DESIGN OF A SIXTEEN CHANNEL ANTERIOR CARDIAC RECEIVE COIL FOR PARALLEL IMAGING AT 3T

by

Michael Smith

A Thesis submitted to the Faculty of Graduate Studies of

The University of Manitoba

in partial fulfillment of the requirements for the degree of

MASTER OF SCIENCE

Department of Electrical and Computer Engineering

University of Manitoba

Winnipeg, Manitoba, Canada

Visual Abstract

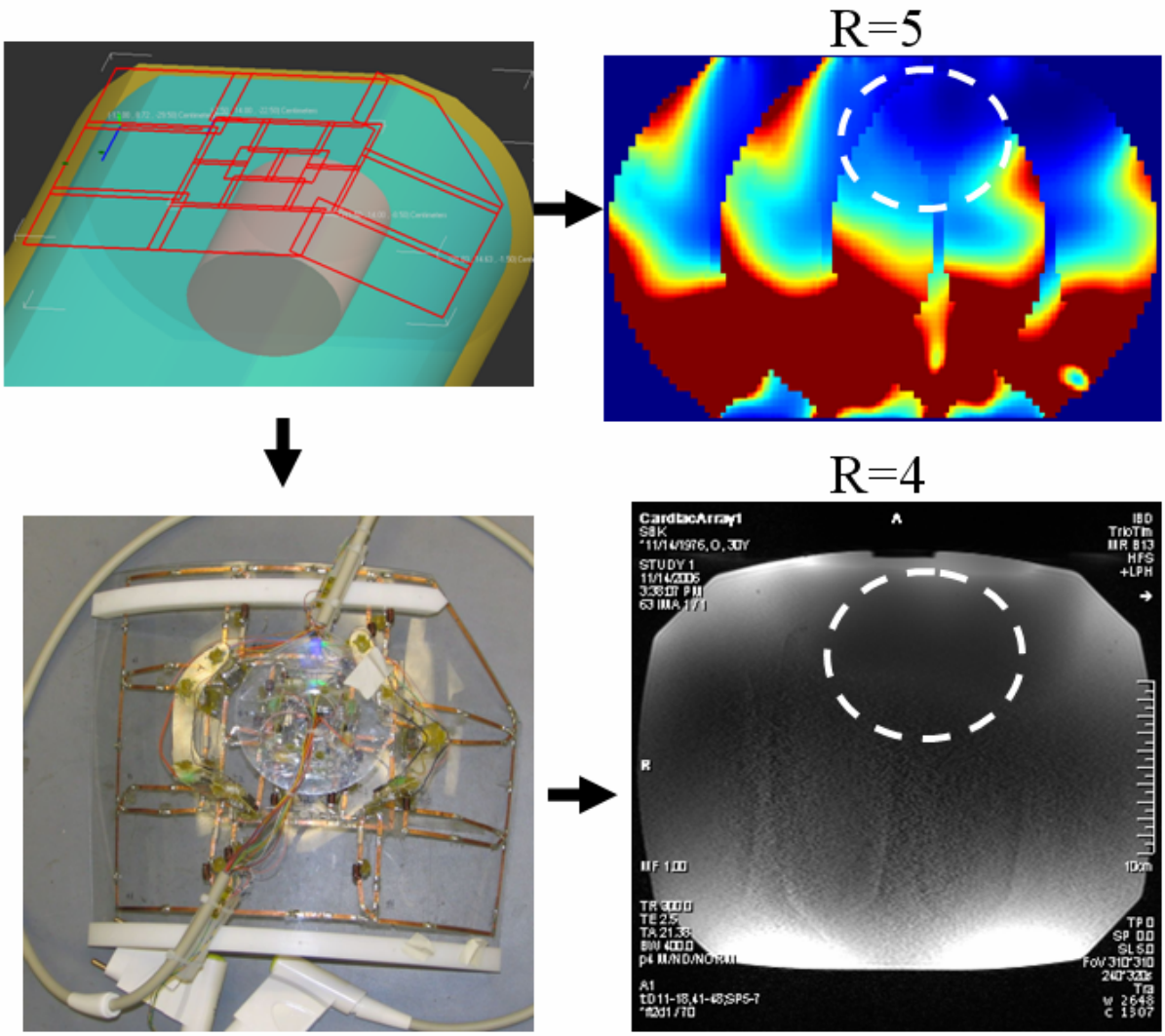

Abstract

A thorough background on MRI physics is presented, emphasizing applications related to receive array coils for SENSE based parallel imaging, to measure induced voltages from RF fields within a sample. The main objective was to construct a 16-channel anterior cardiac array for 3T MRI capable of ⅓ mm pixel resolution across the right coronary artery, while achieving favourable parallel imaging characteristics. Based on FDTD simulations, improved performance relative to previous 16-channel designs was predicted by focusing small elements directly above the ROI, improving SNR behaviour, and using larger peripheral loops for maintaining overall parallel imaging characteristics, verifying the primary project hypothesis. Within the cardiac region, average simulated SNR gains of 62% and 129% were found for acceleration factors R=1 and R=4 respectively, compared to an industry design. Experimental analysis verified that ⅓ mm resolution is achievable within the right coronary artery, while also applying the benefits of parallel imaging up to R=3. This is a crucial step towards improving cardiac diagnostics. In addition, acceleration factors up to R=5 are achievable on a human torso, offering significant imaging time reductions. For an anterior section of the cardiac region, simulated results predicted an average SNR gain of 221%, where 460% gain was found experimentally.

Acknowledgements

For their guidance and assistance towards the successful completion of this challenging project, the author wishes to thank his supervisors, Scott King and Joe LoVetri. He also wishes to thank his family and friends for their support and encouragement, allowing him to explore the rewarding realms of research and engineering.

For technical and financial support, the author would like to thank the National Research Council of Canada's Institute for Biodiagnostics (NRC-IBD), enabling absolute focus on research and studies.

Table of Contents

Nomenclature

α	Flip angle for input pulse [degrees]
$\vec{B}_0$	Main *z*-directed static magnetic field [T]
$\vec{B}_1$	RF excitation field orthogonal to $\vec{B}_0$ field [T]
$\vec{B}_1^+$	Positive circularly polarized $\vec{B}_1$ (transmit field power deposition) [T]
$\vec{B}_{1,rot,c}^+$	Equivalent to $\vec{B}_1^+$, but in the rotating reference frame
$\vec{B}_1^-$	Negative circularly polarized $\vec{B}_1$ (receive field sensitivity) [T]
$\vec{B}_{1,rot,c}^-$	Equivalent to $\vec{B}_1^-$, but in the rotating reference frame
$B_1^e(t)$	Pulse envelope function for $\vec{B}_1$ field [T]
$\vec{B}_{eff}$	Effective $\vec{B}_1$ field $\vec{M}_{rot}$ is exposed to in rotating reference frame [T]
c	Speed of light (2.998×10^8 [m/s])
C_{eff}	Effective capacitance of RF coil with multiple series lumped elements
ΔE	Change of energy between parallel and anti-parallel states [J]
Δf	System bandwidth [Hz]
$\vec{E}$	Electric field vector [V/m]
Ψ	Noise correlation matrix for coil array
σ	Isotropic sample conductivity [S/m]
γ	Gyromagnetic ratio relating $\vec{B}_0$ field to ω_0 [MHz·Rad/T]
g	Geometry factor (*g*-factor) for SENSE
$\vec{G}$	Gradient magnetic field vector having linear spatial dependence [mT/m]
h	Planck's constant (6.626×10^{-34} [J·s])
I_0	Induced unit current [A]
$\vec{J}$	Current density [A/m^2]
$\vec{k}$	*k*-space value for frequency domain signal representation
k_B	Boltzmann's constant (1.3806×10^{-23} [J/K])
λ	Ratio of signal intensities (V_s) used for B_1 mapping
λ_p	Wavelength for propagating signal
L_{eff}	Effective inductance of RF coil
$\vec{M}$	Net magnetic moment per unit volume (bulk magnetization) [J/T·m^3]
$\vec{M}_{rot}$	Net magnetic moment in rotating reference frame [J/T·m^3]
M_z^0	Thermal equilibrium value for $\vec{M}$ [J/T·m^3]
N_α	Probability of being in the parallel state
N_β	Probability of being in the anti-parallel state
$\vec{p}_p$	Complex pixel column vector of received signals for parallel imaging

$\bar{P}_p$	Complex pixel value for parallel imaging (column vector when $R > 1$)
P_{abs}	Absorbed power from $\vec{B}_1^+$ transmit field in sample [J·s]
Q_L	Quality factor for a loaded coil (using typical sample)
Q_U	Quality factor for an unloaded coil (in free space)
ρ	Nuclear spin density
R	Reduction factor for parallel imaging (acceleration factor)
r_c	Coil and other external resistance (non-sample) [Ω]
R_s	Sample resistance [Ω]
S_p	Sensitivity matrix determined for pixel location p
SNR_p	Signal to noise ratio computed for pixel location p
T	Absolute temperature [K]
T_1	Longitudinal (spin-lattice) relaxation time (z-directed) [s]
T_2	Transverse (spin-spin) relaxation time (xy-plane) [s]
T_2^*	Transverse relaxation time constant for inhomogeneous field [s]
T_2^{**}	Transverse relaxation time constant for induced inhomogeneities [s]
T_R	Repetition time between successive k-space line encoding [s]
T_E	Echo time for SE or GE sequences [s]
T_{pe}	Phase encoding wait time [s]
$\vec{\mu}$	Magnetic moment for single nuclei [J/T]
v_p	Propagation velocity [m/s]
V_n	Magnitude of noise voltage [V]
V_s	Magnitude of signal voltage [V]
U_p	Unfolding matrix for pixel p when using SENSE
ω_0	Larmor frequency in (frequency of interest) [rad/s]
ω_{rf}	Carrier frequency for applied RF $\vec{B}_1$ field [rad/s]

List of Acronyms

A-P	Anterior-Posterior
CT	Computed Tomography
EMF	Electro-Motive Force
FDTD	Finite Difference Time Domain
FE	Frequency Encoding
FEM	Finite Element Method
FID	Free Induction Decay
FOV	Field Of View
FSE	Fast Spin Echo
GE	Gradient Echo
GRAPPA	GeneRalized Autocalibrating Partially Parallel Acquisition
GUI	Graphical User Interface
H-F	Head-Foot
IBD	Institute for BioDiagnostics
L-R	Left-Right
MoM	Method of Moments
MRI	Magnetic Resonance Imaging
NMR	Nuclear Magnetic Resonance
NRC	National Research Council
OEM	Original Equipment Manufactured
PDE	Partial Differential Equation
PE	Phase Encoding
PEC	Perfect Electrical Conductor
PML	Perfectly Matched Layer
RF	Radio Frequency
RMS	Root Mean Square
ROI	Region Of Interest
SAR	Specific Absorption Rate
SE	Spin Echo
SENSE	SENSitivity Encoding
SMASH	SiMultaneous Acquisition of Spatial Harmonics
SNR	Signal to Noise Ratio
SoS	Sum of Squares
VNA	Vector Network Analyzer

Permission for Copyrighted Material

Title: Principles of Magnetic Resonance Imaging, A Signal Processing Perspective

Author: Zhi-Pei Liang, Paul C. Lauterbur

Publisher: IEEE Inc. © 2000, ISBN: 0-7803-4723-4

Found on thesis pages: 2, 13, 24, 26, 28, 29, 31

Title: Design of a SENSE-Optimized High-Sensitivity MRI Receive Coil for Brain Imaging

Author: Jacco A. de Zwart, Patrick J. Ledden, Peter Kellman, Peter van Gelderen, Jeff H. Duyn (chief correspondent)

Published in: Magnetic Resonance in Medicine, 47:1218-1227 (2002)

Found on thesis page: 67

CHAPTER 1 Introduction

1.1 Brief MRI History

Since Nuclear Magnetic Resonance (NMR) was discovered in 1946 by Bloch [5] and Purcell [6][9][50], applications of NMR have evolved into well-established imaging techniques used in hospitals worldwide. The most well known application of NMR is Magnetic Resonance Imaging (MRI). The primary drawbacks of MRI include large hardware costs and long imaging times, particularly for 3D scans. A potential solution to reduce imaging time by applying parallel imaging techniques is assessed within this thesis.

MRI has become essential in recent years for diagnosis and medical assessment of living tissues. The use of MRI for immediately acquiring planar and 3D information from a living patient, with minimal demonstrated health risks, has become standard procedure in hospitals worldwide. MRI does not expose the patient to ionizing radiation, as does Computed Tomography (CT) or x-ray technology, making it a safer technique. Also, imaging sensitivity is based on a number of tissue parameters, making MRI extremely versatile in extracting tissue information and creating soft tissue contrast.

Upon diagnosing cancerous tissue, one potential procedure at hospitals includes acquiring a 3D MRI of the patient, segmenting the infected region, and applying non-invasive radiation treatment from a computer controlled Gamma Knife. This amazing process is accomplished within a few days and leaves the patient in a healthier state from a recovery perspective compared with more risky, invasive surgical methods.

MRI is a powerful and noninvasive technique that uses a strong magnetic field to establish NMR in a tissue under examination. The externally-received Radio Frequency (RF) signals are generated through quantum mechanical processes of individual magnetic moments, but can be analyzed macroscopically as a bulk magnetic phenomenon. In 1972, Lauterbur first developed the principles of spatial information encoding essential for image formation utilizing NMR [38]. In modern MRI, both spatial Frequency Encoding

(FE) and Phase Encoding (PE) techniques are employed using gradient fields. The use of gradient fields ensures that the signal frequency is linearly dependent on position in any desired dimension, allowing for image reconstruction (explained later). A typical 2D imaging sequence involves using FE and PE to cover orthogonal directions of *k*-space, or frequency space, where the number of sampling points is directly related to the output 2D image size.

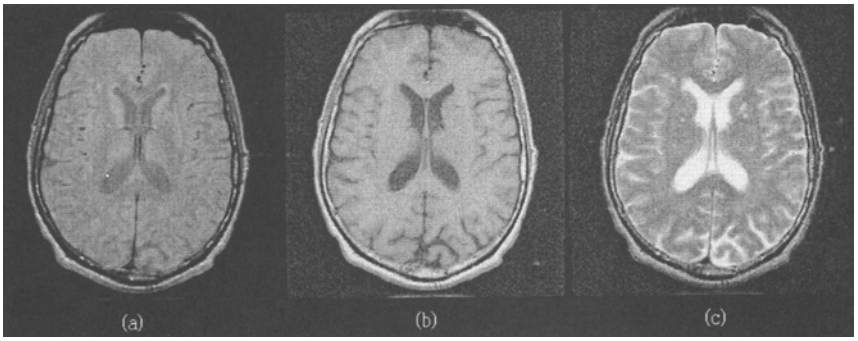

Figure 1.1 - Cross sectional head image obtained using a spin-echo excitation sequence with (a) spin density-weighted contrast (T_E=17ms, T_R=2000ms); (b) T_1-weighted contrast (T_E=18ms, T_R=400ms); (c) T_2-weighted contrast (T_E=80ms, T_R=2500ms) (source: [40], ©2000 IEEE).

Output image pixel values, are a function of the nuclear spin density ρ, the longitudinal (spin-lattice) relaxation time T_1, the transverse (spin-spin) relaxation time T_2, molecular motions, and the chemical shift effect. These parameters can be suppressed or enhanced by altering the system selectable parameters such as repetition time T_R, echo time T_E, and flip angle α (the essential parameters for the understanding of this thesis will be explained later). Figure 1.1 shows how changing system parameters can enhance tissue contrast, by depicting images of a single human brain slice with different imaging parameters.

The opportunity to design large arrays of surface coils has become viable in recent years with cost feasible clinical system designs allowing for up to 32 channels of independent signal reception [19][21][53][80]. The previous single-channel system, which was almost exclusively used prior to the 1990s, permitted only birdcage based coil architectures for large volume coverage, and parallel imaging was not possible.

The objective of this thesis is to further enhance the clinical use of MRI by improving image quality and reducing image acquisition time specific to cardiac imaging. This is accomplished by applying parallel imaging techniques when using a large array of receiver coils. As cost and data throughput constraints on the number of system channels subside, the MRI community is placing significant emphasis on parallel imaging applications and large array receiver coils.

1.2 Current Cardiac Imaging Limitations

A major thrust in current cardiac imaging research involves efforts to minimize natural motion artifacts due to breathing. For image acquisitions during multiple breaths, synchronization between both the respiratory cycle and cardiac cycle is required to minimize motion artifacts because the heart moves during contraction and the diaphragm moves the heart. Acquiring an image during a single breath-hold minimizes motion blurring, but places restrictions on the total number of PE lines that can be acquired, limiting image resolution. The advantage, of course, being that synchronization with only the cardiac cycle is required for single breath-hold imaging.

In single breath-hold acquisitions, resolution can easily be increased in the FE direction by increasing the sampling speed. However, the number of PE direction lines is limited by the time a patient can hold their breath, thereby limiting image resolution. Improving resolution in the PE direction, while maintaining a constant total acquisition time requires the use of parallel imaging. This involves applying mathematical reconstruction techniques, taking information from each array element to reconstruct a full FOV image when fewer than the required PE steps are taken. Evaluation of how well these procedures can reconstruct the full FOV image depends greatly on the geometry of the individual coil elements, which governs their respective sensitivities to different areas of the sample.

Using a 3T designed six-channel Original Equipment Manufactured (OEM) cardiac array coil, it has been shown that 1 mm resolution is achievable, but would be

inadequate for identifying sub-millimetre plaque buildup on the walls of a 3 mm coronary artery, as shown in Figure 1.2. Identification of this plaque provides a crucial step towards improving the in-vivo cardiac disease diagnostic capabilities of MRI. Improving this resolution would also enhance the capabilities of flow imaging to identify irregular or turbulent blood flow.

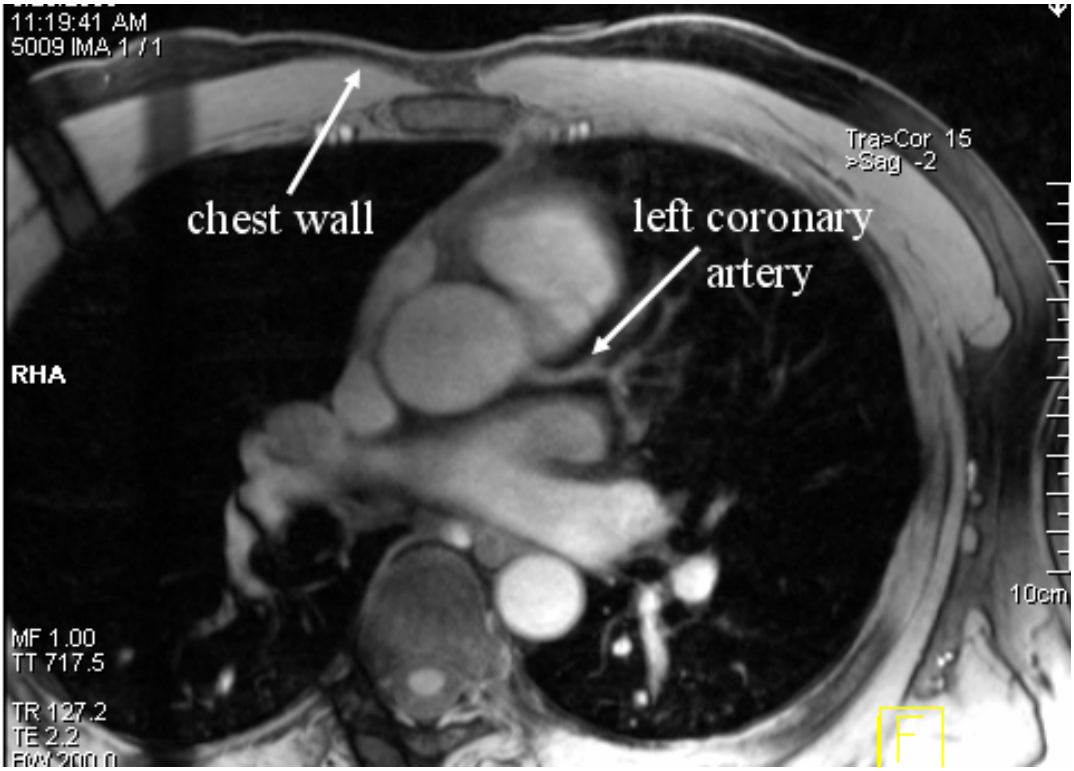

Figure 1.2 - In-vivo cardiac image highlighting the left coronary artery, based on 1.3 mm resolution before applying an image smoothing algorithm by the imaging system (taken with a commercial 3T Siemens Trio Tim system).

Achieving ⅓ mm resolution across the 3 mm right coronary artery would be very useful for identifying plaque buildup on the artery walls. For an example MRI slice taken with 1.3 mm resolution where the left coronary artery is labeled, refer to Figure 1.2. Improved resolution than what was achieved for this image is necessary to identify details regarding the integrity of the arterial walls.

1.3 Previous Work Involving Cardiac Array Coils

In the past two years multiple receive coil designs utilizing a 32-channel system have been constructed and tested for torso and cardiac imaging by several research groups. Previous approaches have involved separate, clamshell style arrays placed anterior and posterior to the human torso, with all elements exhibiting the same geometrical shape and size. To date, all published work on cardiac array coils using 32-channels has been conducted on 1.5T MRI systems; this thesis is the first known investigation at 3T, which will provide improved SNR over 1.5T systems.

A previous design [79][80], which is simulated in this thesis, uses two identical formers containing a four by four grid of rectangular elements sized 7.9 cm by 10.5 cm. Based on quasistatic computational evaluations, this design uses evenly distributed rectangular elements overlapped in the Head-Foot (H-F) direction, but underlapped in the Left-Right (L-R) direction. The anterior 16-channel cardiac array design was used for comparison purposes in a modeling environment for this thesis.

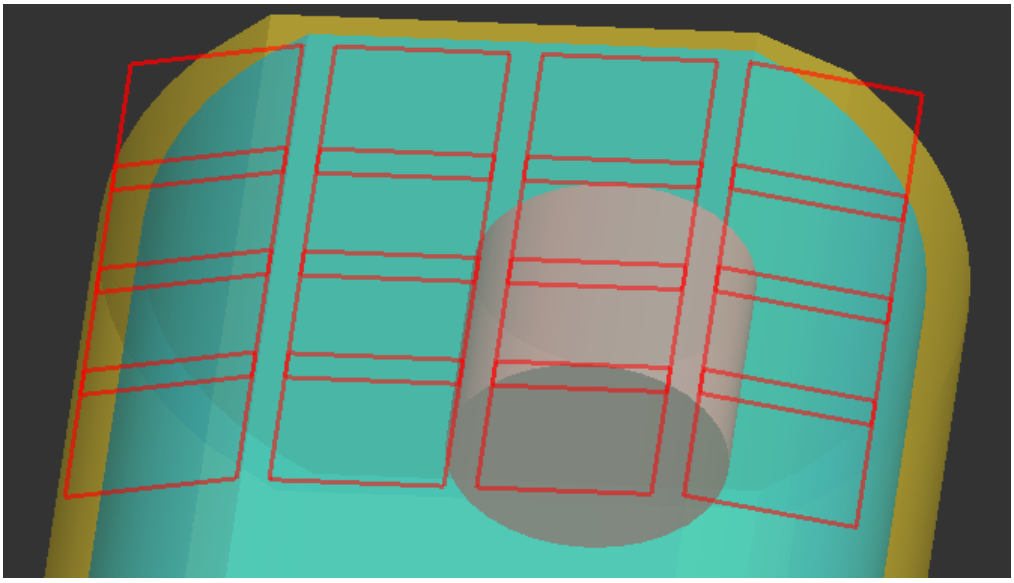

Figure 1.3 – Industry design of a 16-channel anterior cardiac array.

The decision to compare to this previous design was based on establishing comparisons to another 16-channel anterior cardiac array published by another research

group [79]. The electrical traces of this array are depicted in Figure 1.3, shown placed over a human torso numerical model, which was developed for this thesis.

A different design that has been reported involves identical 17-channel anterior and posterior arrays (34 channels in total) arranged in a hexagonal lattice [13], meaning that each row is staggered relative to its neighbouring rows. Five successive H-F directed rows were used, containing three, four, three, four and three separate coil elements, respectively. Each coil element has an octagonal shape with a diameter of 10.6 cm, where element overlap is applied to all nearest neighbours. Because this design was intended for a 32-channel MRI system, two of the elements cannot be used for data acquisition during imaging sequences.

A third 32-channel array design reported for cardiac imaging consists of 11 circular elements for the posterior array and 21 circular loops for the anterior array, where element overlap is applied to all nearest neighbours [19]. Quasistatic simulations determined that placing more elements on the anterior coil serves as beneficial to cardiac array performance. This is intuitive because the cardiac region is closer to the chest wall than the posterior human torso wall. The anterior element diameters were designed to be 7.5 cm, where a diameter of 10.7 cm was used for the posterior elements. Configuration for the anterior array involved left staggered H-F directed rows of five, five, five and six elements, respectively, to account for curvature underneath the left shoulder, while designing for a region on the left of center of the human torso. The posterior array used three rows of four, three and four elements, respectively, staggered in a regular pattern.

1.4 Research Contributions

1.4.1 Hypothesis

The common feature of the three mentioned designs is that they all contain uniformly spaced coils. This does not allow the enhancement of the Signal-to-Noise Ratio (SNR) in specific Regions Of Interest (ROIs) within the imaging volume, such as the heart. The main hypothesis of this research is that concentrating smaller elements

directly above the ROI will result in a significantly higher SNR and a significantly lower *g*-factor (explained later as part of parallel imaging) than standard anterior designs containing the same number of equal sized elements, evenly distributed over the chest, such as those just described. For coverage over a similar total area, this requires using larger elements for regions not over the ROI to maintain a constant total number of elements.

1.4.2 Design Goals

The design goals of this research are to investigate the hypothesis that highly concentrated array elements directly above the ROI can yield a better SNR as well as improved parallel imaging performance within that volume. Larger elements can be used outside the region to maintain full torso coverage for parallel imaging performance. Thus, the main goal is to achieve both a localized SNR improvement and an improvement in parallel imaging performance.

A secondary design difference between previous cardiac arrays and that presented here involves increasing the main system magnet field strength from 1.5T to 3T. Researchers have shown that increasing main magnet strength will increase attainable image SNR by as much as two [66], as well as improve parallel imaging behaviour [75]. For this reason, all systems analyzed in this thesis assumed a 3T MRI system. Note that detrimental side effects associated with increased magnetic fields exist and must be accounted for by the designer. Some of these include increased power deposition within the patient, more complicated RF circuitry and wave behaviour in element profiles. The wave behaviour in the sample must be taken into account for successful design.

For fair comparison, the 16-channel anterior cardiac array designs evaluated in this thesis are assessed relative to the previous 16-channel anterior cardiac array design depicted in Figure 1.3 [79] by utilizing a standardized spine array. A nine-channel OEM spine coil was available for testing purposes and was held standard across all comparisons unless otherwise stated. Although comparisons to previous designs are

useful, and were analyzed in this thesis, the designs developed herein are also compared against absolute performance specifications (to be listed later).

The methodology includes determining conductor placement for the 16-channel anterior cardiac array by using computational analysis software tools. Evaluation of different coil configurations requires SNR and parallel imaging analysis within the cardiac region. The traces must then be placed on a prototype former and each element must be inductively decoupled and tuned. A complete prototype was built and interfaced to a clinical 3T Siemens Trio Tim system via connector cables for experimental verification. All interfacing and receiver coil circuitry was designed as part of this thesis with the exception of the pre-amps, which were designed and fabricated in-house at the National Research Council (NRC) Institute for Biodiagnostics (IBD).

1.4.3 Thesis Objectives

The objective of this thesis is to design a 16-channel anterior receive array coil for parallel imaging of the human cardiac region. Using a full-wave calculation model, the array coil design must be assessed based on both SNR performance within the cardiac region and parallel imaging abilities utilizing SENSitivity Encoding (SENSE) over a range of reduction factors R (to be explained in Section 2.4.4).

For experimental comparisons to a readily available cardiac coil, measurements must be taken with the coil provided with the Siemens system purchased by the NRC-IBD in March of 2006, being a six-channel anterior cardiac array. For computational comparisons, the geometry of previous 16-channel anterior cardiac designs for parallel imaging at 1.5T [19][21][80] must be adapted to 3T environments. Currently, no reported design is known of for a 16-channel anterior cardiac array at 3T. The Siemens system also has 24 spine elements, of which nine are to be used in conjunction with all anterior designs for posterior SNR benefits. The cardiac coil will rest on the subject and the existing spine coil will be used for posterior torso sensitivity. The Siemens system has a maximum of 32 available channels, where 25 are required for this research.

During coil design, system connectivity must be considered. Available Siemens connector plugs come in arrays of four, six, or eight. For clinical ease of use, the design must be well suited for these plug options. The design must be interfaced to Siemens based system connectors, using a total of 16 channels for the anterior array.

The primary objective of this research is to design a coil array capable of acquiring an image with ⅓ mm resolution across the right coronary artery, having equivalent SNR to the six-channel OEM array when acquired with 1 mm resolution, when implemented on a 32-channel 3T Siemens Trio Tim system. Based on SNR analysis (see Section 2.4), this indicates that a three-fold improvement in SNR is required to achieve ⅓ mm resolution. Satisfying this specification will be determined through analysis of coronal slices at the depth of the anterior portion of the right coronary artery, being 3 cm-4.5 cm below the chest wall. The sample applied will be a uniform gel phantom of similar dimensions to a human torso. The gel material is used to model the effects of compartmentalization found in the human body, where aqueous based saline samples are not well suited. The desired effect is to dampen the wave behaviour within the sample, relative to that found when using an aqueous phantom.

Table 1.1 – List of thesis project specifications and deliverables.

Number	Specification or Deliverable
1	achieve ⅓ mm resolution with equivalent SNR to OEM chest array across 3mm anterior portion of right coronary artery (3 cm - 4.5 cm deep)
2	assess parallel imaging performance throughout cardiac region
a)	g-factor max < 2, avg < 1.25 for all axial slices using $R = 4$
b)	g-factor max < 1.5, avg < 1.15 for all axial slices using $R = 3$
3	user friendly GUI based program for array design and parallel imaging analysis of XFDTD and experimental output files

A second objective of this thesis relates to parallel imaging performance. The design must demonstrate maximum and average g-factor (explained in Section 2.4.4) values less than 2 and 1.25 respectively for all axial planes over the cardiac region with using a reduction $R = 4$ (L-R PE). For now, the g-factor is considered as a ratio measure for the additional image noise resulting from parallel imaging with an associated

reduction, or acceleration factor. The maximum and average *g*-factor values must not exceed 1.5 and 1.15 respectively for reduction $R = 3$, using the same imaging parameters. Comparisons relative to previous 16-channel anterior cardiac array coils cannot be established from an experimental perspective, as such, these comparisons cannot be verified, but should be inspected from a computational environment.

Design analysis should be conducted using a full wave Finite-Difference-Time-Domain (FDTD) simulation package called XFDTD6.3 by REMCOM Inc., but requires significant post processing calculations for proper MRI investigation. XFDTD was chosen because it is the most common FDTD package used by MRI researchers. As part of this thesis, a post-processing software package was developed for parallel imaging MRI performance analysis. This software aids RF coil design by analyzing coil behaviour through consideration of polarized magnetic fields. This enables high field coil analysis for both transmit and receive coils, while accounting for parallel imaging techniques such as SENSE for composite image reconstruction and *g*-factor map calculations. The program must be user friendly with an adaptable Graphical User Interface (GUI). It must allow for analysis of 64-channel coil arrays, including modifying the flip angle, signal reception by applying reciprocity theory, and composite image reconstruction by multiple approaches such as Sum-of-Squares (SoS) and Roemer optimal (explained in Section 0). A tabulated list of specifications and deliverables is provided above in Table 1.1.

1.5 Thesis Organization

A concise foundation for the physics of NMR and MRI technology is presented in Chapter 2, incorporating both classical theory and quantum theory for explanations of bulk nuclear magnetization, sample excitation and signal reception. Upon establishing the governing relationship for SNR, by exploring the electric and magnetic fields within a sample, the use of phased array coils is analyzed for parallel (simultaneous) data acquisition. Circuit analysis is used to determine impedance matching equations for maximizing received signals, where different composite image formation techniques are described to establish single image SNR from array coils. Different imaging sequences

are explored, including Spin Echo (SE) and Gradient Echo (GE), as well as their effects on resultant images, being of particular concern with arrays of surface coils. Parallel imaging techniques are described, focusing on applications of SENSE, which was used throughout this thesis by comparing g-factor maps for design evaluation. A connection between the presented MRI theory and RF array coil design through computations is established, with emphasis on the FDTD approach for electromagnetic field modeling. The primary equations utilized for computational array coil design aimed for use in parallel imaging are outlined.

Chapter 3 involves verification of the XFDTD electromagnetic modeling environment used for MRI coil design. Next, the Matlab based program that was written for this thesis is described, including capabilities related to image representation and reconstruction from a parallel imaging perspective. It is useful for MRI based design evaluation of post-processing of output fields from XFDTD. Next the six-channel OEM chest array is analyzed, as required to establish SNR improvements necessary to improve image resolution. Various designs are analyzed for the 16-channel anterior cardiac array described herein, and are compared both to the six-channel OEM array and the 16-channel anterior cardiac array of Figure 1.3. Chapter 3 then explores electrical considerations relating to the coil materials, testing signal losses from different potential conductors and outlining the required electrical components for each array element.

Prototype construction and experimental verification is covered within Chapter 4. The iterative design process for inductively decoupling elements and connecting appropriate matching circuitry is described. Experimental images obtained using the 16-channel anterior cardiac array with a nine-channel OEM spine coil are presented. The resultant images are compared to those obtained with a six-channel OEM cardiac array with the same spine coil connected. Experimental analysis is performed to establish agreement between simulations and project specifications. This is accomplished by comparing of SNR profiles and g-factor maps from the sets of data.

CHAPTER 2 MRI Background

2.1 NMR Basics

2.1.1 Nuclear Spin Systems

The principles of NMR are best described by a combination of quantum mechanical and classical models. From quantum mechanics, atomic nuclei possess a property called spin, which is analogous to angular momentum for a classical model. Considering a proton as a rotating sphere with distributed positive charge with a semi-classical model (does not perfectly conform with the true quantum model), the distributed charge circulating about the axis of rotation is analogous to a current, producing a small magnetic field, called its magnetic moment $\vec{\mu}$. The magnetic moment is related to the angular momentum by the nucleus-specific proportionality constant γ, called its gyromagnetic ratio. The transverse component of the potential spin states, μ_{xy}, and the longitudinal component, μ_z, can also be calculated as

$$\mu_{xy} = \frac{\gamma h\sqrt{3}}{4\pi}, \qquad \mu_z = \frac{\gamma h}{4\pi} \tag{2.1}$$

where h is Planck's constant, 6.626×10^{-34} [J·s].

In the presence of an external magnetic field, $\vec{B}_0$, there are two possible spin states for protons. Application of an external magnetic field to hydrogen atoms is shown in Figure 2.1. In the presence of the magnetic field $\vec{B}_0$, the randomly oriented nuclear spins begin to precess, with the axis of precession aligned with or opposite to the applied magnetic field. In addition, the angle θ represents the angle between the magnetic moment and the applied magnetic field, whose strength determines the energy difference between the two states, named parallel and anti-parallel.

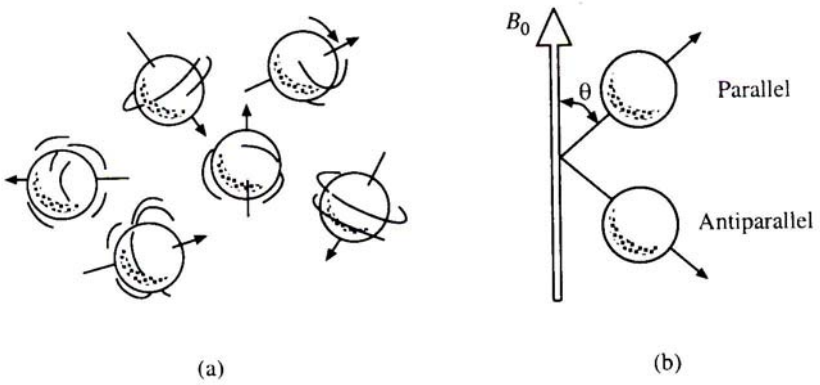

Figure 2.1 - Nuclear magnetic moment vectors (a) pointing in random directions and (b) aligned in the direction of an external magnetic field (source: [40], ©2000 IEEE).

Parallel magnetic moments result in a lower energy configuration, called the parallel state, and anti-parallel states give a higher and less stable energy state, called the anti-parallel state. Zeeman splitting governs the difference in energy between the parallel and anti-parallel states, with the associated energy difference given as

$$\Delta E = \frac{\gamma \hbar B_0}{2\pi} \tag{2.2}$$

Using the standard NMR convention of $\vec{B}_0 = B_0 \hat{z}$, the nuclear precession about the *z*-axis, or $\vec{B}_0$, can be calculated from a classical treatment [40] as

$$\begin{cases} \mu_{xy}(t) = \mu_{xy}(0) e^{-i\gamma B_0 t} \\ \mu_z(t) = \mu_z(0) \end{cases} \tag{2.3}$$

This equation demonstrates that the nuclear precession frequency is related to the main magnetic field of an MRI system by the gyromagnetic ratio. When referring to NMR systems, this precession frequency is commonly known as the Larmor Frequency:

$$\omega_0 = \gamma \mid \vec{B}_0 \mid \tag{2.4}$$

For nuclei containing several protons, things get much more complicated compared to a proton in free space. The Pauli Exclusion Principle states that, in a nucleus, no two fermions (protons as applied here) will have the same quantum state. The result is that all nuclei with an odd number of neutrons and protons have half-integral spin, and their net angular momentum is nonzero. These half-integral spin nuclei, which

are useful for NMR purposes, include ^{1}H, ^{13}C, ^{19}F, ^{23}N and ^{31}P. The ^{1}H atom is abundant in biological tissue and therefore commonly used in NMR imaging. This thesis focuses on ^{1}H proton imaging, where $\frac{\gamma}{2\pi} = 42.58$ [MHz/T]. From the quantum model, the *z*-component of the magnetic moment vector for the ^{1}H atom is given as

$$\mu_z = \pm \frac{1}{2} \gamma \frac{h}{2\pi} \tag{2.5}$$

2.1.2 Bulk Nuclear Precession

Before applying an external magnetic field, all nuclei are oriented in random directions, resulting in a zero net magnetic moment, shown in Figure 2.1a. After applying the external $\vec{B}_0$ field, and using N_α to denote the probability that a proton is in the parallel state, and N_β as the probability of it being in the anti-parallel state ($N_\alpha + N_\beta = 1$), Boltzmann's law is used to fit the population ratios, which states that

$$\frac{N_\alpha}{N_\beta} = e^{\left(\frac{\Delta E}{k_B T}\right)} \tag{2.6}$$

where $k_B = 1.3806 \times 10^{-23}$ [J/K] is Boltzmann's constant, T is the absolute temperature, and ΔE is the energy difference between the two states. Using equation (2.2) and a first order exponential approximation, equation (2.6) simplifies to

$$\frac{N_\alpha}{N_\beta} \approx 1 + \frac{\gamma h \mid \vec{B}_0 \mid}{2\pi k_B T} \tag{2.7}$$

This indicates that more spins will be found in the lower energy state, generating a macroscopic bulk magnetization for the tissue. The bulk magnetization is thought of as the vector sum of all the microscopic magnetic moments in the object. The net magnetic moment per unit volume, or bulk magnetization $\vec{M}$, is given by the energy difference between states N_α and N_β , multiplied by the number of protons per unit volume *n*, and magnetic moment μ_z from equation (2.5). The resulting bulk magnetization is given by

$$\vec{M} = \frac{1}{2}(N_\alpha - N_\beta)\frac{\gamma h}{2\pi}\hat{z} \approx \frac{\gamma h \mid \vec{B}_0 \mid}{8\pi k_B T} n \mu_z \hat{z} \tag{2.8}$$

Notice that a stronger $\vec{B}_0$ field produces a larger net magnetization, which is desirable because it increases the resulting RF signal voltage as will be shown in Section 2.4.1. This demonstrates a benefit of increasing the $\vec{B}_0$ field for MRI systems.

2.1.3 Magnetic Field Excitation and Frequency Selectivity

A net bulk magnetization $\vec{M}$ results with an applied static $\vec{B}_0$ field, but cannot be measured with an RF receiver until the magnetization is perturbed from the *z*-axis to generate a flux change that can be measured by the receiver. By applying an RF field in the transverse *xy*-plane (called the excitation field $\vec{B}_1$), being orthogonal to the $\vec{B}_0$ field, $\vec{M}$ is temporarily perturbed to the transverse plane under the requirement that the transmitted energy is equal to the energy difference between the possible spin states, as given in equation (2.2). Using this quantum model, Planke's Law, and equation (2.4), the $\vec{B}_1$ field oscillation frequency ω_{rf} can be calculated as equal to the Larmor Frequency:

$$\frac{h\omega_{rf}}{2\pi} = \Delta E = \frac{\gamma \hbar B_0}{2\pi} \therefore \omega_{rf} = \omega_0 \tag{2.9}$$

In other words, to satisfy the resonance excitation condition, the applied RF field must be at the system Larmor Frequency determined by the main magnetic $\vec{B}_0$ field. A typical $\vec{B}_1$ excitation field is given as linearly polarized

$$\vec{B}_1(t) = 2B_1^e(t)\cos(\omega_{rf}t + \varphi)\hat{x} \tag{2.10}$$

but can be mathematically broken down into two circularly polarized fields rotating in opposite directions, shown as

$$\vec{B}_1(t) = B_1^e(t)[\cos(\omega_{rf}t + \varphi)\hat{x} - \sin(\omega_{rf}t + \varphi)\hat{y}] + B_1^e(t)[\cos(\omega_{rf}t + \varphi)\hat{x} + \sin(\omega_{rf}t + \varphi)\hat{y}] \tag{2.11}$$

or

$$\vec{B}_1(t) = \vec{B}_1^+(t) + \vec{B}_1^-(t)$$

for pulse envelope $B_1^e(t)$, carrier frequency ω_{rf} and phase angle φ. The $\vec{B}_1^+(t)$ field represents the circularly polarized field rotating in the same direction as the nuclear magnetization, and $\vec{B}_1^-(t)$ represents the circularly polarized field rotating in the opposite direction. The $\vec{B}_1^+(t)$ field is used for sample excitation, and therefore is called the transmit field, where the $\vec{B}_1^-(t)$ field represents the receive coil sensitivity, and both will be considered more fully in Section 2.4.1.

2.1.4 Bloch Equation

The time dependent behaviour of magnetization $\vec{M}$ with applied magnetic field $\vec{B}_1(t)$ is given by the Bloch Equation, having the form used in NMR as [40]

$$\frac{d\vec{M}}{dt} = \gamma\vec{M} \times \vec{B} - \frac{M_x\hat{x} + M_y\hat{y}}{T_2} - \frac{(M_z - M_z^0)\hat{z}}{T_1} \tag{2.12}$$

where M_z^0 is the thermal equilibrium value for $\vec{M}$ in the presence of $\vec{B}_0$ only. T_1 describes the longitudinal relaxation time constant (z-axis), and T_2 governs the transverse relaxation process (xy-plane). Considering the behaviour of $\vec{M}$ during excitation, meaning the time when the RF pulse is applied, the two relaxation terms can be ignored, as they are negligible if the RF pulse duration is short compared to T_1 and T_2. The following assumptions are commonly made in mathematical treatments in MRI, as such are applied for the remainder of this thesis:

1) No T_1 or T_2 relaxation during magnetization excitation.

2) Linear excitation of flip angle α, meaning the flip angles can be accurately calculated using the Fourier transform.

3) Off-resonance excitations are ignored, making flip angle α constant.

4) Chemical shift effect is ignored; being the change of resonant frequency caused by interactions with nearby nuclei, which is common within molecules

A simpler form for the Bloch equation is derived by changing to a frame of reference rotating at our frequency of interest (meaning $\omega = \omega_0$). Using the subscript *rot* to represent rotating frame of reference variables, the Bloch Equation then becomes

$$\frac{\partial \vec{M}_{rot}}{\partial t} = \gamma \vec{M}_{rot} \times \vec{B}_{eff} \tag{2.13}$$

where

$$\vec{B}_{eff} = \vec{B}_{rot} + \frac{\omega}{\gamma} = \vec{B}_{rot} - \frac{\gamma B_0 \hat{z}}{\gamma} = 0$$

Notice that the effective magnetic field $\vec{B}_{eff}$, being the field that the bulk magnetization vector experiences in the rotating frame, vanishes when $\vec{B}_{rot} = B_0 \hat{z}$, which effectively makes $\omega = -\gamma B_0 \hat{z}$. This also means that the longitudinal field vanishes and $\vec{M}_{rot}$ is stationary in the rotating frame. Using prime to denote the rotating frame axes, the excitation RF pulse in the rotating frame $\vec{B}^{+}_{1,rot} = B_1^e(t)\hat{x}'$ is equivalent to the on resonance excitation $\vec{B}_{eff} = B_1^e(t)\hat{x}'$. Substitution of this relation into equation (2.13) results in the equation for the motion of bulk magnetization vector $\vec{M}$:

$$\begin{cases} \dfrac{dM_{x'}}{dt} = 0 \\ \dfrac{dM_{y'}}{dt} = \gamma B_1^e(t) M_{z'} \\ \dfrac{dM_{z'}}{dt} = -\gamma B_1^e(t) M_{y'} \end{cases} \tag{2.14}$$

Using initial conditions $M_{x'}(0) = M_{y'}(0) = 0$ and $M_{z'}(0) = M_z^0$, a closed form solution to equation (2.14) is calculated for pulse length τ_p to be [40]

$$\begin{cases} M_{x'}(t) = 0 \\ M_{y'}(t) = M_z^0 \sin\left(\int_0^t \gamma B_1^e(\hat{t})d\hat{t}\right) & 0 \le t \le \tau_p \\ M_{z'}(t) = M_z^0 \cos\left(\int_0^t \gamma B_1^e(\hat{t})d\hat{t}\right) \end{cases} \qquad (2.15)$$

A visual aid for the motion of $\vec{M}$ is shown below in Figure 2.2, both considering the stationary laboratory frame and the rotating frame of reference, when an RF field is applied. It is assumed that $\vec{M}$ is originally created by static magnetic field $\vec{B}_0$.

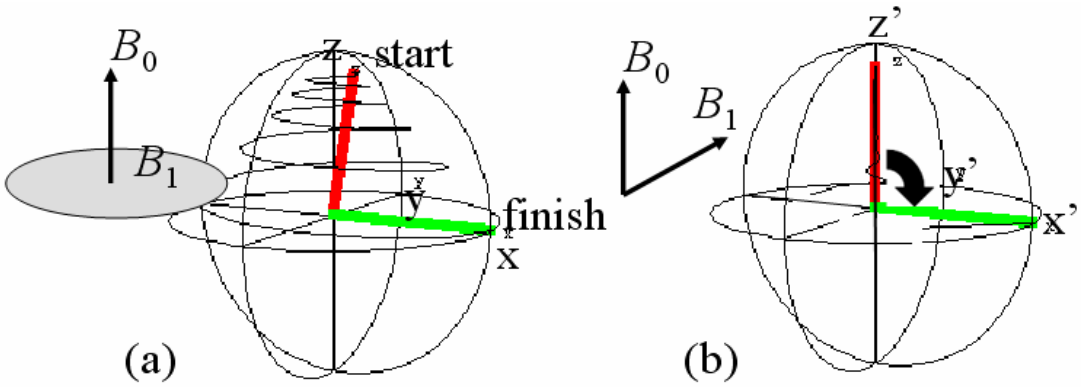

Figure 2.2 - Result of magnetization change when applying RF B_1 field in (a) the laboratory frame of reference and (b) the rotating frame of reference.

2.1.5 Fourier Approximation

The Bloch equation is required to solve exactly how a general RF pulse $B_1 e^{-i\omega_{rf}t}$ affects the various spin magnetizations. However, a general solution has not been developed for a general envelope function $B_1^e(t)$. Fourier analysis enables a solution with little deviation from solving the Bloch equation provided that the tip angle is below 10° for all spins within the sample. For this, the frequency spectrum of our pulse envelope function is required, as given by the Fourier transform:

$$F\{B_1^e\}(\omega) = \int_{-\infty}^{\infty} B_1^e(t) e^{i\omega t} dt = F.T.\{B_1^e(t)\} \tag{2.16}$$

$$\vec{B}_1^+(t) = \frac{1}{2\pi} \int_{-\infty}^{\infty} F\{B_1^e\}(\omega) e^{-i(\omega+\omega_{rf})t} d\omega \tag{2.17}$$

Using the Fourier transform, the transmit field is given as a clockwise rotating continuum of vectors as in equation (2.17). By separating the bulk magnetization vectors in terms of groups of nuclei with different spin frequencies, the resulting excitation effect is calculated under the assumption that the spin system behaves like a linear system. This means that the excitation effect of $\vec{B}_1^+(t)$ on $\vec{M}$ is equal to the sum of the excitation effects of individual components [40]. It should be noted that the system is not linear during excitation, which is why the Fourier analysis approach looses accuracy for flip angles above 10°.

By using $\vec{B}_1^e$ as the excitation field acting on a magnetization precessing at a given frequency, $\vec{M}(\omega + \omega_{rf})$, the flip angle $\alpha(\omega)$ for each group with the same spin frequencies is calculated as

$$\alpha(\omega) = \frac{|F\{B_1^e\}(\omega)|}{|F\{B_1^e\}(0)|} \alpha(0) \tag{2.18}$$

where

$$\alpha(0) = \gamma \int_0^{\tau_p} B_1^e(\tau) d\tau$$

2.1.6 Selective RF Pulse Excitation Using Gradients

To determine the origin of the signal in a 2D slice, first, only nuclei in a desired slice are excited, which requires the use of gradient fields G_x, G_y and G_z . These gradients are used make the *z*-directed magnetic field B_z a function of their respective dimensions, as described by

$$G_x = \frac{\partial B_z}{\partial x}, \qquad G_y = \frac{\partial B_z}{\partial y}, \qquad G_z = \frac{\partial B_z}{\partial z} \tag{2.19}$$

resulting in

$$G(x, y, z) = (G_x x + G_y y + G_z z)\hat{z} \tag{2.20}$$

and

$$B_z(x, y, z) = B_0 + G(x, y, z) \tag{2.21}$$

All gradients must vary linearly to impose a linearly dependant value for the frequency of precession ω_0 on spatial position. Because of its square frequency profile, the sinc pulse is typically used as the excitation pulse, which will correspond to a square slice profile. Only nuclei whose Larmor Frequency lie within the bandwidth of the excitation pulse are tipped into the transverse plane, where their tipping angle $\alpha(\omega)$ is determined by the strength of the transmit field $\vec{B}_1^+$ at that frequency. The slice width depends on both the bandwidth of the sinc pulse and the magnitude of the applied gradient field, as shown in Figure 2.3. The RF pulse bandwidth Δf is related to the slice thickness Δz by

$$\Delta f = \frac{\gamma G_z \Delta z}{2\pi} \tag{2.22}$$

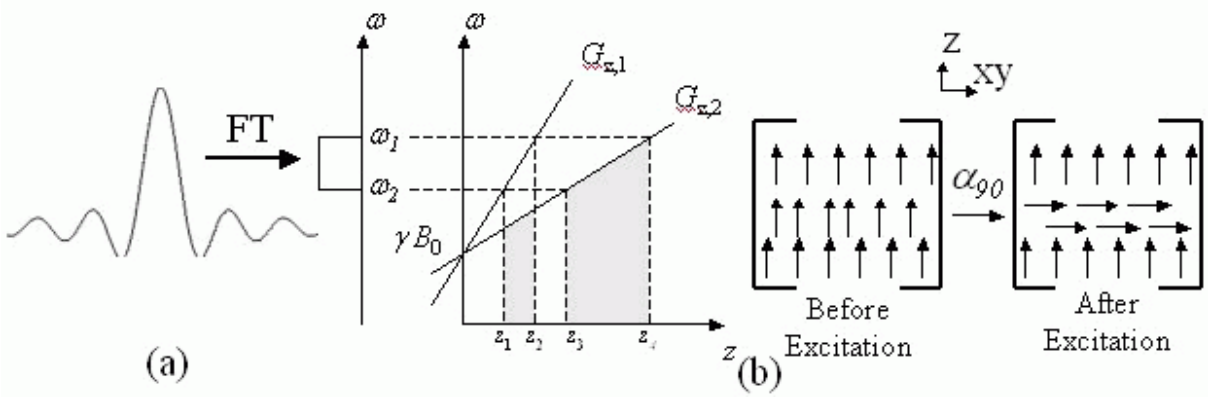

Figure 2.3 – (a) Pulse mapping of two different slice widths, determined by pulse bandwidth (ω_2-ω_1) and two different gradient field strengths $|G|$, depicted with gradient field G_z, giving corresponding slice widths ($z_4 - z_3$) and ($z_2 - z_1$). (b) Excitation effect on magnetic moments.

Since any physical realization of a sinc pulse is inherently a truncated approximation and spin systems behave nonlinearly during excitation, the slice selection

profile will not be perfectly square. By using the Bloch Equation, being a better model of the quantum mechanical processes than the Fourier approximation, any desired slice selection profile is possible, at the expense of increased mathematical complexity required to numerically solve for the pulse envelope $B_1^e(t)$. However, any field inhomogeneities in $\vec{B}_0$ or $\vec{B}_1^+$ not accounted for during pulse design will change the slice profile, making the required effort even less appealing.

2.1.7 Free Induction Decay

Free Induction Decay (FID) is the term given to the signal induced in a coil due to "free" precession of the magnetization vector $\vec{M}$ about the $\vec{B}_0$ field. Faraday's law of electromagnetic "induction" governs the induced signal voltage; and signal amplitude decreasing with time is described by "decay". Faraday's law of induction, also one of Maxwell's equations, is given as

$$\oint_C \vec{E} \cdot dl = \int_S \vec{B} \cdot d\vec{A} \qquad \text{or} \qquad \nabla \times \vec{E} = -\frac{\partial \vec{B}}{\partial t} \tag{2.23}$$

The FID is induced in a receiving RF coil, which must be sensitive to the corresponding signal frequency ω_0. To maximize the induced voltage, the coil should be oriented in the *xy*-plane, being orthogonal to the *z*-directed magnetic field $\vec{B}_0$. The maximum amplitude of an FID signal is always at time $t = 0$, and has value $M_z^0 \sin\alpha$ for flip angle α. There are three different inherent transverse decay rates to be considered when measuring an NMR signal, which are different for different tissues and materials.

For an FID, the slowest transverse decay rate of T_2 describes exponential relaxation of the transverse magnetization of all spectral components, simultaneously returning to their steady state magnetization having $M_{xy} = 0$. The FID amplitude follows the exponential T_2 decay curve only if the $\vec{B}_0$ field is perfectly homogeneous and no chemical shift is present. In other words, this requires that only one resonant frequency

exists for all spins, which cannot be physically realized. For a spectral density of sample spins $\rho(\omega)$ and transverse decay rate T_2, an ideal FID signal is

$$V_s(t) = \sin\alpha \int_{-\infty}^{\infty} \rho(\omega) e^{-t/T_2(\omega)} e^{-i\omega t} d\omega \quad t \geq 0 \tag{2.24}$$

The second FID decay rate considered, T_2^*, occurs when $\vec{B}_0$ field inhomogeneity exists, causing a small spectrum of resonant frequencies through the sample slice. Because each resonant frequency precesses at a different rate, phase coherence is lost through time, causing the FID signal to decay faster. Assuming a Lorentzian distribution for the resonant frequency spectrum, the spectral density function is given as

$$\rho(\omega) = M_z^0 \frac{(\gamma \mid \Delta\vec{B}_0 \mid)^2}{(\gamma \mid \Delta\vec{B}_0 \mid)^2 + (\omega - \omega_0)^2} \tag{2.25}$$

for spatially inhomogeneous magnetic field $\vec{B}_0$. The accelerated signal decay for this situation, characterized by decay rate T_2^*, is given by [40]

$$V_s(t) = \pi M_z^0 \gamma\Delta \mid \vec{B}_0 \mid \sin\alpha e^{-t/T_2^*} e^{-i\omega_0 t} \tag{2.26}$$

where

$$\frac{1}{T_2^*} = \frac{1}{T_2} + \gamma\Delta \mid \vec{B}_0 \mid$$

Finally, the fastest decay rate, denoted by T_2^{**}, results when the $\vec{B}_0$ field is inhomogeneous due to induced gradient fields, meaning equation (2.20) is non-zero. The gradient fields create a wide spectrum of spin frequencies, causing the FID signal to decay much faster than T_2^*, where the decay rate T_2^{**} applies. The value of this decay rate changes when changing the gradient field magnitude.

An echo signal describes the process when a set of spins that have lost phase coherence reverse relative spin directions to one another. Through time, the set of magnetization vectors will realign, and then lose their coherence again. This process creates a two-sided FID, called an echo signal. The process is shown graphically in

Figure 2.5 for a sample type of echo formation (described shortly). Also, it is described how the three transverse decay rates play a role in pulse sequences and imaging.

The longitudinal decay rate of T_1 governs the relaxation process returning the magnetized *z*-component to steady state value M_z^0. This time constant is longer than any of the transverse processes described above, varying depending on the material.

2.2 Imaging Methods

There are many different control parameters in NMR imaging, making it an extremely powerful technique because they can be used to establish tissue contrast between a multitude of tissues. By manipulating the gradient fields and the applied pulse sequence, the slice width, orientation, and image Field Of View (FOV) can be altered. By changing parameters such as repetition time T_R, and echo time T_E, image intensity is changed to display tissue contrast based on proton density weighting ρ, T_1 weighting, or T_2 weighting. By adjusting input RF power, the flip angle α can be controlled to produce optimal contrast or signal intensity in a specific area within the ROI. Allowing for moderate SNR values, short pulse sequences can be designed for increased patient throughput. Also, the type of pulse sequence can be changed between SE or GE, to enhance desired contrast effects, which can be extended to an echo train for multiple echo signals and faster imaging.

2.2.1 Spin Echo and Gradient Echo Pulse Sequences

There are two fundamentally different types of pulse sequences to be considered. Using these sequences, one can generate a number of two sided echo signals from an initial FID, commonly called echo trains, by repeating the echo generating mechanism. The two different sequence types are Spin Echo (SE) and Gradient Echo (GE).

An SE signal is generated by applying two input pulses through the transmit coil with a delay time τ between the pulses. The notation to describe pulse sequences uses α

to denote the flip angle of an applied RF pulse and τ to signify a wait time after the pulse. A generalized two pulse SE sequence is given as

$$\alpha_1 - \tau - \alpha_2 \tag{2.27}$$

If surface coils are used for transmission, the values of flip angles α_1 and α_2 must be specified for a given location because of the flip angle dependence on spatial position. Surface coils are further discussed in Section 2.3. During time delay τ, the spins lose phase coherence before the α_2 refocusing pulse. Loss of coherence for SE sequences occurs according to the exponential T_2^* decay curve, and is caused by $\vec{B}_0$ field inhomogeneities giving a position dependent rotation frequency.

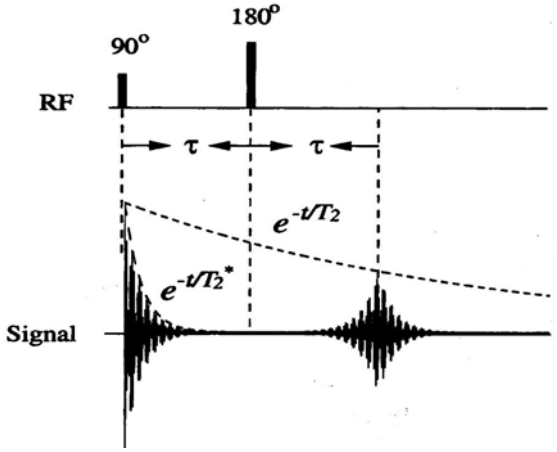

Figure 2.4 – An FID followed by a two sided echo signal comprising an SE sequence as used by applying a 90° - τ - 180° pulse sequence (source: [40], ©2000 IEEE).

For steady state bulk magnetization M_z^0 and imaging echo time $T_E = 2\tau$, the echo signal amplitude for an SE sequence is given by [40]

$$A_E = M_z^0 \sin(\alpha_1) \sin^2\left(\frac{\alpha_2}{2}\right) e^{-T_E/T_2} \tag{2.28}$$

To acquire maximum echo signal amplitude, flip angles α_1 and α_2 should be 90° and 180° respectively, creating re-established phase coherence at time 2τ. The resulting output signal will be symmetric about time point $t = 2\tau$. Figure 2.4 shows the received signal through time with application of an SE pulse sequence. Figure 2.5 shows the corresponding spin magnetization vectors for a standard SE sequence. This visualization

assists in understanding why the received signal decays, and then forms a two-sided FID after the second pulse is applied. A similar image can be used to describe GE processes.

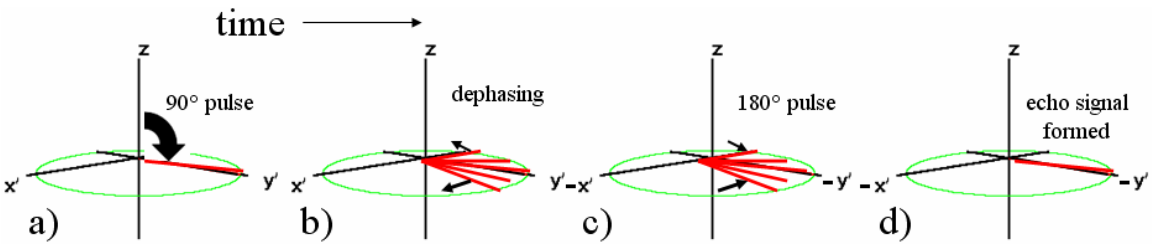

Figure 2.5 – Depiction of magnetization vectors for a standard SE sequence. The T_2 decay process occurs through time, meaning the magnetization magnitude in state d) is smaller than that of state a). a) The first RF pulse is applied tipping the magnetization off equilibrium into the transverse plane. b) Magnetizations of different rotational frequencies dephase according to decay T_2^* because of an inhomogeneous $\vec{B}_0$ field, making the FID signal decay. c) The second RF pulse flips the magnetizations about the transverse plane, magnetization rephasing begins (notice the change in axis) d) Different magnetizations rephase to produce a two-sided FID, or echo signal.

Multiple echoes can be formed by applying more transmit pulses, as done in Fast Spin Echo (FSE) imaging, where the goal is to acquire multiple echo signals before the magnetization relaxes to reduce total required imaging time. Note that an echo forms regardless of α_1 and α_2, demonstrating a situation where the classical treatment breaks down and quantum theory must be used (consider $\alpha_2 = 10°$ for Figure 2.5). When applying more than two pulses, each successive pulse can produce multiple echo signals.

GE signal formation requires time varying gradient magnetic fields to de-phase and re-phase signal components in a controlled fashion, while only using a single transmit pulse α. Gradient fields create a linear dependence between frequency and position in any desired direction. The required pulse sequence and gradient field with resulting output signal associated with a typical GE sequence is shown below, in Figure 2.6. To visualize spin magnetizations for a GE sequence, consider Figure 2.5, but apply decay rate T_2^{**} instead of T_2^*, decay rate T_2^* instead of T_2, and change the sign of the gradient field instead of applying a second RF pulse in Figure 2.5c.

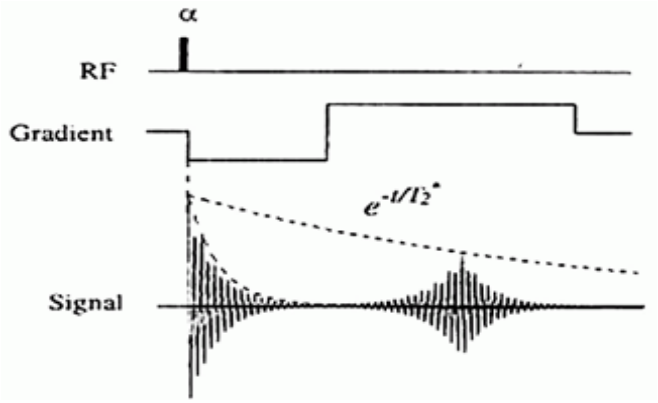

Figure 2.6 - GE pulse sequence from a single RF transmit pulse. The gradient field dephases, and then rephases the magnetization components to generate an echo (source: [40], ©2000 IEEE).

After the initial RF pulse, a negative gradient field is applied in an orthogonal direction to the selected slice, encoding phases into magnetizations through time, given in the rotating frame for *x*-gradient G_x as

$$\phi(x,t) = \gamma \int_0^t -G_x x d\hat{t} = -\gamma G_x x t \quad 0 \le t \le \tau \tag{2.29}$$

where $\phi(x,t)$ represents the phase of the magnetization vector at position *x*, for time *t*. In equation (2.29), the phase changes linearly as a function of time, meaning loss of phase coherence is linearly related to *t*. After the gradient is reversed, the output signal increases as the transverse magnetization vectors regain phase coherence. Using time period τ before inverting the gradient field, and assuming the same gradient magnitude, the phase angle as a function of position and time, after reversal, is

$$\phi(x,t) = -\gamma G_x x \tau + \gamma G_x x (t - \tau) \qquad \tau \le t \le 2\tau \tag{2.30}$$

The process of reversing the gradient field to generate an echo signal can be repeated numerous times to generate an echo train for fast imaging. The primary advantage of an SE over a GE sequence is that field non-uniformities or inhomogeneities are refocused in the SE, but not in the GE. This results in the GE sequence having a much faster upper bound signal decay rate of T_2^*, compared to the T_2 exponential signal decay rate associated with an SE sequence. The maximum FID amplitude associated with a GE sequence is given by [40]

$$A_E = M_z^0 \sin(\alpha) e^{-t/T_2^*} \tag{2.31}$$

It is also noted that for flip angle α, a GE signal will be proportional to sin(α), where an SE signal has $\sin^3(\alpha)$ dependence. This property makes GE sequences more desirable for B_1-mapping when using a surface coil for transmitting RF pulses, and SE sequences better for B_1-mapping when using a volume coil (see Appendix A for a B_1-mapping description). This is because the field magnitude of surface coils exhibits a nonlinear relationship with distance, where volume coils have little change in B_1^+ field magnitude with distance. Another property of GE sequences that can be advantageous is that less power is transmitted into the body because only one transmit pulse is required. In other words, a lower Specific Absorption Rate (SAR) is associated with GE sequences as compared with SE sequences. The SAR describes the amount of energy a region of tissue absorbs from the transmitted RF pulse. This absorbed energy dissipates in the form of heat, which can be a problematic design constraint for high $\vec{B}_0$ systems. If the SAR is too high, it is possible to permanently damage the sample tissue.

2.2.2 Frequency Encoding

The goal of Frequency Encoding (FE) in MRI is to establish a linear dependency between the origin of a signal in sample space and oscillation frequency within the sample space. During an FID or echo signal, the gradient coils are used to encode a unique frequency for each originating physical position. Here, a homogeneous main magnetic field is assumed. By ignoring a proportionality constant based on flip angle, main magnetic field strength, and receiver sensitivity, the received signal from the entire object in general is calculated as

$$V_s(t) = \left[\int_{object} \rho(r) e^{-i\gamma \vec{G}\cdot\vec{r}t} dr \right] e^{-i\omega_0 t} \tag{2.32}$$

for applied gradient field $\vec{G}$, carrier frequency ω_0, and nuclei spin density $\rho(r)$, varying as a function of position *r*. The carrier frequency can easily be removed by demodulation,

simplifying the required system circuitry. Figure 2.7 shows demodulated signals from a frequency-encoded system.

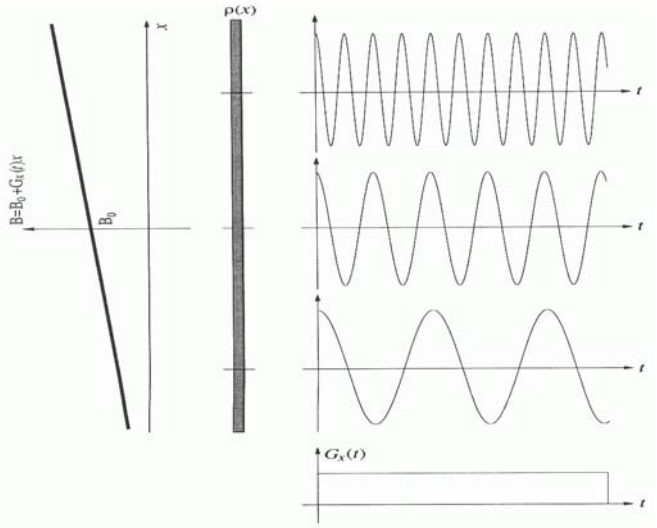

Figure 2.7 – Resulting signals from a 1D object in the presence of a frequency-encoding gradient (source: [40], ©2000 IEEE).

Note that the three gradient fields simultaneously cannot establish 3D encoding: only a plane of constant frequency can be established within a 3D object. By using the three gradient fields, the plane of constant oscillation frequency can have any desired orientation, allowing the user to acquire MRI slices of any orientation by applying a slice selection pulse with a designed bandwidth, as described in Section 2.1.6. This allows determination of one dimension for a 3D system.

After a given slice has been excited, a gradient field orthogonal to the slice selection gradient field is used to establish frequency encoding across the slice. Note that this also creates planes of constant frequency within the sample, but it is known that the received signals originated only from the selected plane, where transverse magnetizations are non-zero. This effectively determines the second dimension relating to where the received signals originated from. Next, a process is required to yield information about the third dimension, to fully determine where each signal originated from in 3D space.

2.2.3 Phase Encoding

The process of Phase Encoding (PE) simply involves applying the FE gradients to the sample, but over a very short time period, to establish a linear phase difference over different positions. Due to the spatial dependant oscillating frequencies associated with applying the gradient fields, when the gradient is turned off after time T_{pe}, each position will have a different phase angle, which can be given as (assuming $\vec{G} = G_x x\hat{z}$)

$$\phi(x) = -\gamma G_x x T_{pe} \tag{2.33}$$

The signal is phase encoded because of the linear relation between $\phi(x)$ and position *x*. As with FE, PE can be applied to any arbitrary direction. The phase encoded received signal can be calculated as

$$V_s(t) = \left[\int_{object} \rho(r) e^{-i\gamma \vec{G} \cdot r T_{pe}} dr \right] e^{-i\omega_0 t} \tag{2.34}$$

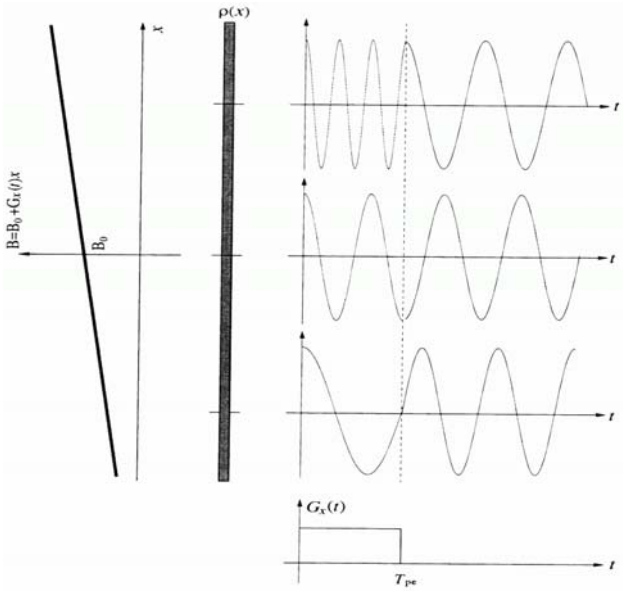

Figure 2.8 – Resultant signals from a 1D object in the presence of a phase-encoding gradient (source: [40], ©2000 IEEE).

A visual interpretation of the resulting signals for PE can be seen in Figure 2.8. Note that signals with the same frequency and phase are indistinguishable; meaning the total phase change over the object FOV cannot exceed 2π without aliasing. PE serves as

the third method of relating signals to their originating position, which is required to reconstruct an image for a selected slice within a 3D object. The mathematics behind this reconstruction requires a mapping between the frequency domain and the image domain, accomplished using the Fourier Transform.

2.2.4 *k*-Space Coverage

The role of a FE gradient $\vec{G}$ is to encode spatial information into the time domain, or *k*-space, using the FE mapping relationship

$$\vec{k} = \begin{cases} \gamma \vec{G} t / 2\pi & FID \\ \gamma \vec{G}(t - T_E)/2\pi & ECHO \end{cases} \tag{2.35}$$

for FID and echo signals respectively. To form an image, these time domain signals are transformed to the frequency domain (equivalent to the spatial domain) using the Fourier Transform. For a 2D axial imaging sequence, assuming the signal voltage was measured at the source, being the spin magnetization vector, the signal voltage can be given as

$$V_s(t) = \int_x \int_y C(r)\rho(r) e^{-i2\pi(k_x(t)\cdot x + k_y(t)\cdot y)} dxdy \tag{2.36}$$

where

$$k_x(t) = \frac{\gamma}{2\pi}\int_0^t G_x(\tau)d\tau \quad \text{and} \quad k_y(t) = \frac{\gamma}{2\pi}\int_0^t G_y(\tau)d\tau$$

where $\rho(r)$ is the spin density, and $C(r)$ gives a position dependent constant to account for $\vec{B}_1^+$ field inhomogeneities. Extracting $\rho(r)$ from $V_s(t)$ requires taking the inverse 2D Fourier transform of the signal waveform. To make this possible, a vector of $V_s(t)$ signals must be sampled, each one covering *k*-space differently, meaning a different set of gradients must be applied. This is where PE comes into play. The associated NMR image can be reconstructed through the inverse 2D Fourier transform of the *k*-space data.

Both PE and FE must be applied to adequately cover *k*-space. The PE step determines the starting position for *k*-space traversal. From here, applying a FE gradient traverses a straight line through *k*-space, assuming constant gradients are applied during signal acquisition. Each repeated PE step corresponds to another row of output image

pixels for the reconstructed image. In other words, the number of pixels in one dimension of the output image will directly correspond to the number of PE steps taken while acquiring the data (256 PE sequences gives 256 lines in the PE direction). The number of pixels associated with the FE direction is dependant on the number of sample points in the time domain and the total acquisition time.

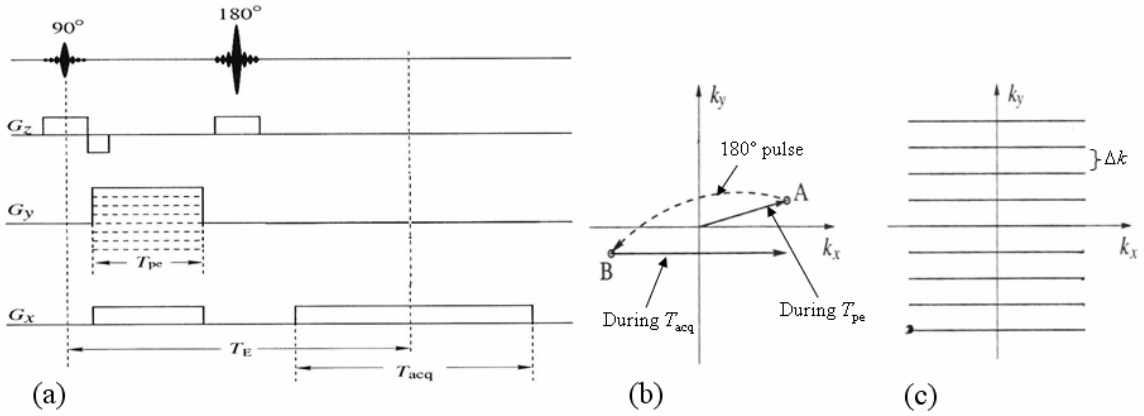

Figure 2.9 - Cartesian based k-space sampling with (a) sample SE pulse sequence required (b) k-space traversal for single pulse repetition (c) total k-space coverage from repeated PE steps (source: [40], ©2000 IEEE).

The most common 2D imaging sequences involve rectilinear, or Cartesian, *k*-space sampling as shown in Figure 2.9, or Radon transform imaging as in Figure 2.10. By changing the gradient magnitude, shown as dashed lines, different *k*-space lines can be filled allowing sufficient coverage for image reconstruction. Notice that the three different gradients applied in the sequence of Figure 2.9 are in orthogonal directions.

Both pulse sequences shown fall under the general category of SE. PE occurs during time lapse T_{pe}, where FE occurs during T_{acq}. The echo time T_E represents twice the elapsed time between the initial pulse and the second or echo pulse. The MRI system records the received signals during the acquisition time (T_{acq}).

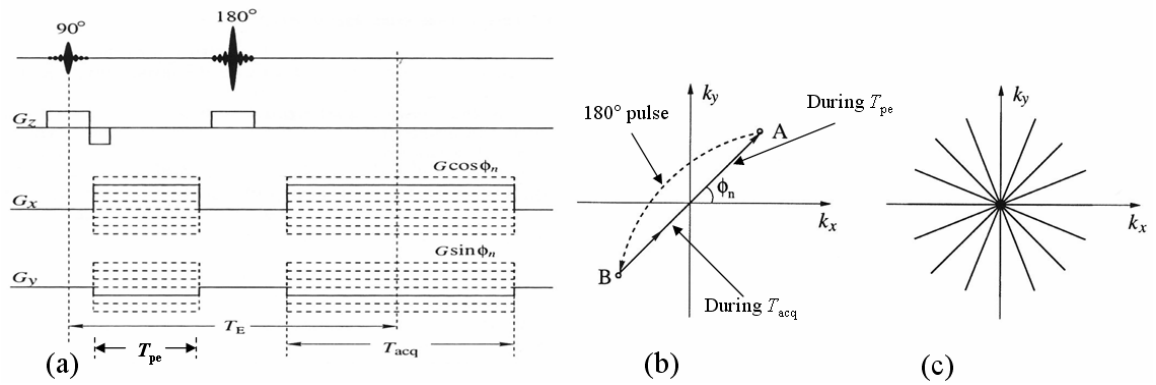

Figure 2.10 - Radon transform based imaging with (a) required SE pulse excitation sequence (b) k-space traversal from single repetition (c) total k-space coverage from the pulse sequence (source: [40], ©2000 IEEE).

Considering Cartesian based *k*-space sampling, the FOV is determined by the *k*-space difference between adjacent PE lines Δk, where image resolution is governed by the total number of PE lines. This implies that to reduce total imaging time using a constant FOV, fewer PE steps could be taken with an increased gradient step size. However, received image data becomes aliased due to spectral, or Nyquist folding if *k*-space is undersampled. By violating the Nyquist sampling theorem, components outside the baseband are folded into the baseband and become indistinguishable from those originally located within the baseband [40].

For a depiction of the resulting image when only half of the required *k*-space lines are taken, refer to Figure 2.11. To properly unfold the data, parallel imaging (explored in detail in Section 2.4.4) is required, where multiple receivers are used, each having a unique sensitivity profile over the sample space, allowing full FOV image reconstruction by applying mathematical techniques.

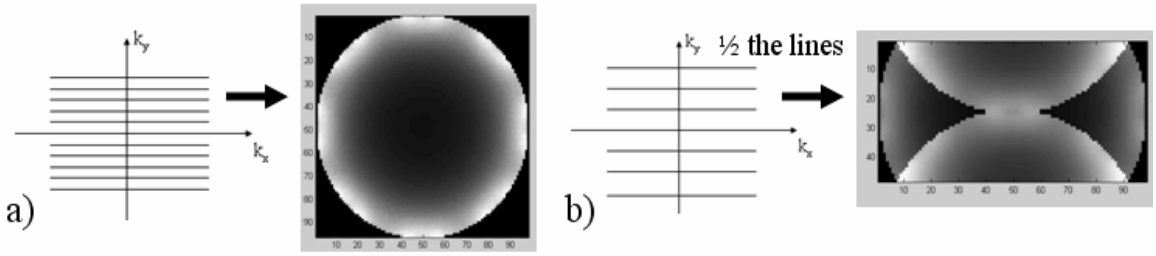

Figure 2.11 – *k*-space sampling lines and associated reconstructed image when a) enough *k*-space lines were acquired, and b) ½ the required *k*-space lines acquired with the associated aliased image, demonstrating that the spectral folding resulted in the image being folded.

2.3 MRI System Perspective

2.3.1 General System Overview

The main magnet, commonly super-conducting, is the most expensive component of an MRI system and is required to establish the homogeneous static $\vec{B}_0$ field (*z*-directed by convention). Gradient coils are used inside the magnet bore to establish a linear variation of the $\vec{B}_0$ field magnitude, which was described in detail in Section 2.1.6.

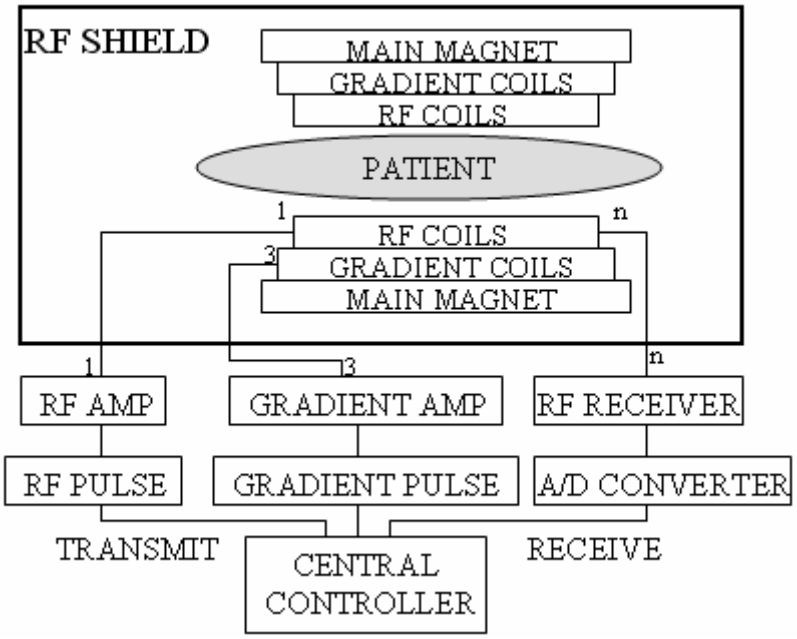

Figure 2.12 – Common depiction of a MRI system component block diagram.

RF coils are used to transmit power into the sample object and to receive emitted signals, being processes named excitation and reception respectively. This can be accomplished by a single coil design, or by two specialized designs. Refer to Figure 2.12 for a common depiction of an MRI system overview as a block diagram.

As previously described, the gradient coils enable selecting a slice plane of any orientation through the patient. The coordinate system applied for MRI imposes $\vec{B}_0$ as *z*-directed, L-R as *x*-directed, and A-P as *y*-directed, when considering a patient lying in the

cylindrical bore of the magnet. The three orthogonally directed slices are named axial for the *xy*-plane, sagittal for the *yz*-plane, and coronal for the *xz*-plane.

The noise figure, or amount of noise added by the RF components in the RF receiver system, is very important because SNR is strongly related to image quality. Typically, this system parameter is ignored during coil development because it affects all potential coil designs equally.

2.3.2 RF Coil Design Specifics

RF coils are used as both transmit and receive coils in MRI. These coils must have a high quality factor *Q* at the Larmor Frequency ω_0 to be sensitive to the NMR signals. This is important because MRI is known as a low sensitivity technique, as a small percentage of sample nuclei emit the measurable signal (nine in a million for a 3T system), which is governed by equation (2.8). Currently, clinical MRI systems are equipped with a single transmitter channel, but an array of receiving lines, as shown in Figure 2.12. Future systems will likely incorporate an array of transmitter coils, each with an individual RF pulse and amplifier line. The two main types of coil architectures are volume and surface coils.

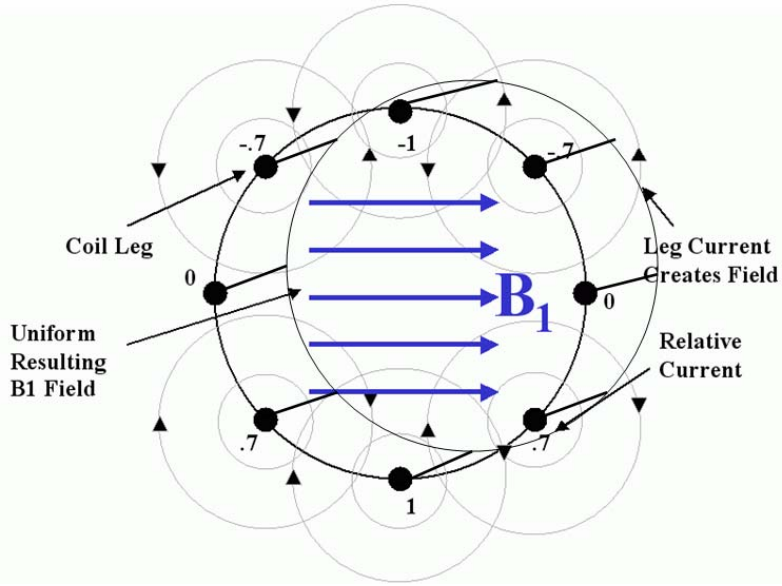

Figure 2.13 - Eight leg birdcage coil current distributions with resulting B_1 field.

Volume coils are typically characterized as producing a uniform $\vec{B}_1$ field. A birdcage coil is a typical volume coil design, shown in Figure 2.13 with relative current distributions. Having a uniform $\vec{B}_1$ field makes volume coils ideal for transmit coils, because uniform excitation is usually desired. Surface coils are advantageous for applications in parallel imaging, where nonuniform field distributions can be exploited (explained in Section 2.4.4). Note that an array of surface coils can be oriented to cover a volume, but the overall resultant $\vec{B}_1$ field would not be uniform, as seen from a birdcage coil. This research is focused on a receive-only coil, where parallel imaging is incorporated; hence the birdcage coil will no longer be considered. To make a resonating surface coil, capacitors are placed around a conductive trace, which is inherently inductive, to get a resonance frequency according to

$$\omega_{res} = \frac{1}{\sqrt{L_{eff} C_{eff}}} \tag{2.37}$$

where effective loop inductance L_{eff}, and effective capacitance C_{eff}, are required to apply this relation. In MRI, the RF coil is tuned to $\omega_{res} = \omega_0$, as required by equation (2.4). To measure the coil performance as a resonator, a designer must calculate its quality factor Q, both when loaded with a typical sample and unloaded (in free space), being named Q_L and Q_U respectively. These quantities can be calculated according to

$$Q_L = \frac{\omega L_{eff}}{R_s + r_c} = \frac{\omega_0}{\Delta\omega} \qquad\qquad Q_U = \frac{\omega L_{eff}}{r_c} = \frac{\omega_0}{\Delta\omega} \tag{2.38}$$

where $\Delta\omega$ is the 3dB bandwidth. Equivalent coil resistance and other non-sample effects are lumped within r_c, where as R_s is the effective resistance of the sample. Example effects accounted for in r_c are conductor skin effect loss, interaction between neighbouring coils, dielectric losses in the distributed capacitors and eddy current losses in the shielding of metallic objects close to the coil's magnetic field. Because it is desirable to maximize power deposition in the sample, and by reciprocity, maximize the receive sensitivity of the coil, a good coil design will exhibit $Q_L << Q_U$.

2.3.3 Phased Array Coils

A phased array coil is simply a set of surface coils, each electrically isolated from the others. Separate and independent signals are received from each RF coil, and then combined to improve the SNR over a large FOV. Here, phased array coils are considered for use as receiver coils. For a cylindrical array of surface coils having a similar overall geometry to a birdcage design, similar SNR values are found in an axial slice center, but the phased array will have far superior SNR near the image periphery (i.e. close to the array). A general rule of thumb is that the diameter of a surface coil corresponds to the optimal depth for signal sensitivity, where the sensitivity falls off as the distance squared. Small surface coils yield better SNR at shallow depths compared to large coils, indicating a stronger $\vec{B}_1^-$ field at that position. Another advantage over volume coils involves using parallel imaging techniques to reduce imaging time (discussed in Section 2.4.4).

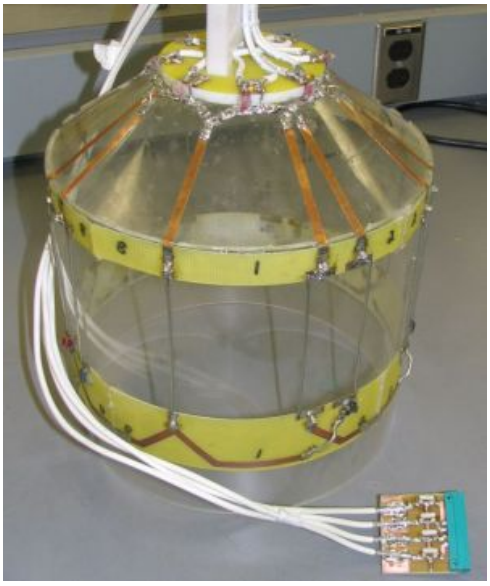

Figure 2.14 - Sample four-channel array coil designed by the author for human head imaging at 1.5T. This coil used eight different loops combined to form four channels [56].

Parallel imaging is of particular interest in cardiac imaging, where patient motion can cause significant image degradation. The primary disadvantage of phased array designs is the requirement for many independent receiver system channels (preamplifier and RF components), which translates to increased costs. For an example of how surface

coils can be used for volume imaging, Figure 2.14 depicts a sample phased array volume coil implemented for human head imaging, which was designed by the author for a previous project [56].

2.4 MRI Image Analysis

2.4.1 SNR Calculation

RF coil performance in MRI is characterized by the SNR associated with that coil, which is inversely proportional to the Root Mean Square (RMS) of the thermal or Johnson noise voltage measured across the coil terminals. Thermal noise voltage is governed by Planke's blackbody radiation law, given as [48]

$$V_n = \sqrt{\frac{4hf\Delta fR}{e^{hf/k_BT} - 1}} \tag{2.39}$$

where Δf is the system bandwidth, f is the center frequency of the bandwidth, and R is the effective resistance for the system. The Johnson noise voltage represents the RMS of the thermal noise voltage measured at the coil terminals. By taking the first two terms of the Taylor series expansion of the exponential, equation (2.39) reduces to

$$V_n = \sqrt{4k_BT\Delta fR} \tag{2.40}$$

To simplify analysis, the effective resistance R can be broken into series sample resistance R_s and non-sample resistance r_c. The non-sample resistance includes many noise sources such as the coil itself, external circuitry and coil housing. Typically in RF coil design, the non-sample resistance is treated as a constant. For research of this thesis, it was reduced to only include the resistance of the coil itself. The relation between sample resistance to loaded and unloaded Q values is given as

$$R = R_s + r_c = R_s\left(1 + \frac{Q_L}{Q_U - Q_L}\right) \tag{2.41}$$

For resistance R_s, noise is caused by time-averaged losses in the sample from sinusoidal unit current I_o. Thus, applying Ohm's law to obtain the time-averaged losses in the sample for sinusoidal unit current results in

$$V_n = \sqrt{4k_B T \Delta f P_{abs} / I_o^2} \tag{2.42}$$

where I_o describes an induced unit current associated with the imaging experiment and P_{abs} describes the absorbed power in the sample. The absorbed power can be calculated from the induced electric field over the entire sample as [10]

$$P_{abs} = \frac{1}{2}\sum_N \sigma(E_x^2 + E_y^2 + E_z^2)\Delta x \Delta y \Delta z \tag{2.43}$$

for isotropic conductivity σ. This treatment is useful in a simulated problem space, where the $\vec{E}$ fields are solved throughout the 3D sample. This concludes calculation of the noise voltage and related absorbed power.

Next, the useful signal strength must be derived. To calculate the imaging signal strength, the Principle of Reciprocity [25] is used to describe the relationship between a bulk nuclear magnetic moment, or magnetization per unit volume $\vec{M}dV$ and the measurable signal V_s in an RF coil as seen in Figure 2.15. The induced voltage in a loop by oscillating magnetic moment $\vec{M}$ is proportional to the magnetic field $\vec{B}$ at, and parallel to, $\vec{M}$, that the loop would produce if oscillating unit current $I_0 \cos(\omega t + \Phi)$ were passed through the loop [25]. The reciprocity equation can be stated as

$$|V_s| = \frac{\omega \vec{M} \bullet \vec{B}_P}{I_o} \tag{2.44}$$

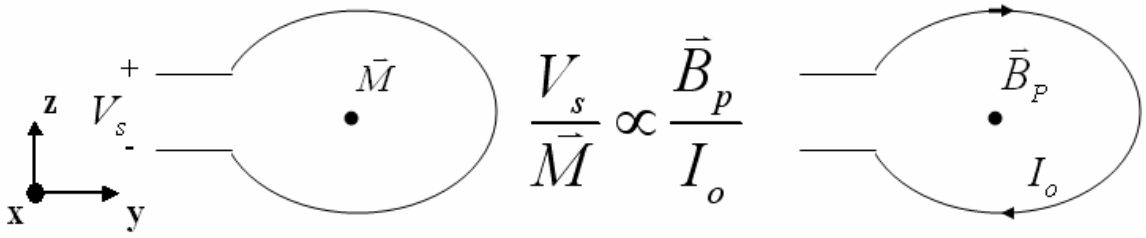

Figure 2.15 - Illustration of the Principle of Reciprocity being applied to RF coils.

In equation (2.44), $\vec{B}_p$ is the $\vec{B}$ field perpendicular to the plane of the loop. Assuming that the loop is centered on the *x*-axis and in the *yz*-plane, any *z*-directed magnetic field does not influence the NMR signal, thus can be ignored. Both $\vec{M}$ and $\vec{B}_p$ in this case are purely *x*-directed. By applying magnetic field $\vec{B}_0$, a circularly polarized field is created in the *xy*-plane. To complete the description, a second coil is required in the *xz*-plane to detect *x*-directed magnetization. Here, the applied current $I_0 \cos(\omega t)$ creates equivalent point source magnetization for the loop that varies as $I_0 A \cos(\omega t)$, for loop cross sectional area *A*. For the time being, the fields are calculated in a general sense, meaning not from a transmission or reception perspective. This is because they can be considered as one and the same by applying the Principle of Reciprocity. The induced Electro-Motive Force (EMF) from sample conduction and displacement currents, as calculated separately for each dimension from Faraday's Law, are given as

$$\begin{aligned} V_x &= -A\frac{dB_{1X}}{dt} = \omega C_{ox} I_o A^2 \sin(\omega t + \theta_1) \\ V_y &= -A\frac{dB_{1Y}}{dt} = \omega C_{oy} I_o A^2 \sin(\omega t + \theta_2) \end{aligned} \tag{2.45}$$

where C_{ox} and C_{oy} are position and frequency dependent attenuation factors, θ_1 and θ_2 are position and frequency dependent phase shifts produced by conduction and displacement currents that go to zero for low frequency problems. Now, changing to a reference frame rotating at the Larmor Frequency ($\omega_0 = \gamma |\vec{B}_0|$), denoted by subscript *rot*, in both the positive and negative rotating frames, the magnetic fields are given as

$$B_{1x,rot}^{+} = B_{1x}\cos\omega t + B_{1y}\sin\omega t \approx \frac{I_0 A}{2}\left[C_{0x}\cos(\theta_1) - C_{0y}\sin(\theta_2)\right] \tag{2.46}$$

$$B_{1y,rot}^{+} = -B_{1x}\sin\omega t + B_{1y}\cos\omega t \approx \frac{I_0 A}{2}\left[C_{0x}\sin(\theta_1) + C_{0y}\cos(\theta_2)\right] \tag{2.47}$$

$$B_{1x,rot}^{-} = B_{1x}\cos\omega t - B_{1y}\sin\omega t \approx \frac{I_0 A}{2}\left[C_{0x}\cos(\theta_1) + C_{0y}\sin(\theta_2)\right] \tag{2.48}$$

$$B_{1y,rot}^{-} = B_{1x}\sin\omega t + B_{1y}\cos\omega t \approx \frac{I_0 A}{2}\left[-C_{0x}\sin(\theta_1) + C_{0y}\cos(\theta_2)\right] \tag{2.49}$$

The above equations were simplified using equation (2.45), resulting in products of sines and cosines. The resulting terms either have no time variation, or time variation according to $2\omega t$, where the latter terms vary too quickly to influence the NMR system, as such are neglected. A trigonometric expansion is applied to get the resulting, simplified, approximated equations (2.46) to (2.49). The equations become simpler yet if a polar representation is used by applying complex numbers to form the same relations [25], changing magnetic moment $\vec{M}$ to be complex as $M_c = m + im_c = AI_o e^{i\omega t}$.

By defining the real numbers along the rotating *x*-axis and the imaginary numbers along the rotating *y*-axis, the separate *x* and *y* components from equations (2.46) to (2.49) can be combined with respect to the positively and negatively rotating frames. This application results in two circularly polarized rotating fields calculated as

$$\begin{aligned} B_{1,rot,c}^{+} &= B_{1x,rot}^{+} + iB_{1y,rot}^{+} = \frac{b_{1x} + ib_{1y}}{2} \\ B_{1,rot,c}^{-} &= B_{1x,rot}^{-} + iB_{1y,rot}^{-} = \frac{(b_{1x} - ib_{1y})^*}{2} \end{aligned} \tag{2.50}$$

where

$$\begin{aligned} b_{1x} &= C_{ox} A I_o e^{i\theta_1} \\ b_{1y} &= C_{oy} A I_o e^{i\theta_2} \end{aligned} \tag{2.51}$$

Note that equation (2.51) is not typically used in MRI analysis. In simulated situations, b_{1x} and b_{1y} are parameters solved for throughout the ROI, simply being the magnetic field components, which are found by solving Maxwell's equations.

Experimental results will have pixel intensities proportional to $\vec{B}_{1,rot,c}^{+} \bullet \vec{B}_{1,rot,c}^{-*}$ (discussed shortly), where there is no need to solve equation (2.51) because the transmit field and receive sensitivities are already known.

Now, the focus is moved to a simple pulse NMR experiment, where computation of the transmit field and receive sensitivity as separate entities is desired. Here, the convention that the magnetization vectors $\vec{M}$ are precessing in the positively rotating frame of reference is adapted. For an applied magnetic field to perturb this magnetization vector according to the Bloch equation, the excitation field must be rotating in the same direction, at the same frequency, described by equation (2.13). This means that the transmit field must be $\vec{B}_{1,rot,c}^{+}$. This excitation field is applied to equation (2.12). Assuming that the $\vec{B}_0$ field is *z*-directed, relaxation effects (T_1 and T_2) are ignored, and a small flip angle ($\alpha < 10°$) to approximate the Bloch equation as linear, simplified Bloch equations for the rotating frame can be separated into relevant components (recall that the system is insensitive to *z*-directed perturbations), which can be given as

$$\frac{dM_{x,rot}^{+}}{dt} \approx \gamma B_{1y,rot}^{+} M_z \qquad \frac{dM_{y,rot}^{+}}{dt} \approx -\gamma B_{1x,rot}^{+} M_z \tag{2.52}$$

By fixing the transmit field, the Principle of Reciprocity is now applied to determine the corresponding receive sensitivity field. After applying the $\vec{B}_1^{+}$ transmit field over a determined time duration τ, the resulting magnetization is

$$M_{rot,c}^{+} = \gamma\tau M_z^0 B_{1y,rot}^{+} - i\gamma\tau M_z^0 B_{1x,rot}^{+} = -i\gamma\tau M_z^0 B_{1,rot,c}^{+} \tag{2.53}$$

Using the change in magnetization with Faraday's Law to calculate the induced EMF in the coil, the EMF induced by the *x* and *y* components of nuclear magnetization separately are

$$\begin{aligned} V_x &= \omega C_{ox} I_o A^2 \left\{ \left(\frac{M^+_{x,rot}}{I_o A} \right) \sin(\omega t + \theta_1) + \left(\frac{M^+_{y,rot}}{I_o A} \right) \cos(\omega t + \theta_1) \right\} \\ V_y &= \omega C_{oy} I_o A^2 \left\{ -\left(\frac{M^+_{x,rot}}{I_o A} \right) \cos(\omega t + \theta_2) + \left(\frac{M^+_{y,rot}}{I_o A} \right) \sin(\omega t + \theta_2) \right\} \end{aligned} \tag{2.54}$$

The total voltage $V_s(t)$ is calculated as the superposition of these two voltages. Employing a trigonometric expansion, and still utilizing magnetizations in the rotating frame, results in

$$V_s(t) = \omega A \begin{Bmatrix} \left[M^+_{x,rot} \left(C_{ox} \sin\theta_1 - C_{oy} \cos\theta_2 \right) + M^+_{y,rot} \left(C_{ox} \cos\theta_1 + C_{oy} \sin\theta_2 \right) \right] \cos\omega t \\ + \left[M^+_{x,rot} \left(C_{ox} \cos\theta_1 + C_{oy} \sin\theta_2 \right) + M^+_{y,rot} \left(-C_{ox} \sin\theta_1 + C_{oy} \cos\theta_2 \right) \right] \sin\omega t \end{Bmatrix} \tag{2.55}$$

Note that the terms in the outermost parentheses are equal to the fields in the negatively rotating frame, more specifically

$$\begin{aligned} B^-_{1x,rot} &\approx \frac{AI_o}{2} \left[C_{ox} \cos\theta_1 + C_{oy} \sin\theta_2 \right] \\ B^-_{1y,rot} &\approx \frac{AI_o}{2} \left[-C_{ox} \sin\theta_1 + C_{oy} \cos\theta_2 \right] \end{aligned} \tag{2.56}$$

This demonstrates that while the magnetization precesses positively, the negatively precessing field from a hypothetical unit current I_o should be used for calculations of received signal strength. This is important for employing the Principle of Reciprocity. Now returning to the laboratory frame (non-rotating), the induced EMF after applying excitation field $\vec{B}_1^+$ for time τ is calculated as

$$V_{s,c} = -\frac{i2\omega\gamma\tau M_z^0 \vec{B}^+_{1,c} \vec{B}^{-*}_{1,c}}{I_o} \tag{2.57}$$

To extend this voltage equation to an NMR system, a few small changes are required. Still approximating the Bloch equation as linear, the flip angle α is calculated to be $\gamma\tau\vec{B}^+_{1,rot,c}$, where the available transverse signal is given by the sin of that angle. The real signal voltage across the terminals of the receiver is given by

$$|V_s| = \frac{2\omega M_z^0 \,|\sin(\gamma\tau\vec{B}_{1,rot,c}^{+})\vec{B}_{1,rot,c}^{-*}|}{I_o} \tag{2.58}$$

Finally, the resulting SNR for a single RF pulse sequence is calculated by using equations (2.42) and (2.58) to yield

$$SNR \overset{\Delta}{=} \frac{|V_s|}{V_n} = \frac{2\omega M_z^0 \,|\sin(\gamma\tau\vec{B}_{1,rot,c}^{+})\vec{B}_{1,rot,c}^{-*}|}{\sqrt{4kT\Delta f P_{abs}}} \tag{2.59}$$

For notational simplicity, $\vec{B}_1^+$ and $\vec{B}_1^-$ will be used for the remainder of this thesis instead of $\vec{B}_{1,rot,c}^{+}$ and $\vec{B}_{1,rot,c}^{-}$, respectively. An example of a single pulse sequence is a GE pulse. This SNR equation can be easily extended to multi-pulse sequences such as a SE. Equation (2.59) is fundamental for an RF coil designer. For a given system, the $\vec{B}_1^+$ field must be computed for transmit coil design, where both the $\vec{B}_1^-$ field and P_{abs} are required for receive coil design evaluation, while all other variables can be treated as constants in each case.

2.4.2 Signal Coupling with Phased Arrays

A very important design step for ensuring good SNR in array coils involves minimizing the mutual coupling between individual loops. Mutual inductance will cause noise and NMR signal to transfer from one loop to another, inhibiting performance as a parallel structure by raising the effective noise floor.

A transformer-based model of two different loops is shown in Figure 2.16. Coil interactions are minimized by removing inductive coupling between the coils ($k = 0$) or by reducing the current flowing on the loops. Current flow is reduced by imposing a high impedance in the loop, which can be accomplished by using low input impedance preamplifiers, meaning $R_p \leq 3\Omega$. Inductive coupling removal is accomplished for adjacent loops either through overlapping the two coils of concern, or by using a shared capacitance to counteract the mutual inductance between them. When tuned properly, the

shared capacitor, which must be placed on a shared edge between the two loops being decoupled, will not allow current flow between the loops.

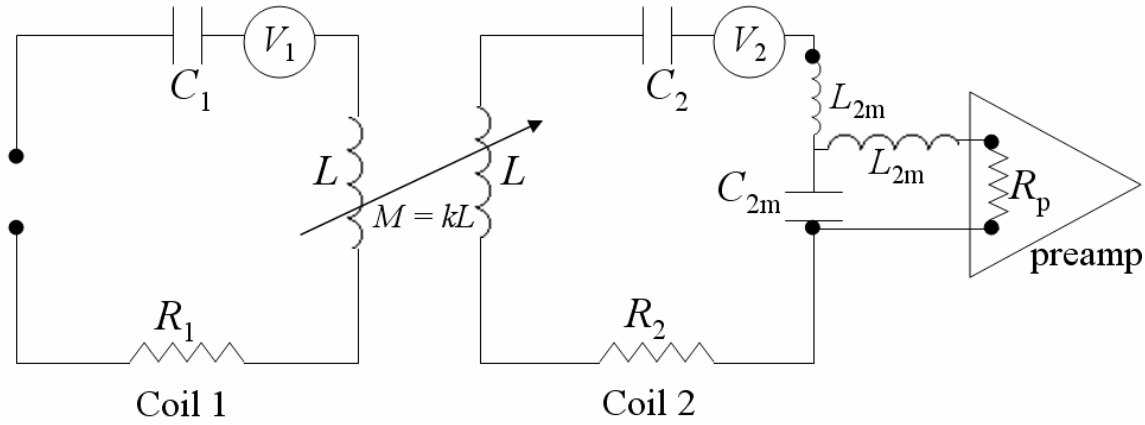

Figure 2.16 - Transformer based model for surface coil interactions and the preamplifier matching network. V_1 and V_2 are NMR induced voltages in the coils.

By using a matching network with the low input impedance preamplifiers, transforming a high impedance to the loop, both the signal current and noise current are essentially zeroed, allowing us to measure the induced voltage across the two effective terminals shown for Coil 2 without detrimental noise signal crosstalk. Because the noise signal is sample dominated, reducing the current flow affects both the desired and undesired signals equally, thus will not change the output SNR of any single coil in isolation.

The high impedance matching process is now explained, in referring to Figure 2.16 for corresponding variable names. It is assumed that both coils are tuned to the system resonant frequency ω_0, as seen across their respective terminals looking into the coil in isolation ($M = 0$). Considering Coil 2 in isolation, the impedance as seen across the two terminals looking into the pre-amp is given as

$$Z_2 = i\omega_0 L_{2m} - \frac{i}{\omega_0 C_{2m}} + \frac{L_{2m}/C_{2m}}{R_p} \tag{2.60}$$

Resonance must be established within the matching circuit itself (L_{2m} and C_{2m}), as well as matching this to the impedance the pre-amp is expecting. For convenient measurement with a Vector Network Analyzer (VNA), pre-amps are designed to expect a

$50\,\Omega$ impedance, making the resonance and matching requirements for the coil to transform the series resistance R_2, respectively, according to

$$\omega_0 L_{2m} = \frac{1}{\omega_0 C_{2m}} \tag{2.61}$$

and

$$\frac{1}{\omega_0 C_{2m}} = \sqrt{50 R_2} \tag{2.62}$$

which means

$$Z_2 = \frac{X_{2m}^2}{R_p} = \frac{L_{2m} / C_{2m}}{R_p} \tag{2.63}$$

After applying equation (2.61) to (2.60), notice that if the input impedance of the preamplifier was near zero ($R_p \approx 0$), the impedance of the loop across the terminals (Z_2) would be very large, meaning a very small current flow in the coil. MRI signals would still be properly transferred to the preamplifier, because both the signal and the noise voltages would be reduced. This high impedance allows the coils to receive signals independently, without noise and signal coupling.

Now, consider Coil 1 as viewed across the two terminals not in isolation. The series impedance when the second coil connected to a preamplifier is

$$Z_1 = R_1 + \frac{(\omega_0 M)^2}{R_2 + Z_2} \tag{2.64}$$

which becomes

$$Z_1 = R_1 + \frac{\omega_0^2 L^2 k^2}{R_2 + (L_{2m} / C_{2m}) / R_p} \tag{2.65}$$

making clear the noise power coupling between the two loops. By either eliminating the mutual inductance, accomplished by making coupling constant $k = 0$ (applying loop overlap or using a shared capacitor), or zeroing the preamplifier input impedance ($R_p \approx 0$), the two loops become perfectly electrically isolated. Accounting for the coupling contributions, the NMR signal received at the terminals of Coil 1 would be

$$V_{Coil1} = V_1 - V_2 \frac{i\omega_0 Lk}{R_2 + (1/\omega_0 C_{2m})^2 / R_p} \tag{2.66}$$

where again, to establish isolated signals between the two coils, it is desired to eliminate any voltage from the second coil as received from the first.

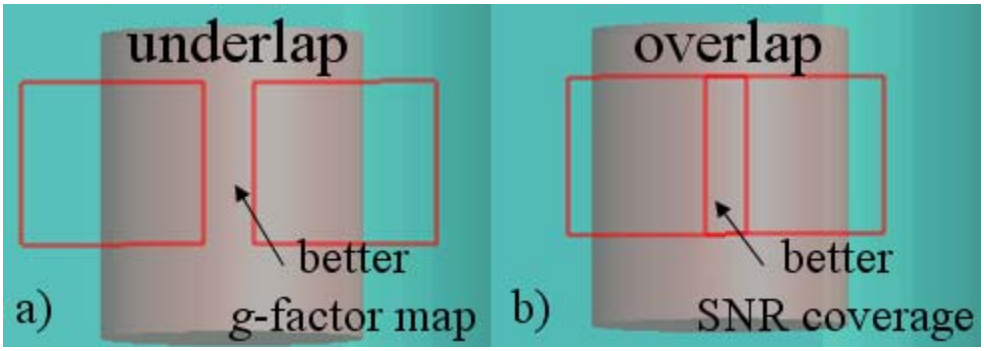

Figure 2.17 – Illustrative comparison between neighbouring coil configuration options applying a) underlapping and b) overlapping between the conductive traces of adjacent loops.

Every individual coil requires its own preamplifier, matching network and RF components for data acquisition. For removing inductive coupling by applying overlap, circular loops should have centers separated by 3/4 of their diameter, while square loops must be separated by 9/10 of their diameter [54]. Conductor traces are shown for two adjacent coils, when applying underlap and overlap in Figure 2.17a and b), respectively. The amount of overlap to apply for irregularly-shaped loops must be determined through experiment or analysis. Note that it is not possible to overlap all loops for an array of more than three elements, and therefore alternative decoupling techniques must be used.

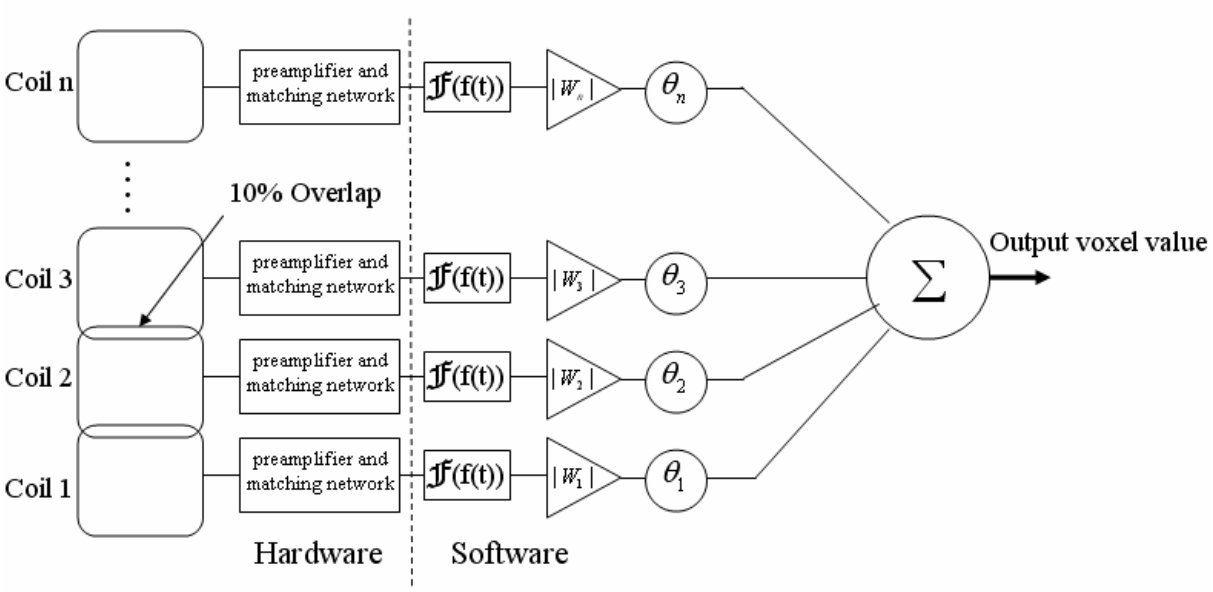

Figure 2.18 – Block diagram for a phased array receiver system.

For a block diagram of a phased array receiver system, refer to Figure 2.18. The low input impedance preamplifiers are used to minimize current flow by imposing a high impedance on the loop, thus very little noise or NMR signal is coupled to other coils [54]. The received signals can be combined based on a variety of techniques, the best being a matched filter weighting, where the weighting coefficients $W_i = |W_i| e^{i\theta_i}$ are both coil and volume element, or voxel, specific (discussed further shortly).

2.4.3 Signal Combining with Phased Arrays

The process of combining the simultaneously acquired data signals to form a single composite image is now examined. Although there are many different potential signal combining methods, this thesis outlines the Sum-of-Squares (SoS) method and a matched filter weighted, or Roemer optimal method for combining complex quadrature data. The advantage of the SoS approach is that the noise correlation matrix is not required, with the disadvantage that composite SNR is sacrificed.

First, the noise correlation matrix Ψ must be calculated. This matrix describes how much signal and noise data received by coil *i* gets transferred to coil *j* through resistive coupling. Each element of this matrix represents a noise power between two

coils. Similar to calculating the sample noise from a single coil (refer to equation (2.43)), a noise power between loops *i* and *j* over a uniformly conductive sample is defined as

$$P_{abs,ij} = \int_V \sigma(\vec{E}_i(x,y,z) \cdot \vec{E}_j(x,y,z))dV \tag{2.67}$$

Note that the above equation is only solvable when the 3D $\vec{E}$ fields and associated conductivities are known throughout the sample volume, as is the case in a simulation environment. For determining mutual noise power between physically realized coils, voltage signals for both coils must be acquired over a time period *T* when the sample is not excited. A more accurate correlated noise power value will result by choosing a longer data acquisition period *T*. The effective correlated noise contribution is extracted from a time averaged multiplication of the two voltages as

$$P_{abs,ij}^{meas,voltage} = \frac{1}{T}\int_{-T/2}^{T/2} V_i(t)V_j(t)dt \tag{2.68}$$

By special application of Parseval's Theorem [32] to the above equation, an equivalent experimental approach can be found for determining correlated noise for an array coil. This requires taking output intensity images from two different coils, named I_i and I_j, which were acquired without sample excitation, having number of pixels *n* by *m*. Each pixel in the image domain corresponds to sample dimension Δx and Δy in the physical sample respectively. Taking the two noise images, the correlated noise power can be extrapolated through [62]

$$P_{abs,ij}^{meas,image} = \frac{1}{nm\Delta x\Delta y}\sum_{a=0}^{n}\sum_{b=0}^{m} I_i(a\Delta x, b\Delta y)I_j(a\Delta x, b\Delta y) \tag{2.69}$$

The absorbed power calculated from equations (2.68) and (2.69) will be different by a scaling constant, which can be ignored here because relative SNR calculations are considered. Next, using all possible correlated noise powers, the complete noise correlation matrix is created, which contains all information about correlated and uncorrelated noise between different elements in the array. Each matrix element $P_{abs,ij}$

represents the added effective noise power when coils *i* and *j* are used, hence the correlated noise between the coils. The electric coupling coefficient k_e, also known as normalized noise correlation coefficient, is defined as

$$k_{e,ij} = \frac{P_{abs,ij}}{\sqrt{P_{abs,ii} P_{abs,jj}}} \tag{2.70}$$

For an array of *n* elements, the non-normalized and normalized noise correlation matrices, respectively, are given as

$$\Psi = \begin{bmatrix} P_{abs,11} & \cdots & P_{abs,1n} \\ \vdots & P_{abs,ii} & \vdots \\ P_{abs,n1} & \cdots & P_{abs,nn} \end{bmatrix} \tag{2.71}$$

and

$$\Psi_{Norm} = \begin{bmatrix} k_{e,11} & \cdots & k_{e,1n} \\ \vdots & k_{e,ii} & \vdots \\ k_{e,n1} & \cdots & k_{e,nn} \end{bmatrix} \tag{2.72}$$

Next, methods for forming the composite image are explored. The composite image can be calculated by making a weighted combination of the individual images for pixel position *p* from each coil element. For this, a vector for each pixel is formed containing image values, or signal values from each coil, named $\vec{p}_p$. The first reconstruction technique, called a Sum-of-Squares (SoS), forces the noise to be a constant value throughout the entire composite image [23]. Computation of a composite pixel value is set up as an optimization problem, where SNR is maximized subject to a scaling constraint. Also, only the diagonal component of the noise correlation matrix is used $\Psi_D = \Psi \cdot eye(n)$, applying identity matrix *eye(n)*, providing scaling only to the self-correlations (coil *i* to coil *i*) of the array. Weighting factors $w_{i,p}$ are defined for each coil at the pixel location, thus creating vector $\vec{w}_p$. Based on the weighted composite signal valued $\vec{w}_p^T \vec{p}_p$, the SNR for that pixel is given by [23]

$$SNR_p^{SoS} = \frac{\vec{w}_p^T \vec{p}_p}{\sqrt{\vec{w}_p^T \Psi_D \vec{w}_p}} \tag{2.73}$$

where the variance can be shown to be

$$\text{var} = \vec{w}_p^T \Psi_D \vec{w}_p \tag{2.74}$$

From here, SNR is optimized by finding the maximum of $\vec{w}_p^T \vec{p}_p$, while constraining the variance to be equal to a constant β. Using a Lagrange multiplier λ_L, $\vec{w}_p$ is solved for by equating the partial derivatives with respect to $w_{i,p}$ with zero, using the function

$$g(\vec{w}_p) = \vec{w}_p^T \vec{p}_p + \lambda_L \vec{w}_p^T \Psi_D \vec{w}_p \tag{2.75}$$

Using $\beta = \vec{w}_p^T \Psi_D \vec{w}_p$ to eliminate λ_L, the weighting vector becomes [23]

$$\vec{w}_p = \frac{\sqrt{\beta}\, \vec{p}_p^T \Psi_D^{-1}}{\sqrt{\vec{p}_p^T \Psi_D^{-1} \vec{p}_p^*}} \tag{2.76}$$

Finally, equation (2.76) is inserted to (2.73) to get the SoS-SNR as

$$SNR_p^{SoS} = \sqrt{\vec{p}_p^T \Psi_D^{-1} \vec{p}_p^*} \tag{2.77}$$

If calculating Ψ_D is not possible, estimating the noise correlation matrix by the identity matrix *eye(n)* provides reasonable results, which is called the simple SoS approach, computed according to

$$SNR_p^{simpleSoS} = \sqrt{\vec{p}_p^T \vec{p}_p^*} \tag{2.78}$$

When not using the full noise correlation matrix, effectively ignoring coupling between different elements, a strong SNR decrease will be observed near the coils, where smaller decreases result far away from the array [36]. For an SNR computation approach using the full matrix Ψ, the sensitivity map from all coils is used to form a separate vector for each pixel position, named $\vec{S}_p$, having the same length as the number of array elements. The sensitivity map can be thought of as the individual SNR that the coil would receive from a uniform sample. This sensitivity-weighting vector replaces the second

image profile of equation (2.77). The composite SNR can be derived in a similar manner to that done for the SoS pixel intensity [54]. This method is known as a matched filter weighted or Roemer optimal approach, and is calculated by

$$SNR_p^{OPT} = \sqrt{\vec{p}_p^{\,T} \Psi^{-1} \vec{S}_p^{\,*}} \tag{2.79}$$

for composite image intensity SNR_p^{OPT}. The composite image is acquired by solving equation (2.79) for every resultant image pixel. After which, the data can be processed as if acquired from a single coil. Effectively, the SoS approach weights each pixel by its own signal, where the optimal approach uses a standardized sensitivity. Although fewer computations are required for equation (2.77), the resultant SNR will not be as good as that if equation (2.79) were used.

2.4.4 Sensitivity Encoding

SENSitivity Encoding (SENSE) is a parallel imaging technique for reconstructing a full FOV image from a set of aliased images using an array of receiver coils. The benefit of this technology is a reduction in acquisition time, achieved by taking fewer PE steps to acquire the data. As applied to MRI, the direction of aliasing will be that of the PE direction(s). Here, SENSE is analyzed for 2D imaging sequences, where the single PE direction is the *y*-direction. Note that SENSE can be extended to multiple directions, which is useful for 3D imaging sequences, where two PE directions are used, thus 2D SENSE can be applied [74].

Employing Cartesian sampling, an aliased image is acquired by eliminating some of the PE lines, as shown in Figure 2.11. The resulting image appears folded as shown in Figure 2.19, where reduction factor *R* is defined to describe the degree of image folding relative to the unfolded image. For example, taking one third of the total required PE steps corresponds to $R = 3$. What this means is, applying an $R = 4$ pulse sequence enables a timesaving of 75% relative to an $R = 1$ sequence. Using an array of receiver coils, multiple aliased images are acquired, each encoded with spatial sensitivity information

specific to the corresponding coils' $\vec{B}_1^-$ field. From each coil element, an aliased image and its sensitivity map is required to unfold the superposition of signals [49]. Signal separation is only possible when individual coil sensitivities show different weights throughout the image region, as surface coils do.

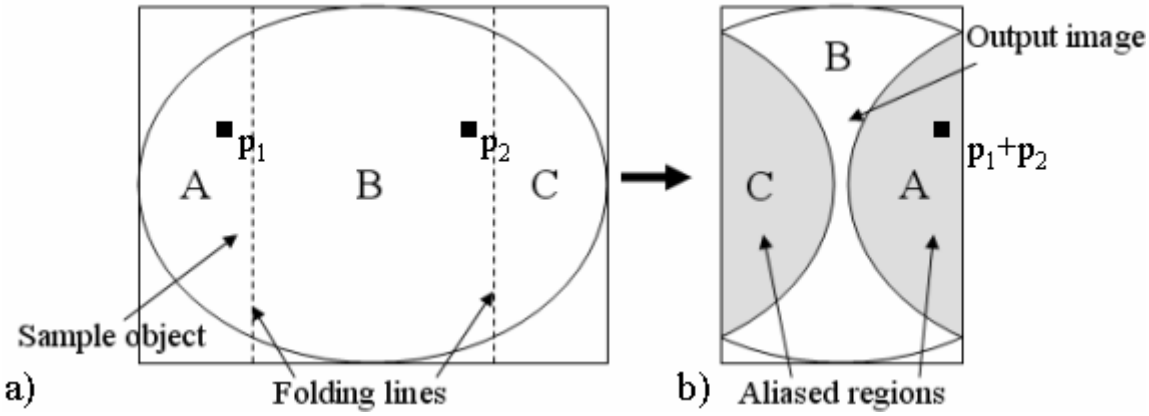

Figure 2.19 – a) Full FOV image showing folding lines related to reduction factor $R = 2$, and b) Aliased image caused by violating Nyquist sampling rate showing superimposed pixels.

A sensitivity map S is essentially a full FOV image for a given receive coil used as a gold standard measurement of the $\vec{B}_1^-$ field strength. Using reliable information is difficult, as the sensitivity map will change depending on the dielectric sample being imaged.

The *g*-factor can be thought of as representing the ability of the coil configuration to separate aliased pixels. Mathematically, it represents a scaling factor for increasing the noise level, which will be different for every pixel in the output image. Thus, *g*-factor maps provide a good design constraint for coil arrays dedicated to SENSE imaging. For ideal performance in parallel imaging, it is desirable for the sensitivity maps in an array to be as different from one another as possible for the slice of interest. This will yield improved *g*-factor maps.

Also, SENSE performance will be enhanced if the coils' plane of symmetry (if it exists) is not parallel with the PE direction, yielding different folded sensitivity maps. These general design guidelines will yield the best *g*-factor map. A sample four-element coil configuration with associated sensitivity maps is shown in Figure 2.20. Notice that

no coil is oriented such that its plane of symmetry is parallel to the labeled PE direction, shown both by its electrical trace configuration and associated sensitivity maps.

With knowledge of *R*, it is known which pixels from the full FOV were superimposed for the reduced image, as shown in Figure 2.19. A sensitivity matrix $S_{p,c\times s}$ must be created for each folded pixel *p*, where *c* represents the number of coils used and *s* is the number of superimposed pixels at that location. Note that now the maximum value for *p* is nm/R corresponding to a full FOV image sized $n \times m$.

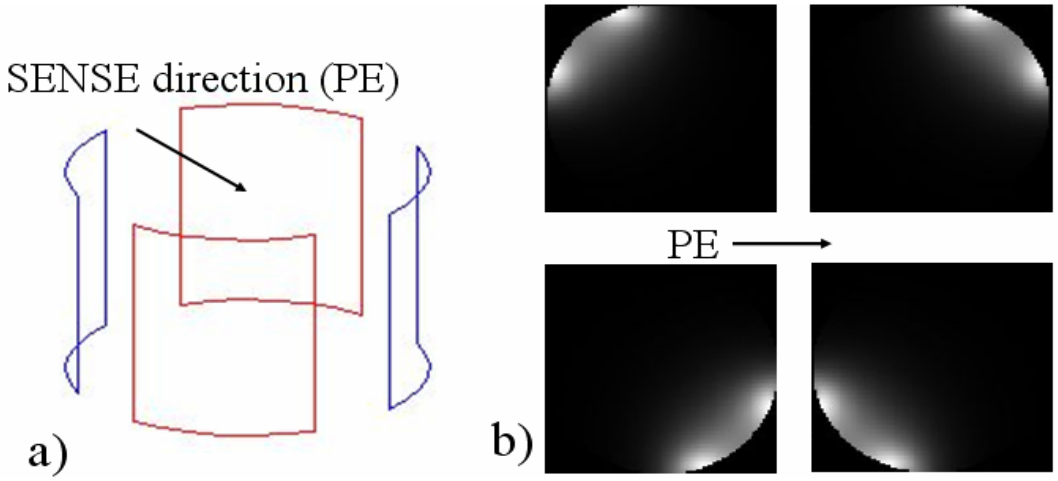

Figure 2.20 – a) Four-element phased array configuration with b) associated sensitivity maps from quasi-static simulations that are optimally oriented for the specified PE direction for use with SENSE.

The aliased signal value is a superposition from the folded pixels, creating a system of linear equations. Folded pixels with zero sensitivity, such as pixels found outside the object space for example, can be ignored, which reduces problem uncertainty. The unfolding matrix U_p, which is calculated for each folded pixel is given by [49]

$$U_p = (S_p^{T*}\Psi^{-1}S_p)^{-1}S_p^{T*}\Psi^{-1} \tag{2.80}$$

where Ψ represents the $c \times c$ receiver noise correlation matrix from equation (2.71). The transpose complex conjugate of the sensitivity matrix S_p must be computed for unfolding. After creating vector $\vec{p}_p$ from the associated image values from each receiver coil for the pixel *p*, signal separation is calculated from

$$\vec{P}_p = U_p \vec{p}_p \tag{2.81}$$

and the separated pixel values are given in resulting vector $\vec{P}_p$ for the unfolded image. This procedure must be repeated for each pixel in the reduced FOV to obtain the full, unfolded image. The matrix inversion of equation (2.80) is only possible if $c > s$, meaning that the reduction factor is less than the number of receiver coils. Perfect image reconstruction is generally not possible because the sample values will be noisy relative to the sensitivity data.

Unlike standard Fourier images, the noise levels in SENSE images vary from pixel to pixel because the receiver noise matrix Ψ is not unitary, resulting in correlated noise between pixels [49]. As the number of PE steps is reduced in SENSE imaging, reconstructed image SNR is reduced, indicative of the negative effects of increasing R. Specific to Cartesian sampling, a geometry factor (g-factor) is defined, describing the increased noise caused by using the nonunitary matrix. This g-factor is calculated on a pixel by pixel basis as

$$g_p = \sqrt{[(S_p^T \Psi^{-1} S_p)^{-1}](S_p^T \Psi^{-1} S_p)} \geq 1 \tag{2.82}$$

Coils can be designed to optimize g-factor maps for certain regions, such as cardiac, breast or brain imaging, where a g-factor of one corresponds to no additional noise from unfolding the data.

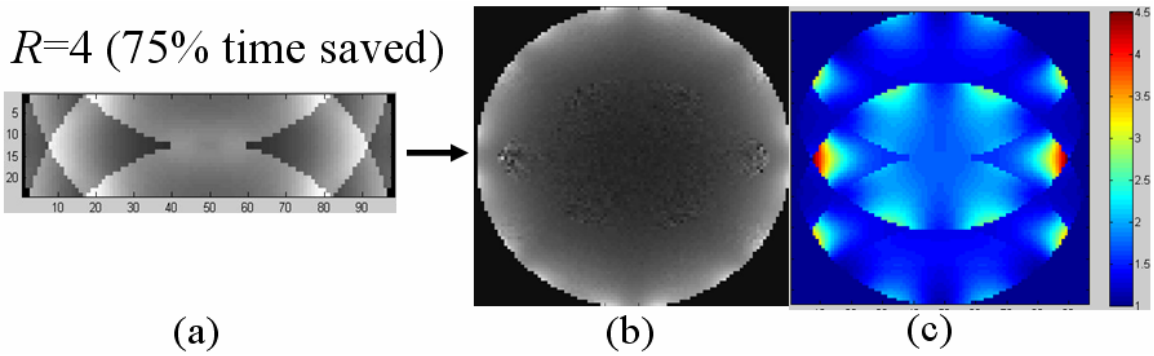

Figure 2.21 – By applying L-R PE with acceleration $R = 4$ on an axial profile from an eight element coil configuration, one can reconstruct the (a) aliased image, (b) noisy reconstructed image, and (c) associated g-factor map.

A sample *g*-factor map is given in Figure 2.21c for an eight coil configuration and $R = 4$. Also, the aliased and reconstructed images are shown, demonstrating how the noisy regions of Figure 2.21b) are visibly related to the *g*-factor map. The SNR in the resultant, reconstructed image can be calculated as

$$SNR_p^{red} = \frac{SNR_p^{full}}{g_p \sqrt{R}} \tag{2.83}$$

for each pixel *p*, where SNR_p^{full} represents the SNR from the full FOV image (calculated using equation (2.79)), and SNR_p^{red} represents the reduced SNR, based on the reduction factor *R*. Notice that even with a perfect *g*-factor, having a value of one everywhere, there is an upper bound SNR according to $\sqrt{R}$ because less total data is collected. This dictates ideal coil design performance. Even with an infinite number of surface coils, a perfect *g*-factor map is still unattainable due to inherent limitations of parallel MRI. The electrodynamic signal detection process has been analyzed for optimal attainable performance, where researchers have coined the associated term of ultimate intrinsic SNR [45][75]. For the general theory of SENSE, including derivation of why the *g*-factor describes the added noise, refer to [49].

The SENSE parallel imaging technique operates purely in the image domain after receiving the aliased image. To utilize parallel imaging in the time domain, SiMultaneous Acquisition of Spatial Harmonics (SMASH) can be used [59]. For an alternate approach, based on the SMASH technique, one can employ GeneRalized Auto calibrating Partially Parallel Acquisition (GRAPPA) [18]. The mathematical theory governing these methods was not explored for this thesis because an equivalent calculation to the *g*-factor does not exist for design evaluation.

To properly design a receive coil array for parallel imaging, the $\vec{B}_1^-$ map must be determined. The $\vec{B}_1^+$ field must be calculated for transmit coil design. Both fields can be easily solved in a computational environment or a physically realized one using B_1

mapping techniques (see Appendix A for explanation). Full $\vec{E}$ field and $\vec{B}$ field knowledge enables complete analysis of coil performance.

2.5 Application to MRI Coil Design

2.5.1 Introduction

This section compares different methods for acquiring 3D $\vec{E}$ and $\vec{B}$ fields computationally. As all approaches make a series of approximations and assumptions, the designer must be aware of how accurate the computation is, and ensure that a physical realization of the design will satisfy project goals. This requires computational tests with experimental verification.

2.5.2 Field Modeling Approaches

A number of computational algorithms exist that are designed to mathematically calculate how a system of charges affects electric and magnetic fields within a confined volume. Under the assumption of a system without time-varying currents, Coulomb's Law and the Biot-Savart Law can be used for $\vec{E}$ and $\vec{B}$ field calculations as

$$\vec{E}(r) = \frac{\int_C \rho_l dl}{4\pi\varepsilon_0\varepsilon_r r^2}\hat{r} \tag{2.84}$$

$$\vec{B}(r) = \frac{\mu_0\mu_r \vec{I}}{4\pi}\int_C \frac{d\vec{l}\times\hat{r}}{|\vec{r}|^3} \tag{2.85}$$

where ρ_l is the charge density for infinitesimal length dl, $\varepsilon_0\varepsilon_r$ is the material permittivity, $\vec{r} = |\vec{r}|\hat{r}$ is the distance vector from the charge or current point to the field point, $\mu_0\mu_r$ is the material permeability, and $\vec{I}$ is the current flowing through the space. MRI applications apply to time-varying signals at the system Larmor frequency, where the wavelength λ is given by

$$\lambda = \frac{2\pi c}{\sqrt{\mu_r \varepsilon_r}\,\omega_0} \tag{2.86}$$

using speed of light ($c = 2.998\times10^8$ [m/s]) and signal frequency ω_0. At smaller main $\vec{B}_0$ fields, the signal wavelength is typically much larger than any sample dimension, describing situations where quasi-static calculations will produce accurate field behaviour patterns [28]. For human MRI, industry standard generally permits quasi-static calculations as acceptable for $\vec{B}_0 \le 1.5\,\text{T}$ ($\sim \lambda/4$ sample). Otherwise, field behaviours are not accurate based on human body dimensions and tissue permittivity constants. For such systems, including the 3T system this thesis utilizes, full-wave field solutions should be computed, as the $\vec{E}$ field can no longer be approximated as conservative ($\nabla \times \vec{E} \neq 0$).

The three most common full-wave computational approaches include FDTD, Finite Element Method (FEM) and the Method of Moments (MoM). Since a finite number of calculation points must be chosen, all computational techniques are inherently approximations because the solution space must be discretized.

The MoM approach requires the calculation of Green's functions, making it best suited to systems with linear homogeneous media, such as free space. The Green's functions, or fundamental solutions, can be problematic to integrate, as they are based on a solution of the system of equations subject to a point source or charge [47]. From an MRI perspective, MoM works well for unloaded coils, being free space calculations, but is inefficient for non-homogeneous media such as a human body model [28].

The FEM approach works well for complex geometries and inhomogeneous media. Each element, having an arbitrary orientation and number of sides, is described by its nodes and one edge point, where an interpolation function is formed between nodes. This forms a matrix inversion problem to solve for the finite number of unknown coefficients, in turn allowing calculation of the nodal values. The MRI research community has found FEM works well for samples with small contrast, but can lose computational efficiency for modeling neighbouring tissues having large contrast [28].

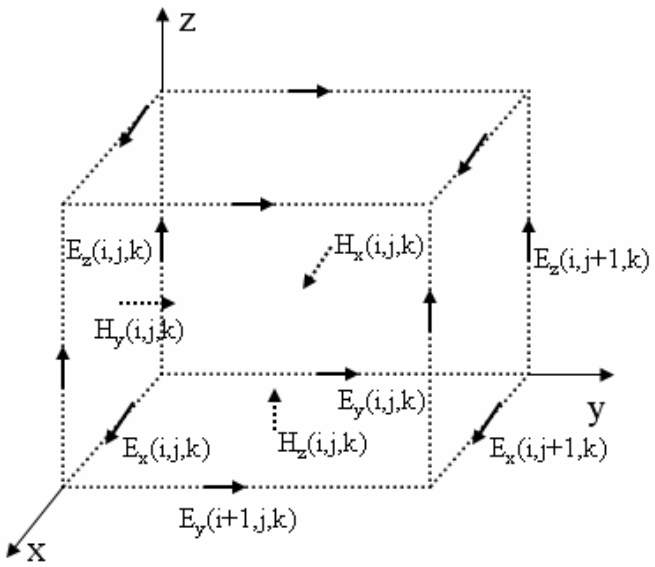

Figure 2.22 – Yee cell geometry for use in FDTD calculations of Maxwell's Equations.

The FDTD method requires defining a mesh and relating nodal field values to their neighbouring fields based on Maxwell's equations, boundary conditions and general continuity relations. One advantage of the explicit FDTD method over the MoM and FEM methods is that it does not require large scale matrix inversion [28]. By dividing the sample space into Cartesian Yee cells [64][77] as shown in Figure 2.22, FDTD iterates through time steps allowing signals and fields to propagate through the defined sample space [37]. The propagations follow Maxwell's curl equations, given for an isotropic medium as

$$\nabla \times \vec{E} = -\mu_0 \mu_r \frac{\partial \vec{H}}{\partial t} \tag{2.87}$$

$$\nabla \times \vec{H} = \sigma \vec{E} + \varepsilon_0 \varepsilon_r \frac{\partial \vec{E}}{\partial t} \tag{2.88}$$

These curl equations are used to assign $\vec{E}$ and $\vec{H}$ component variables to three edges and three faces for the cube of Figure 2.22, and then repeated to generate a meshed grid of coordinates. Using incremental time step Δt, which relates to the iterated time index *n*, the space and time derivatives using a central finite difference approximation are given as

$$\frac{\partial F^n(i,j,k)}{\partial x} = \frac{F^n(i+1/2,j,k) - F^n(i-1/2,j,k)}{\Delta x} \tag{2.89}$$

$$\frac{\partial F^n(i,j,k)}{\partial t} = \frac{F^{n+1/2}(i,j,k) - F^{n-1/2}(i,j,k)}{\Delta t} \tag{2.90}$$

The half time step indicates that the fields are alternately calculated, achieving central differences for the time derivatives [4]. These equations are used on each of the six scalar equations represented by Maxwell's curl equations to yield six coupled explicit finite difference equations.

FDTD is used most commonly for MRI calculations for its predictable computational requirements and conceptually simplistic backbone [28]. For design guidelines, the respective frequency and time step limitations of FDTD are

$$\max(\Delta x, \Delta y, \Delta z) < \frac{\lambda_{\min}}{20} \tag{2.91}$$

$$\Delta t < \frac{\sqrt{\varepsilon_r \mu_r}}{c} \frac{1}{\sqrt{\frac{1}{\Delta x^2} + \frac{1}{\Delta y^2} + \frac{1}{\Delta z^2}}} \tag{2.92}$$

where $(\Delta x, \Delta y, \Delta z)$ represents the cell edge sizes in their respective dimensions. The smallest allowed wavelength, $\lambda_{\min}$, corresponds to the maximum frequency the given mesh can solve for. The time step Δt is restricted to ensure solution stability. The most common commercially available FDTD software used by MRI researchers is XFDTD by Remcom Inc. All full-wave calculations presented in this thesis were obtained using XFDTDv6.3.

Boundaries are essential for reducing the problem space from being infinite to something computationally reasonable. The primary requirement for the boundary is to alter the fields less than a pre-determined threshold, relative to the solution obtained using an infinite boundary. Successively extending or contracting the boundary can establish the threshold point where the inner fields are accurate, while still ensuring the computation time to be minimal.

Boundary types can be grouped into absorbing and reflecting. Two common absorbing boundary types are Perfectly Matched Layer (PML) and Liao, where the most common reflecting boundary is a Perfect Electrical Conductor (PEC). Although the superconducting magnet is treated as PEC material for MRI, its distance from the RF sources is large enough to allow for absorbing boundaries to be used, placed in close proximity to the RF coils. The fields within the sample are of primary concern, being those on the side of the RF coils that is in the opposite direction as the superconducting magnet.

2.5.3 Use of SNR in RF Array Coil Design

In general, design of RF coil arrays can be accurately carried out in a computational environment provided that the limiting assumptions are known and SNR comparisons are made from a relative improvement basis, opposed to an absolute one. Typical optimization parameters include maximizing SNR performance for a specified region, or minimizing the required imaging time by applying parallel imaging. A wide range of array coil designs exist, where each design is specific to magnetic field strength $\vec{B}_0$, number of available channels, and the designed region, which could be brain, spine, cardiac or shoulder for example. The primary comparison parameters between array designs include:

1) Calculated SNR after parallel reconstruction using equations (2.59) and (2.79).
2) Parallel imaging performance, as measured by *g*-factor maps, at predetermined reduction factors using equations (2.82) and (2.83).

The four equations of concern are repeated below for convenience.

$$SNR \overset{\Delta}{=} \frac{|V_s|}{V_n} = \frac{2\omega M_z^0 \left| \sin\left(\gamma\tau \vec{B}_1^+\right) \vec{B}_1^{-*} \right|}{\sqrt{4kT\Delta f P_{abs}}} \tag{2.93}$$

$$SNR_p^{OPT} = \sqrt{\vec{p}_p^T \Psi^{-1} \vec{S}_p^*} \tag{2.94}$$

$$g_p = \sqrt{[(S_p^T \Psi^{-1} S_p)^{-1}](S_p^T \Psi^{-1} S_p)} \geq 1 \tag{2.95}$$

$$SNR_p^{red} = \frac{SNR_p^{full}}{g_p \sqrt{R}} \tag{2.96}$$

For controlled comparisons, all system parameters should be held constant. This includes the sample, the applied RF pulse and the MRI system architecture; meaning $\vec{B}_0$ field, number of channels, system noise figure and magnet bore geometry. Related to equation (2.93) the following variables become constant: ω, M_z^0, γ, τ, T, and Δf. Thus, for a given 2D slice, only a complex $\vec{B}_1$ profile (for signal calculations) and the 3D $\vec{E}$ field values (to calculate absorbed power) are required. The sensitivity matrix S_p and sensitivity map vector $\vec{S}_p$ are formed from the $\vec{B}_1^-$ of each RF coil based on the chosen reduction factor *R* for reduced pixel *p*.

From a computational perspective, it is important to stress that a full 3D $\vec{E}$ field and conductivity map of the sample is required for every coil element to produce Ψ, which can demand substantial computer storage space and calculation time as the number of elements is increased. Also, image resolution must be considered, as both equations (2.94) and (2.95) must be calculated by looping through every pixel in the reduced image.

For perspective, computation of steady state fields for each element for this research requires 430MB of storage and takes two hours using a P4 2.8GHz Duo Core personal computer. This corresponds to 7GB of storage and 32 hours of computation time for a single 16-channel design to be evaluated. This restricts the feasibility of automated optimization approaches such as simulated annealing, genetic algorithms, or other search techniques; as such none were applied to this research.

CHAPTER 3 Anterior Cardiac Array Coil Design

3.1 Introduction

Software environments have become popular for testing the viability of potential MRI RF coil designs due to the costs associated with fabrication and experimental tests. As discussed previously, for accurate prediction using high field systems (>1.5T) with large samples, such as human subjects, a full-wave modeling program must be employed [28]. For MRI based analyses of resultant electromagnetic fields, a substantial amount of post-processing is required, particularly for array coils and parallel imaging.

In this chapter, field patterns from the commercially available XFDTDv6.3 software are verified, and then analyzed using a post-processing MRI analysis program that was developed as part of this research. The 16-channel anterior cardiac array was designed and is analyzed in this computational environment. This involved comparing to other 16-channel anterior arrays to verify the project hypothesis, as well as comparing to a six-channel OEM cardiac array to ensure that the project specifications are satisfied. Finally, electrical considerations are discussed for transitioning from the simulation environment to realizing the design.

3.2 Verification of XFDTD Software

3.2.1 XFDTD Capabilities and Output Fields

Full-wave field calculations, for designing MRI coils, were performed using the Remcom Inc. software XFDTDv6.3. Some of the features and capabilities of this software will now be described.

The XFDTD modeling software is capable of storing 2D Cartesian planes for complex $\vec{B}$ and $\vec{E}$ fields, conduction currents $\vec{J}$, SAR and surface currents. System excitation can be accomplished by placing discrete sources within the mesh, forcing an

incident plane wave on the system, or applying a Gaussian beam, all either as broadband or single frequency excitations to obtain steady state behaviour.

Output data is stored as Cartesian planes, based on requests from the user, where either a steady state fields, or time-step based fields can be selected. Each requested plane is stored in a text file as magnitude and phase components for the associated cell edges in that plane. Memory constraints become important when storing $\vec{E}$, $\vec{B}$, and $\vec{J}$ fields over a 3D region, particularly when considering an array of coils. Hard disk storage requirements are 1MB for a 120×84 cell $\vec{E}$ or $\vec{B}$ field plane. If both the coil design and the sample space have radial or axial symmetries, the problem space can be reduced by assuming an infinitely long cylindrical sample, or adapting symmetry, which simplifies the computational requirements. For the 16-channel designs considered in this thesis, approximately 7GB of storage was required per design.

3.2.2 Boundary Conditions for XFDTD

The optimal boundary condition is the one requiring the shortest computation time while satisfying chosen accuracy criteria. The accuracy criterion applied for this research requires computing a resonant frequency between successive iterations to within 100 kHz of the last iteration. The boundary condition was increased by three cells per dimension for each iteration. The resolution within the sample was held constant for all test cases, meaning increased mesh sizes are only beneficial if the respective field values become substantially more accurate.

For determining appropriate absorbing boundary conditions, a 9 cm square loop made of infinitely thin copper ($\sigma = 5.8E7$ S/m) wires, having four equally spaced lumped element capacitors (26.9pF) was simulated in free space using various Liao and PML absorbing boundaries with 6 layers on a 5 mm fixed cell size Cartesian mesh. A 32-time step length Gaussian pulse was applied across one capacitor, and then transient field calculations were performed for 35000 time steps, with each time step being 9.629 ps. The steady state data was used to analyze resonant properties of the circuit. The

computations started with a tightly placed boundary for both the Liao and the PML case, and then the boundary was successively increased. For each setting, the required computation time and resultant resonant frequency were measured, where the results are shown in Table 3.1. The number of free space boundary cells that were placed around every side of the square loop structure is shown in the first column.

Table 3.1 – Comparison of PML to Liao boundary conditions for XFDTD calculations.

Bondary Condition	Computation Time	Resonant Frequency	Total Mesh Size (cells)
6 layer PML (5 cell)	1:00	134.4 MHz	28x10x28 = 7840
6 layer PML (7 cell)	3:15	122.9 MHz	32x14x32 = 14336
6 layer PML (9 cell)	4:21	123.1 MHz	36x18x36 = 23328
6 layer PML (12 cell)	**6:34**	**123.2 MHz**	**42x24x42 = 42336**
6 layer PML (15 cell)	10:08	123.2 MHz	48x30x48 = 69120
6 layer PML (18 cell)	14:07	123.2 MHz	54x36x54 = 104976
Liao 10 cell	1:23	126.0 MHz	38x20x38 = 28880
Liao 13 cell	2:03	124.6 MHz	44x26x44 = 50336
Liao 15 cell	2:51	124.0 MHz	48x30x48 = 69120
Liao 18 cell	4:19	123.6 MHz	54x36x54 = 104976
Liao 21 cell	6:08	123.4 MHz	60x42x60 = 151200
Liao 24 cell	8:08	123.3 MHz	66x48x66 = 209088
Liao 27 cell	10:26	123.2 MHz	72x54x72 = 279936

It was found that using a PML boundary with 6 layers requires at least 12 border cells around the computation space for the solution to change resonant frequency by less than 100 kHz from the previous iteration. The Liao boundary requires at least 27 border cells for each dimension before this criterion is met. The boundary condition meeting the outlined criterion and requiring the shortest computation time is the 6 layer PML boundary, with 12 border cells.

The fields from a loop along its centerline are proportional to its diameter, implying that the number of required boundary cells should be determined based on distance ratio relative to the diameter of the excited loop. Because the above calculations used a 5 mm mesh, the acceptable boundary requires 6 cm of free space for a 9 cm loop.

This implies a required border of 6/9 = 2/3 the diameter of the RF loop being calculated should be used. Using a larger 6 layer PML boundary simply corresponds to increased computation time, with similar accuracy in the resulting field behaviour.

3.2.3 XFDTD Output Field Verification

A 8.5 cm square saddle coil was constructed and simulated for use in a 7T MRI system, having a resonant frequency of 309 MHz. A 15.4 cm diameter, 26 cm length cylindrical saline phantom was used when collecting the experimental images. The phantom has electrical parameters $\sigma = 0.48$ S/m and $\varepsilon_r = 76.7$, based on solution concentrations of $CuSO_4$ = 1 g/l and NaCl = 2.5 g/l. A GE pulse sequence was used with $T_R = 3$ sec and $T_E = 10$ msec, which makes ignoring relaxation effects a reasonable assumption for the simulations. The single loop was used as both a transmit and receive coil, meaning the full-wave SNR calculations were based on

$$SNR \propto \frac{\sin(\gamma\tau\vec{B}_1^{+})\vec{B}_1^{-*}}{\sqrt{P_{abs}}} \tag{3.1}$$

after simplifying equation (2.59) by removing constants. When using quasi-static calculated fields, $\sin(\gamma\tau\vec{B}_1^{+})\vec{B}_1^{-*}$ is replaced with $\sin(\gamma\tau\,|\,\vec{B}_1\,|)\,|\,\vec{B}_1\,|$ because phase information is different for frequency dependant calculations.

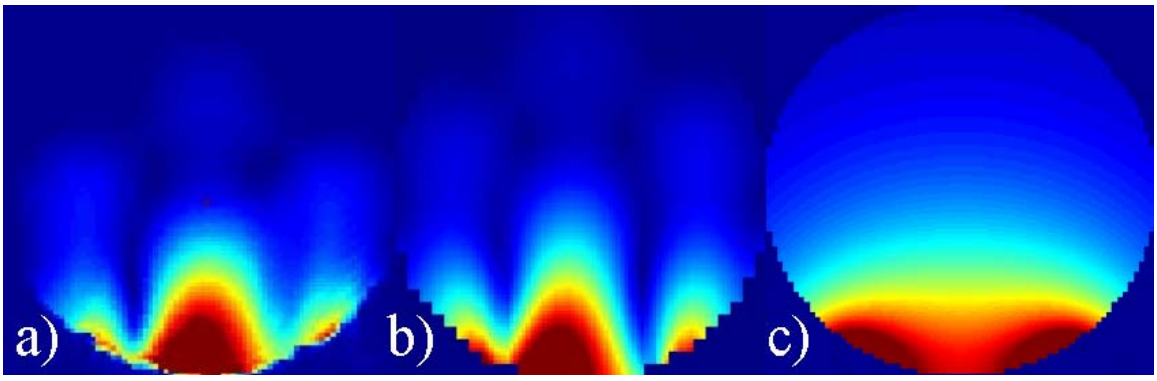

Figure 3.1 – Image SNR maps from single saddle coil with a 7T MRI system from a) experimental measurement, b) XFDTD full-wave calculation, and c) quasi-static simulation.

Three different image maps are shown in Figure 3.1, being the experimentally obtained SNR, XFDTD calculated SNR, and quasi-static calculated SNR profiles,

respectively. Qualitatively, the XFDTD field output patterns matched those found in experiment. The quasi-static predicted SNR map shows very bad agreement with the experimentally obtained one, making it clear that quasi-static computations are inadequate for modeling a 7T system. The XFDTD predicted SNR exhibits good agreement to Figure 3.1a, proving XFDTD is capable of accurately modeling high field MRI system behaviour.

For verification of XFDTD when applying parallel imaging techniques, comparisons of *g*-factor maps were performed using quasi-static and XFDTD field outputs for a 1.5T system. These results were compared to those from a research paper accepted by the MRI community, authored by de Zwart et al [12]. The accepted results were obtained from a quasi-static program on a uniform cylindrical phantom.

To approximate quasi-static field behaviour, the coils were designed at 64 MHz for XFDTD computation. The simulations used eight identically shaped coil elements around a cylinder having both length and diameter equal to 20 cm. Each saddle coil was 15.4 cm long, with an arc angle of 30° and a radius equal to 11 cm. XFDTD calculations required defining the sample permittivity, which was set to $\varepsilon_r = 76.8$, to emulate a typical saline solution.

Different *g*-factor maps for the different computation environments are given in Figure 3.2. The primary difference between the de Zwart and Quasi-static columns relates to different contrast enhancement applied, as a different number of grayscale levels were used. Good agreement was found for the quasi-static simulation, verifying the *g*-factor calculation algorithm developed for this thesis.

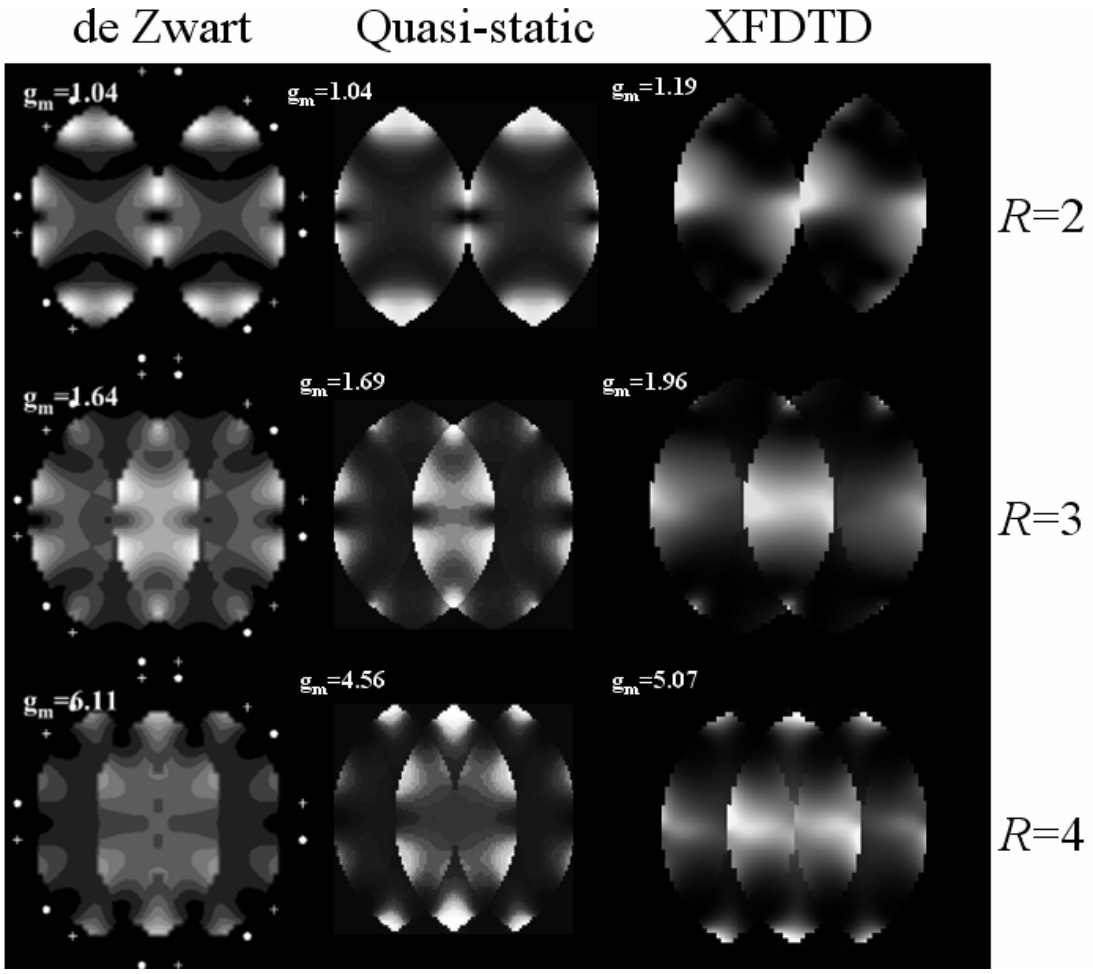

Figure 3.2 – Comparison of *g*-factor maps for different reduction factors, *R*, for an eight-channel saddle coil around a uniform sample. The left column shows results from a trusted quasi-static research paper by de Zwart (source: [12], ©2002). Comparisons are made to both quasi-static and XFDTD outputs generated for this thesis.

The same algorithm was used for analyzing the XFDTD output fields, showing poor agreement with the de Zwart *g*-factor maps. It was determined that *g*-factor maps are much more susceptible to inaccuracies in sensitivity maps than SNR profiles are. As the XFDTD sensitivity maps are considered more accurate than the quasi-static ones, it is believed that the de Zwart results do not represent a clinical situation as well as the XFDTD obtained results do. More investigation is required into this issue, but was considered to be outside the scope of this research.

To verify that the SNR profiles between the XFDTD and the quasi-static case are in relatively good agreement, they are both shown in Figure 3.3. Good agreement was

found for simulated SNR maps relating to a 1.5T system. Recall that substantially different SNR maps resulted for a 7T system, demonstrated by Figure 3.1.

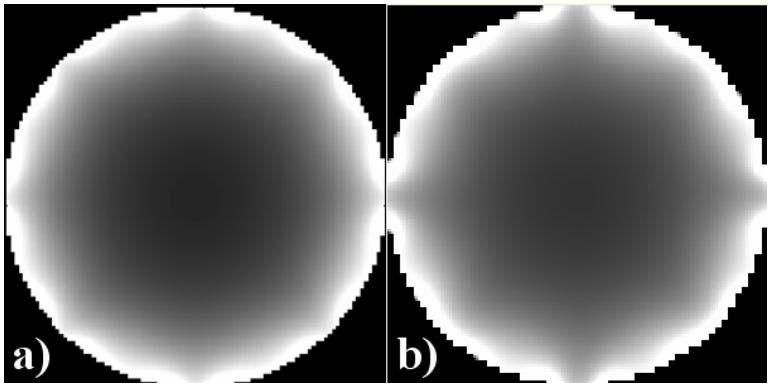

Figure 3.3 – Composite SNR profiles for an eight element array applying Roemer optimal reconstruction with a) quasi-static field profile, and b) XFDTD fields for a 1.5T system.

3.3 Performance Analysis Software

3.3.1 XFDTD Human Torso Model

A 5 mm mesh of a human male was supplied with the XFDTDv6.3 Bio-Pro software, which is ideal for calculations of SAR. However, this mesh is insufficient for parallel imaging analysis because of the air gaps found within it, which are present to model the lungs. These air gaps correspond to signal nulls in MRI, which are shown in Figure 3.4. Air gap locations play a significant role in *g*-factor calculation because the number of superimposed pixels can be artificially reduced. Designs based on this model could indicate an artificially improved *g*-factor map because of the air gaps, which are not constant from patient to patient, in addition to having position and size variations.

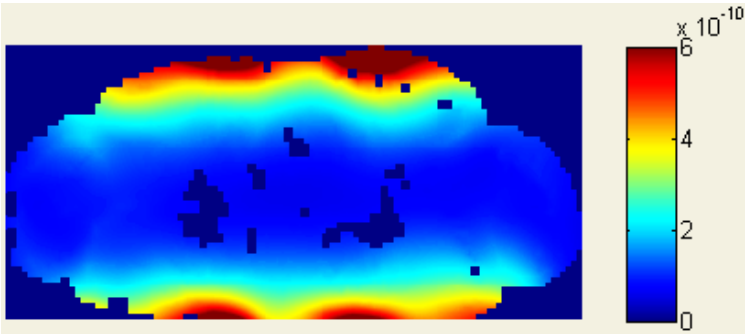

Figure 3.4 – Sample axial SNR calculation from XFDTD for 5 mm mesh of a human male demonstrating air gaps as signal nulls within the chest.

Furthermore, as the design is region specific, it is also undesired for performance to be dependant on changes in permittivity within the sample. Thus, a simplified human torso model having little structure was used in this thesis. This human torso model was developed based on data collected from a range of sources [17][20][43][63][73][80], as well as test scan measurements performed at the NRC, and it will now be described.

The average male torso model is chosen to have outermost dimensions of 40 cm$\times$26 cm$\times$64 cm for width, depth and length, respectively. The side boundaries are formed using an ellipse with a 40 cm major axis and a minor axis of 32.4 cm, where the top and bottom edges were removed to form equal flat surfaces 26 cm apart. Based on this chopped ellipse, a 1.5 cm layer of epidermis, or adipose tissue, having electrical parameters $\sigma = 0.07S/m, \varepsilon_r = 5.1$, is placed on the periphery. The interior is made of uniform tissue having electrical parameters $\sigma = 0.6075S/m$, $\varepsilon_r = 32.4$.

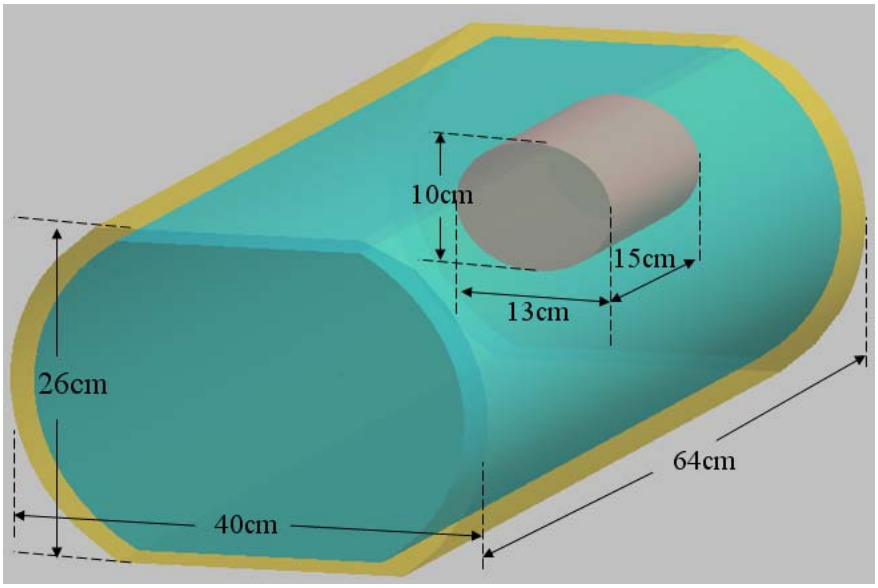

Figure 3.5 – Human torso model for XFDTD with cardiac region. The three different tissues used were epidermis or adipose (yellow), inner tissue (aqua) and myocardium (pink).

The cardiac region was modeled as an elliptical cylinder with dimensions 13 cm$\times$10 cm $\times$ 15 cm for width, depth and length, respectively. The cardiac region was centered at (4.5 cm, 5.4 cm, -15.5 cm) relative to the torso center, and given parameters $\sigma = 1S/m, \varepsilon_r = 52.6$. Figure 3.5 depicts the final torso used for this project,

where different tissues are given different colours. The electrical parameters were determined from a weighted sum of different tissue types found within the human torso.

3.3.2 Analysis Software for Parallel Imaging Array Coil Design

To perform MRI specific computations on the complex fields obtained from XFDTD, a post-processing program was developed for this project. The MatlabV7.1 programming environment was selected because of its efficient matrix calculations, straightforward GUI management tools, and because it is commonly used by the potential users at the NRC-IBD.

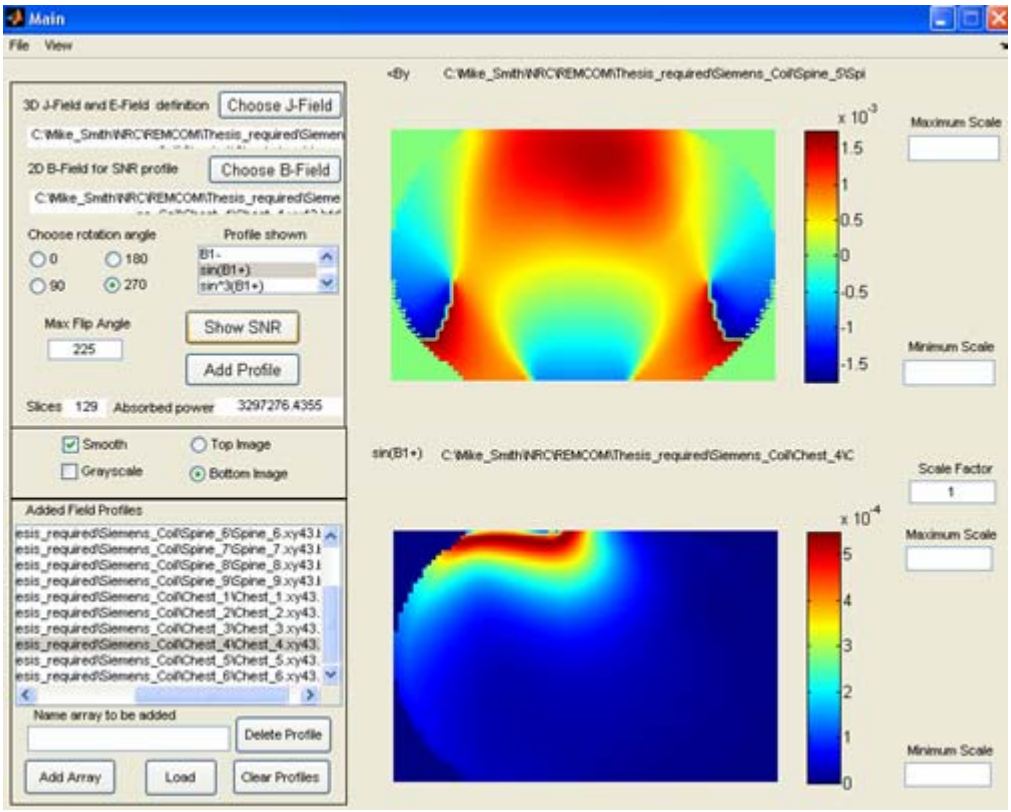

Figure 3.6 – Single coil analysis GUI for XFDTD outputs.

The software's GUI was given two main views, the first geared towards single element analysis, as shown in Figure 3.6, and the second aimed at array coil design. The single element view, shown in Figure 3.6, allows one to define a set of coil elements by specifying associated $\vec{J}$ and $\vec{B}$ field file names and paths. The useful design approach of employing radial symmetry is enabled using rotation operators, and translation through

the axial dimension is established by altering the starting position of the coil. An extensive list of potential $\vec{B}$ field views is available, including transmit field for GE and SE sequences, receive field, component magnitudes and phases, and transmit-receive behaviour with a specified maximum flip angle. The list of added individual coil elements and associated data can be saved, allowing time saving benefits when loading multiple coil designs from their individual elements.

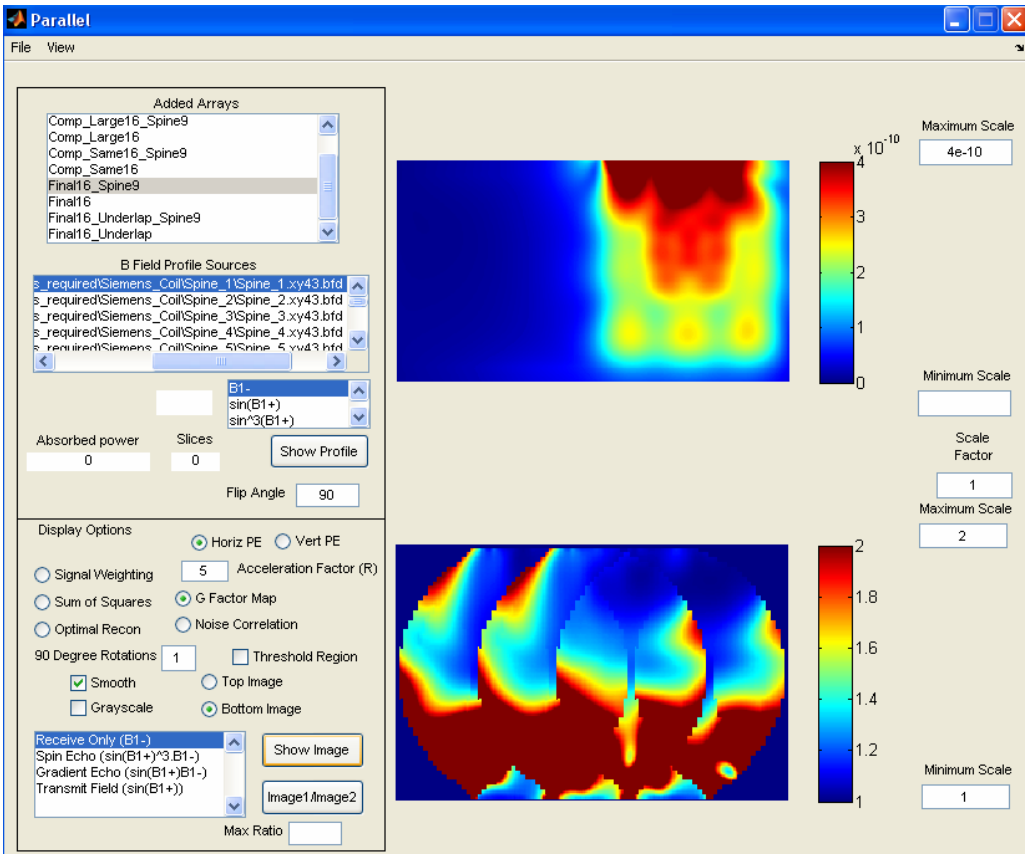

Figure 3.7 – Array coil analysis GUI for XFDTD outputs.

The second view, shown in Figure 3.7, depicts the analysis tools for groups of coils. Any number of array designs or elements per array can be analyzed at once. Composite images from user-defined coil arrays can be calculated and individual coil behaviour can be viewed. Multiple image reconstruction techniques are available to be used, including signal weighted, SoS, and Roemer optimal reconstruction, which may require *g*-factor map calculation. The user-defined array coils can be analyzed as receive only, as a transmit and receive array, through either SE or GE sequences, or as a transmit

only array. The $\vec{B}$ field slice under consideration can easily be changed, and settings can be saved to preserve noise correlation calculations, which can take hours per array, even on a state-of-the-art personal computer (3.2GHz Pentium 4 duo-core). The PE direction can be changed for *g*-factor map calculations, which are available at integer reduction factors. Furthermore, a region can be thresholded based on material conductivity borders to make clear a desired ROI. This is of particular interest for cardiac analysis, where the myocardium, or heart tissue, is given different electrical parameters than the surrounding tissue. A ratio between images can be used to establish relative design improvements.

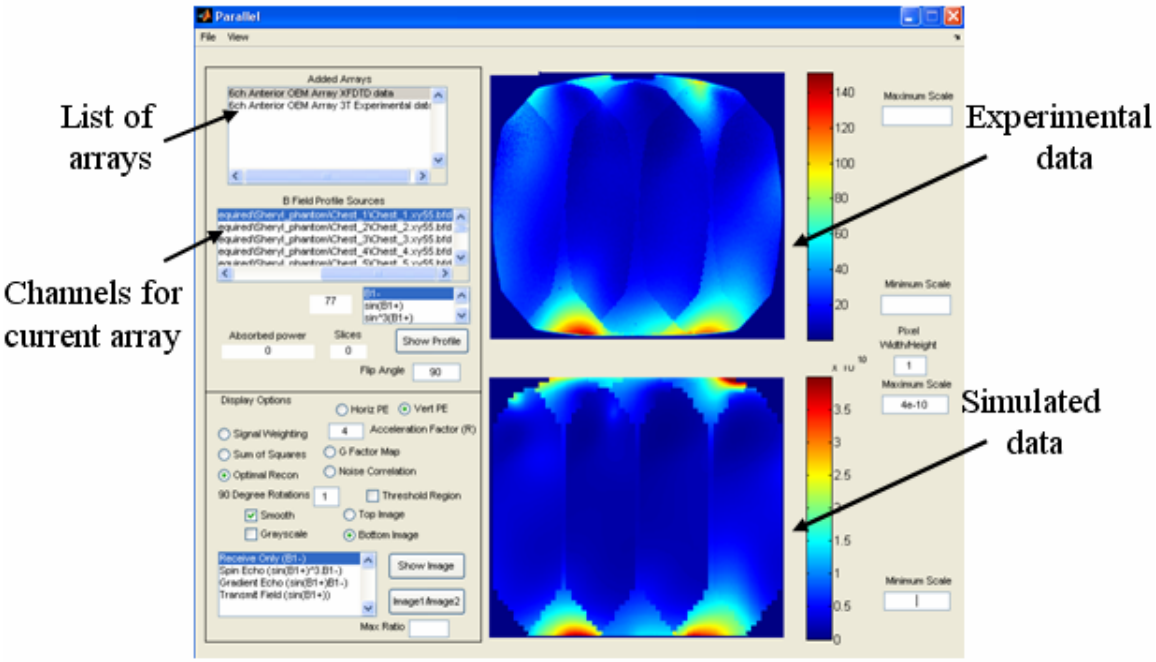

Figure 3.8 – The software analysis program enables post-processing comparisons between experimental (top) and simulated XFDTD (bottom) composite SNR data.

The data input stream can be either from a simulated environment, such as XFDTD, or experimental output data, such as from the 3T Siemens Trio Tim system. This enables immediate assessment of modeling accuracy or qualitative profile comparisons. For an SNR comparison between simulated and experimental results based on the six-channel Siemens array with the nine-channel OEM spine coil, refer to Figure 3.8. The composite images displayed depict axial SNR performance with L-R PE and reduction factor $R = 4$. The experimental data was treated similar to the computed data for post-processing image reconstruction, in that the full FOV data was acquired and used

to emulate reduced FOV images according to equation (2.96). The software back-end was designed to allow extension to other data input types with minimal effort. The user-friendly program allows convenient and quick analysis and data management for a complex structure of text file formats that are output by the XFDTDv6.3 software and the 3T Siemens Trio Tim system. This software was used for the array coil designs that will now be described.

3.4 Array Coil Design

3.4.1 Design Guidelines

All of the experimental work described herein was performed on a 32-channel 3T Siemens Trio Tim system located at the NRC-IBD, which was installed in April of 2006. The system is equipped with a 24-element spine array, consisting of eight rows of three elements, of which up to four rows can be used at any given time. Also, a six-channel chest array was supplied, which has two rows of three uniform hexagonal overlapped elements with a center-to-center distance of 13.3 cm, being the same geometry as the spine elements. The specifications include utilizing three rows of existing spine elements in conjunction with the anterior 16-channel chest array. The XFDTD model of the conforming six-channel chest array with three spine element rows placed around the human torso model is shown in Figure 3.9.

For this design project, relative computational comparisons are essential because absolute SNR behaviour is meaningless in the XFDTD modeling environment. To establish a mapping between XFDTD results and realizable SNR for evaluating resolution capabilities, it is essential to computationally evaluate performance of the existing Siemens supplied cardiac array coil.

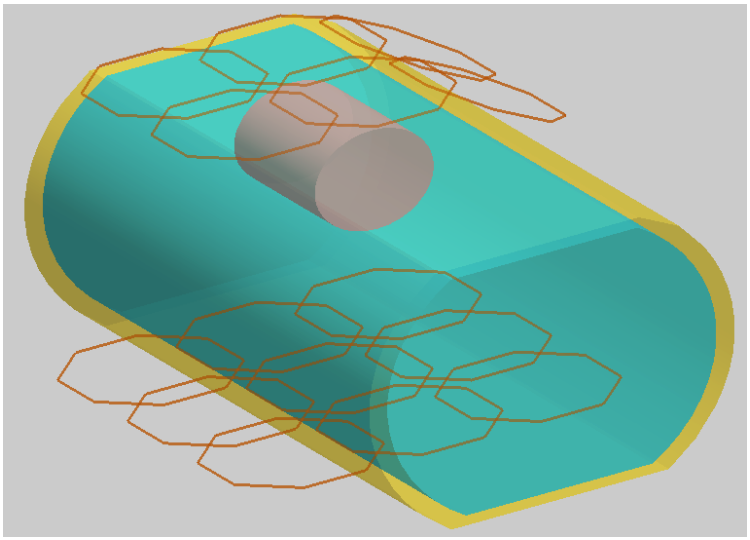

Figure 3.9 – Six element conforming OEM cardiac array with three rows of anterior spine coils. The overlapped hexagonal loops were placed around the XFDTD human torso model.

Increasing the resolution means that the signal per pixel must decrease because the total amount of collected signal data remains constant. The reduced SNR results because the noise level will remain constant, being independent of image resolution, as it is primarily governed by thermal emissions from the sample, described by equation (2.40). To achieve ⅓ mm resolution, while maintaining equivalent SNR to the OEM array, the new design must exhibit three fold SNR gain for the same resolution.

It would be possible to define and model the complete coil array design as an optimization problem, however, without taking into account modeling symmetry assumptions and imposing a pattern on the design solution, the number of variables and the computational requirements of such an optimization problem would be unfeasible. Thus, the design considered here is not claimed to be globally optimal. Instead, a set of design principles and guidelines are used to manually adjust potential designs for improved performance. Some of these guidelines could include overlapping all nearest neighbour coils and choosing dimensions to best suit the coil's SNR coverage requirements.

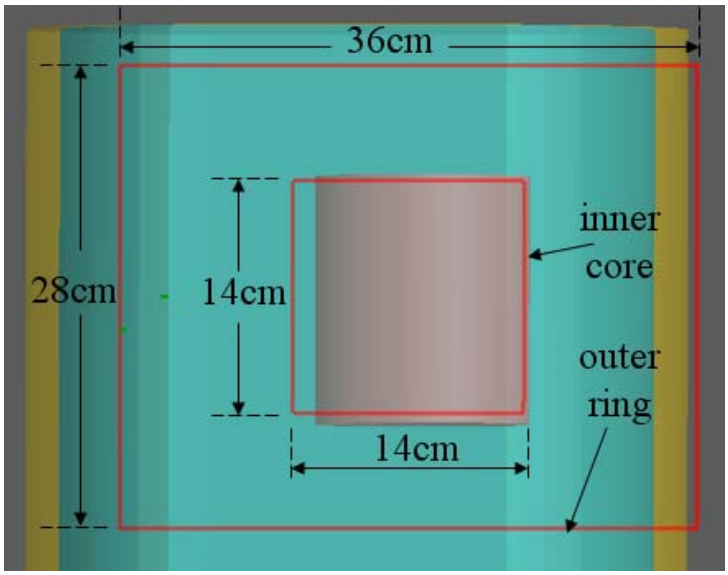

Figure 3.10 – The inner core and outer ring design regions with associated dimensions, placed on the human torso model.

Interfacing between the 16-channel anterior chest array and the Siemens system is accomplished via Siemens supplied connector plugs, which are used to group the design into four, six or eight channels per plug. This made it practical to segment the anterior cardiac design into two separate sections of eight elements early in the design process. The two different sections are named inner core and outer ring, respectively. The main focus of the inner core is to enhance SNR, whereas the outer ring is given the purpose of improving parallel imaging capabilities in the ROI. For perspective, the two sections are labeled in Figure 3.10. Justification for dimension sizes of the two sections will follow.

3.4.2 Inner Core Section

The inner core section is made of eight separate coils that are placed directly above the myocardium region, intended to be very sensitive to the ROI. Based on a maximum region depth of 13 cm from the chest wall and a L-R width of 13 cm, the inner core was chosen to have an outer perimeter of 14 cm by 14 cm, allowing for 1 cm separation between the coil and the patient, ensuring that the SNR is not sacrificed in the posterior section of the cardiac region. As expected, computational analysis of arrays with smaller dimensions than 14 cm by 14 cm showed a reduced average SNR, despite proving advantageous near the surface of the sample.

Element overlap was utilized between all neighbouring inner core loops to reduce the associated inductive coupling. Furthermore, for maximizing the received signal at the depth of the anterior coronary arteries, the inner core elements were designed to have dimensions between 4.5 cm and 6 cm. This provides optimized SNR at depths of 3.5 cm to 5 cm due to the 1 cm separation. Applying this restriction to eight overlapped elements occupying a 14 cm by 14 cm space provides sufficient design constraints for shrinking the problem space into something manageable.

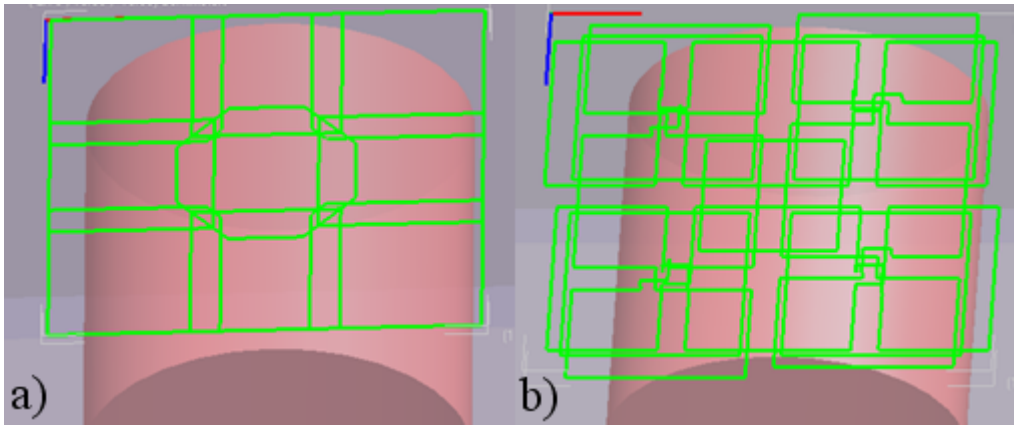

Figure 3.11 – Conductor placements for nine element inner core architectures using a) a regular three by three grid of the overlapped simple loop array and b) five simple loop coils and four naturally decoupled twisted loops stacked on top.

For the initial simulations, both, simple loop coils [54] and naturally inductively decoupled twisted array coils [34] were considered for SNR behaviour, with parallel imaging performance taken as secondary. The simple loop array design was made of a three by three grid of overlapped array coils; each sized 5.25 cm by 5.25 cm. The twisted loop pattern used five simple loop coils, with four twisted loops overlayed on top, and placed so as to be naturally decoupled with the simple loops. The two different arrays are shown in Figure 3.11.

Previous work [34] showed that applying twisted loops to an array, using lots of underlap between simple loop elements, with lots of overlap with the twisted loops, can effectively retain the SNR improvements associated with overlap, while providing the *g*-factor benefits of using underlap. However, by forcing the array onto a 14 cm square surface, the twisted elements become quite large (6.5 cm by 14 cm), meaning that SNR

performance at depths between 3.5 cm and 5 cm are sacrificed. Also note that the conductor placement for the twisted loop design is far more complex than that of the simple coil approach, and this would make fabrication more difficult, particularly with the small design space allocated for the inner core section.

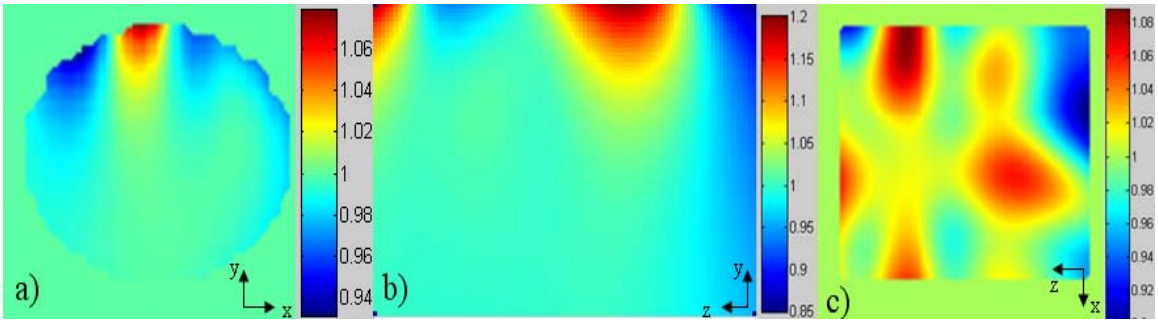

Figure 3.12 – SNR ratios thresholded over the desired cardiac ROI of the simple loop array divided by the naturally decoupled twisted array for cardiac a) central axial slice, b) central sagittal slice and c) 7 cm deep coronal slice.

The simple loop array and twisted array designs were compared to determine what architecture is better for the inner core. The SNR ratios for a central axial, central sagittal and 7 cm deep coronal slice are displayed in Figure 3.12, where the SNR ratios are based on the simple loop array coil design divided by the twisted array design. It is clear that the simple loop array design provides better SNR at shallow depths.

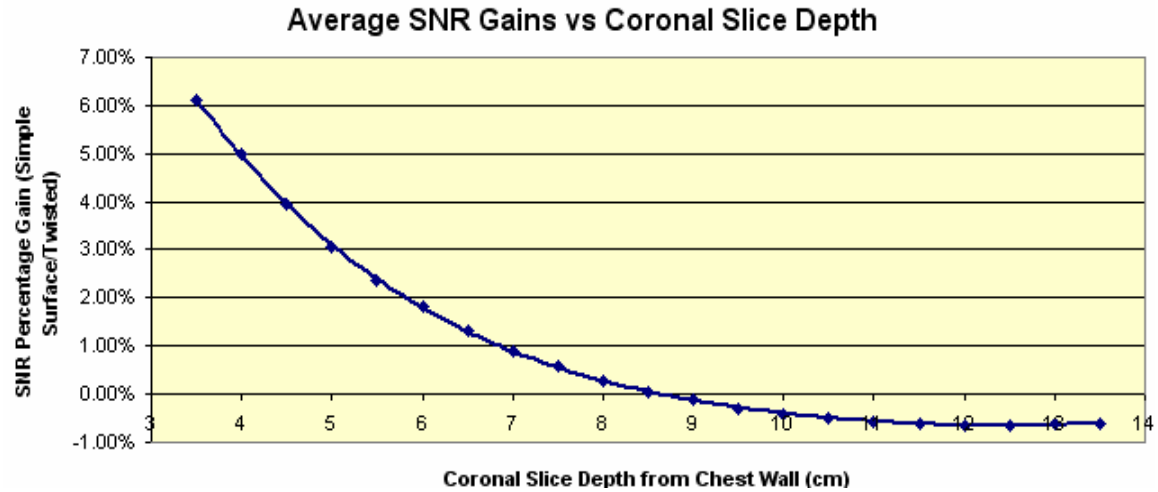

Figure 3.13 - Average SNR gains of a nine-channel simple loop array design relative to a nine-channel twisted array coil as a function of coronal slice depth.

For quantitative evaluation, the SNR was averaged over each coronal slice covering the ROI, with a percentage gain line plot as a function of slice depth relative to

the chest wall displayed in Figure 3.13. Clearly, for the 3.5 cm-5 cm depth of interest for anterior coronary imaging, the simple loop array design provides better SNR relative to the twisted array approach. This behaviour matched expectations based on design geometry.

An interesting finding is that *g*-factor analysis of the inner core alone displayed significant improvements from the twisted array relative to the simple loop coils. A qualitative demonstration of this is shown in Figure 3.14a, recalling that a *g*-factor close to one is optimal. This benefit can be understood by considering the twisted array design as an array of underlapped simple loop coils, with good gap coverage between them by using the twisted elements, providing good A-P PE performance [35].

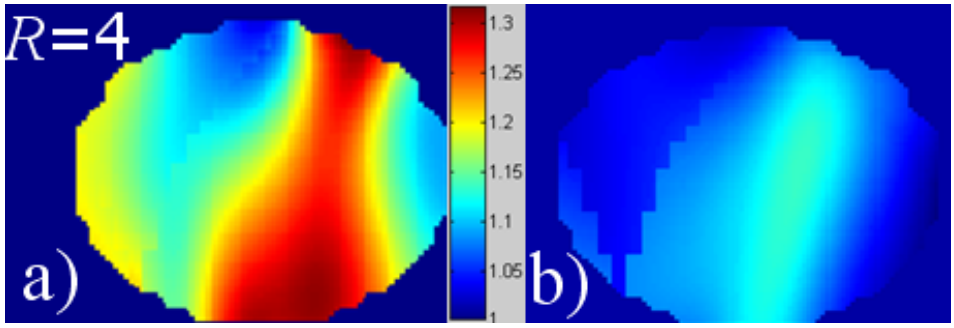

Figure 3.14 – Ratio of *g*-factor maps for $R = 4$ over the central axial slice using the nine-channel simple loop array divided by the twisted loop based array excluding the nine spine elements with a) no outer ring present, and b) outer ring present.

However, these benefits do not outweigh the SNR gains of the surface array. When including the outer ring (intended for *g*-factor improvements) in the computation, the average improvement is less than 9%, shown in the *g*-factor ratio map of Figure 3.14b. The benefits are slightly more reduced when including the nine spine elements to the calculation. The average SNR/*g*-factor ratio for the complete design is better with the simple loop array design.

After determining that overlapped simple loop array is the best approach for the inner core section, the next challenge was in placing eight rectangular coils in a 14 cm by 14 cm space having SNR performance characteristics similar to the nine-channel simple loop array of Figure 3.11a. Through trial and error size variations, rotations and loop

translations, an appropriate eight-channel inner core section was finalized. The resulting conductive trace configuration is shown in Figure 3.15b. Although the geometry changes primarily followed a trial and error process, general MRI design guidelines were used in making educated, or non-random, adjustments. These educated decisions affected overlap amounts, loop sizes relative to their intended imaging depth of interest, and other factors.

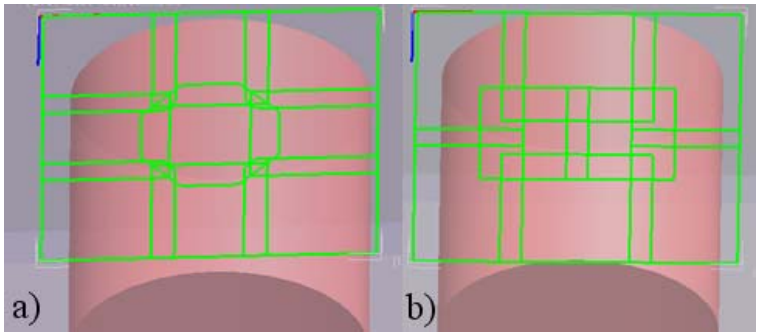

Figure 3.15 – Conductive trace placement for a) nine-channel simple loop array coil design and b) eight-channel finalized inner core design.

For results of the SNR performance loss of using the chosen eight-channel inner core design relative to the nine-channel configuration of Figure 3.15a, refer to the line plot of Figure 3.16. As expected, the nine-channel design provided an upper bound for the SNR of the eight-channel design, but average SNR within the cardiac region falls within 2.25% of the upper bound.

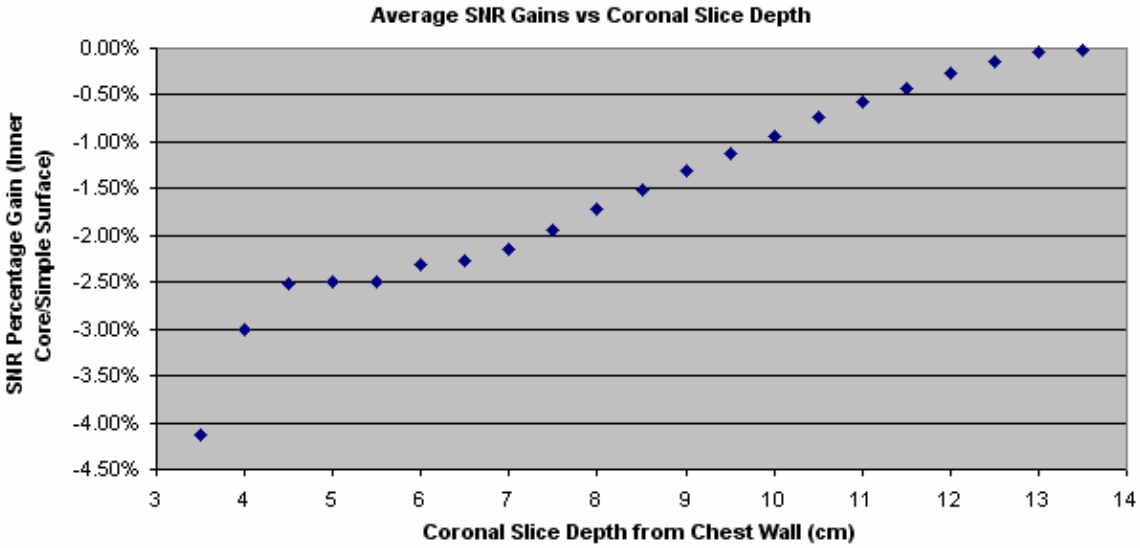

Figure 3.16 – Average SNR gains from eight-channel inner core design relative to the nine-channel surface array, having equal total dimensions, as a function of coronal slice depth.

Considering *g*-factor maps for the inner core by itself, the eight channel design proved better than the nine channel array for a central axial slice, which is shown in Figure 3.17a. This L-R PE *g*-factor ratio using $R = 4$, pertains to a specific slice where the eight element pattern performs better, because four of the array elements lie across the central axial plane, whereas only three are found for the nine channel array, which was specifically considered while designing the inner core.

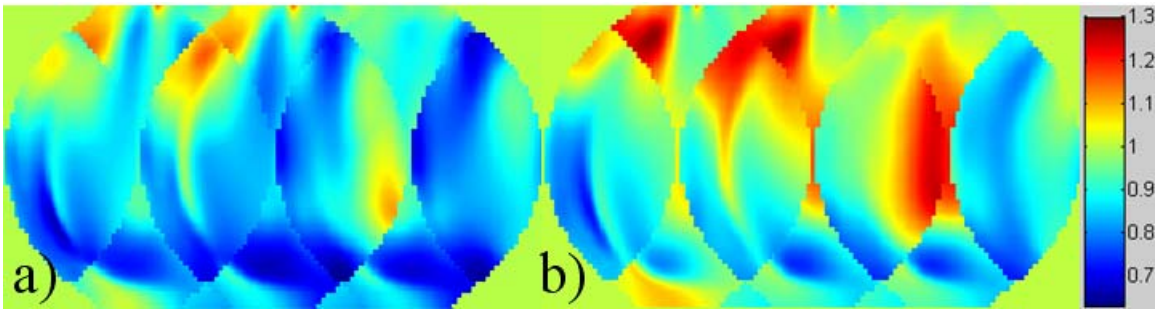

Figure 3.17 – L-R PE *g*-factor map ratios for $R = 4$ of the eight-channel array divided by the nine-channel array for a) a central axial slice, and b) a 4 cm off center axial slice.

Figure 3.17b shows the case for a slice 4 cm off center, where the nine channel array is better. From a qualitative assessment of various slices, it was concluded that the designs are equivalent from a parallel imaging perspective, particularly when adding the outer ring. It was also concluded that the benefit of using a single connector cable for the inner core section outweighed the associated minimal SNR loss for using eight elements. Because of these considerations, it was decided that the inner core section would be comprised of eight elements.

3.4.3 Outer Ring Section Design

The main objective for the eight-channel outer ring is to increase parallel imaging performance within the cardiac region. This behaviour compliments the SNR improvements derived from the eight-channel inner core section to give good overall imaging characteristics. To achieve desirable *g*-factor maps, adequate SNR coverage over the entire sample is required. In addition, coil underlap in the PE direction produces a better *g*-factor map compared to overlapped coils [73][80][12]. The primary design principles applied for modifying the outer ring coil architecture involved:

1) Applying element underlap between coils in the L-R direction.
2) Establishing an overall signal sensitivity FOV no larger than required, such as consideration of the H-F coil length, which is unlikely to be a PE direction.

In practice, MRI technicians are trained to choose the PE direction as the shortest dimension of the chosen FOV. Based on human torso dimensions, PE directions are chosen as L-R or A-P dominant for arbitrary slice orientations, because the H-F direction FOV is much larger. Undesired signal folding results if the FOV in the PE direction is chosen to be too small with respect to the transmit and receive coil spatial sensitivities. This led to the design approach of applying element underlap between the inner core section and the outer ring elements that are adjacent in the L-R, or *x*-axis direction.

As arbitrary slice orientation analysis was beyond the scope of this research, the final design cannot be considered as globally optimal from a parallel imaging perspective. An important note is that a design optimized for PE in the L-R direction would be different than one optimized for the A-P or H-F PE directions. As arbitrary slice orientations are used in clinical MRI, no one coil with a finite number of elements can be optimal for every potential slice orientation, which is why general guidelines are applied during the design process.

The outer ring dimensions were adjusted to determine what size of footprint would satisfy the required parallel imaging performance. As the H-F length of the array is decreased, but held longer than the H-F ROI, average SNR increases and average *g*-factor for L-R and A-P PE decreases within the ROI. However, the tradeoff is that H-F PE *g*-factor maps increase. This creates a design compromise that has no simple solution. As clinical slice orientations can contain an H-F component in the PE direction, the overall array should not be made too narrow. Based on the above relationship and various design computations, the outer ring H-F length was set as 28 cm.

To ensure minimal separation between the patient and the coil, a flexible or arced design in the L-R direction is essential. The total L-R width must provide SNR coverage for the torso in the L-R direction, without being unmanageable for smaller patients. This

is a particularly difficult parameter to optimize because of the wide range of potential chest widths, ranging from 24 cm to 37 cm [63]. An arc length of 36 cm was chosen based on SNR and *g*-factor maps when varying the total L-R width, as well as considering previous design work [7][13][21][73][80].

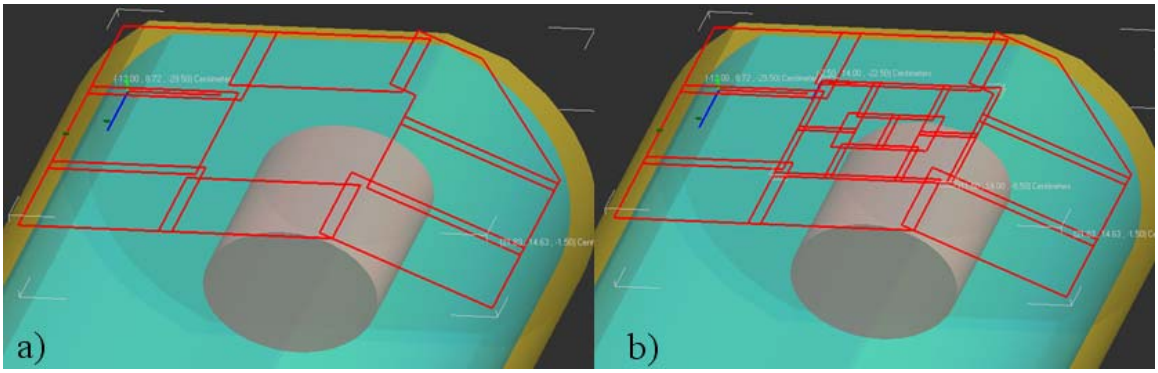

Figure 3.18 – Conductor traces for a) the final eight-channel outer ring design, and b) the entire 16-channel anterior cardiac array.

By centering the outer ring on the inner core section and placing the entire design directly over the cardiac region, better SNR profiles and *g*-factor behaviour results within the ROI. Further improvements are achieved by placing the coil between the human torso and the arm. The improvements result from reducing the distance between the ROI and the coil on the left side of the torso. This puts constraints on the coil geometry, as the position of the shoulder must be accounted for in the design. The conductor placement was adjusted to allow the anterior array to curve underneath the armpit. The eight-channel outer ring is depicted in Figure 3.18a, with the full 16-channel anterior cardiac array shown in Figure 3.18b. To minimize signal coupling, overlap is used between all neighbouring outer ring elements. For combining the outer ring with the inner core, element overlap is used for all cases with exception of the two outer ring elements lying along the central axial slice. Simulations indicated that underlapping these loops with the inner core produces better *g*-factor maps for L-R PE.

For sample axial *g*-factor maps utilizing all 25 elements (16 from anterior cardiac array, nine from OEM spine array) with and without the cardiac region highlighted, applying a reduction factor $R = 5$ with L-R PE direction, refer to Figure 3.19. This *g*-

factor map is very good considering just the ROI, indicating that pulse sequences using R = 5 should produce useful output images.

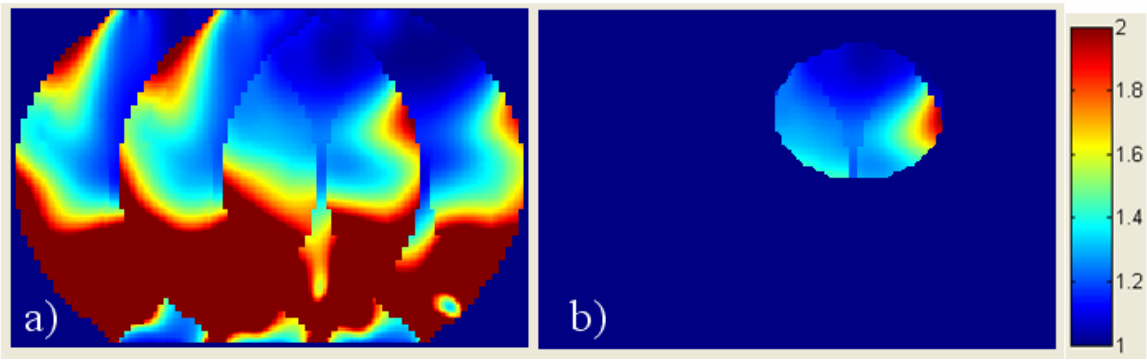

Figure 3.19 - Axial *g*-factor maps from the center of the cardiac region using reduction R = 5 with a PE direction L-R displaying a) full slice and b) only the cardiac region highlighted.

3.5 Design Analysis

3.5.1 Comparisons to Other 16-Channel Anterior Designs

In this section, three different 16-channel anterior cardiac array designs are analyzed using the simulation environment, applying the nine-channel OEM spine array to all anterior designs. Electrical traces for the three different receive coils are depicted in Figure 3.20.

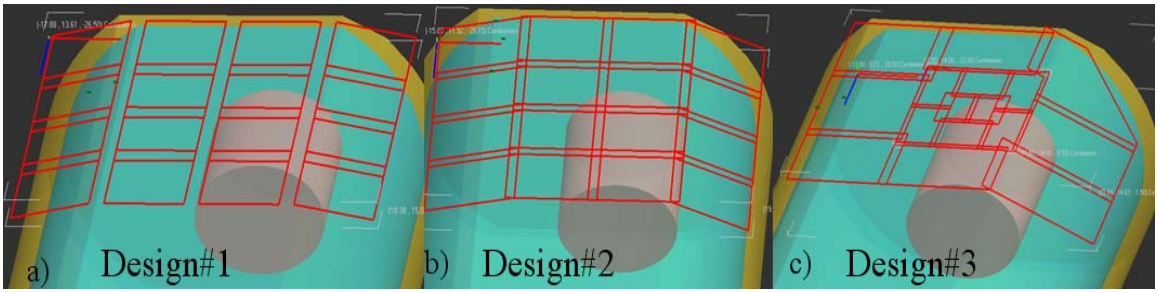

Figure 3.20 – Electrical traces for 16-channel anterior cardiac designs based on a) Zhu et al design [80], b) regular overlapped elements of same total footprint as c), and c) design developed for this thesis.

The anterior cardiac array labeled Design#1, by Zhu et al [80], is shown in Figure 3.20a, where element underlap was applied in the L-R direction to improve parallel imaging in that dimension. Figure 3.20b shows a uniform element anterior array named Design#2, with the same total dimensions as Figure 3.20c, and using overlap between all

nearest neighbours. Comparisons between Design#1 and Design#2 explore potential benefits of utilizing a reduced overall size, or footprint, for improved composite image SNR. Design#3, shown in Figure 3.20c, is the design just discussed that was developed for this thesis. Total array dimensions when extended to a 2D surface are 36.5 cm by 36 cm for Design#1, and 36 cm by 28 cm for both Design#2 and Design#3.

SNR ratio images of Design #3 relative to the two other anterior cardiac arrays for a central axial slice are shown in Figure 3.21. When considering the dashed ROI, it is clear that focusing many small elements near the ROI results in considerable SNR gains (upwards of 200%). Also noted is that SNR is sacrificed in Design#1 relative to the SNR of Design#2 by applying element underlap in an attempt to improve the parallel imaging performance.

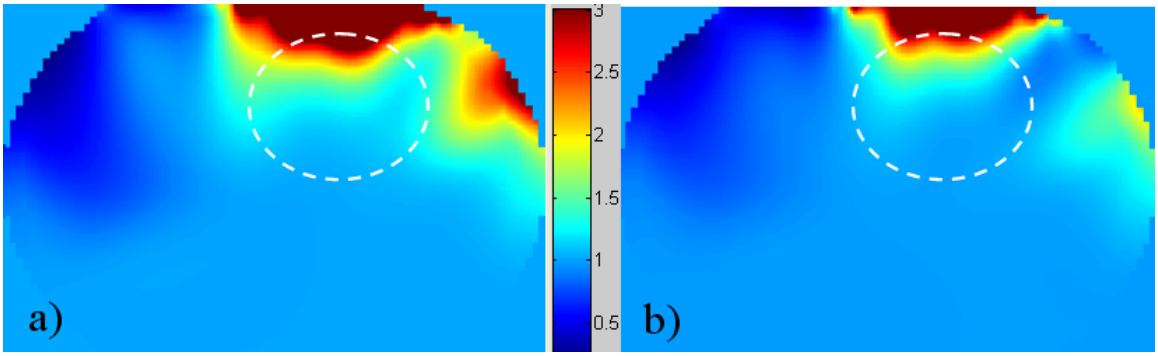

Figure 3.21 – SNR ratio images for a central cardiac region axial slice of Design#3 divided by 16-channel anterior cardiac designs from a) Design#1, and b) Design#2.

Ratio axial *g*-factor maps for $R = 4$ are shown in Figure 3.22 for Design#1 and Design#2 both divided by Design#3 in images a) and b) respectively. Because the *g*-factor ratios are well above one in the ROI, it is clear that Design#3 has a better *g*-factor map compared with either of the competing designs, but suffers in regions far away from the array coil.

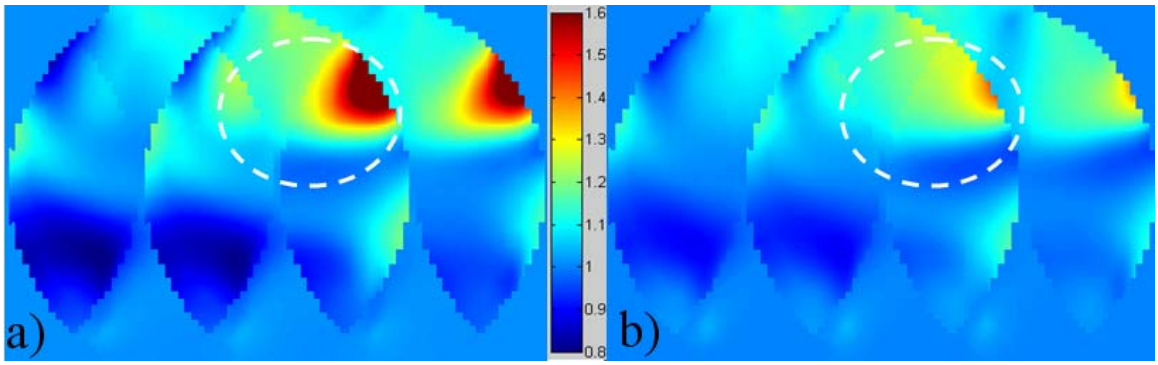

Figure 3.22 – Ratio images for $R = 4$ g-factor maps for a central axial slice using different 16-channel anterior cardiac designs with nine spine elements, being a) Design#1 divided by Design#3 and b) Design#2 divided by Design#3.

As R increases, Design#3 improves relative to both other designs, meaning that a more desirable g-factor map results, which is made clear in Table 3.2. Also, Design#2 has lower average g-factors compared with Design#1, which is also visible from Figure 3.22. This behaviour can be attributed to the smaller footprint used for Design#2, which counteracts the parallel imaging gains associated with applying element underlap, as done in Design#1. This demonstrates that although element underlap can improve g-factor maps for its associated PE direction, as was intended by Zhu et al [80], a better design approach could involve reducing the overall array footprint, while applying element overlap. Consideration of g-factor maps in the A-P and H-F PE directions must also be considered before determining a finalized ideal design.

Table 3.2 – Average g-factors over central 5 cm, or 10 axial slices within the cardiac region.

	$R = 2$	$R = 3$	$R = 4$
Design #1	1.012	1.203	1.880
Design #2	1.010	1.177	1.778
Design #3	1.009	1.081	1.328

A detailed analysis comparing the three design options was conducted for the central 5 cm, or 10 axial slices of the cardiac region. This involved applying reduction factors between $R = 1$ and $R = 4$, while using a L-R PE direction to calculate the predicted composite SNR using equation (2.96). Averaged results, shown as a line plot, are depicted in Figure 3.23.

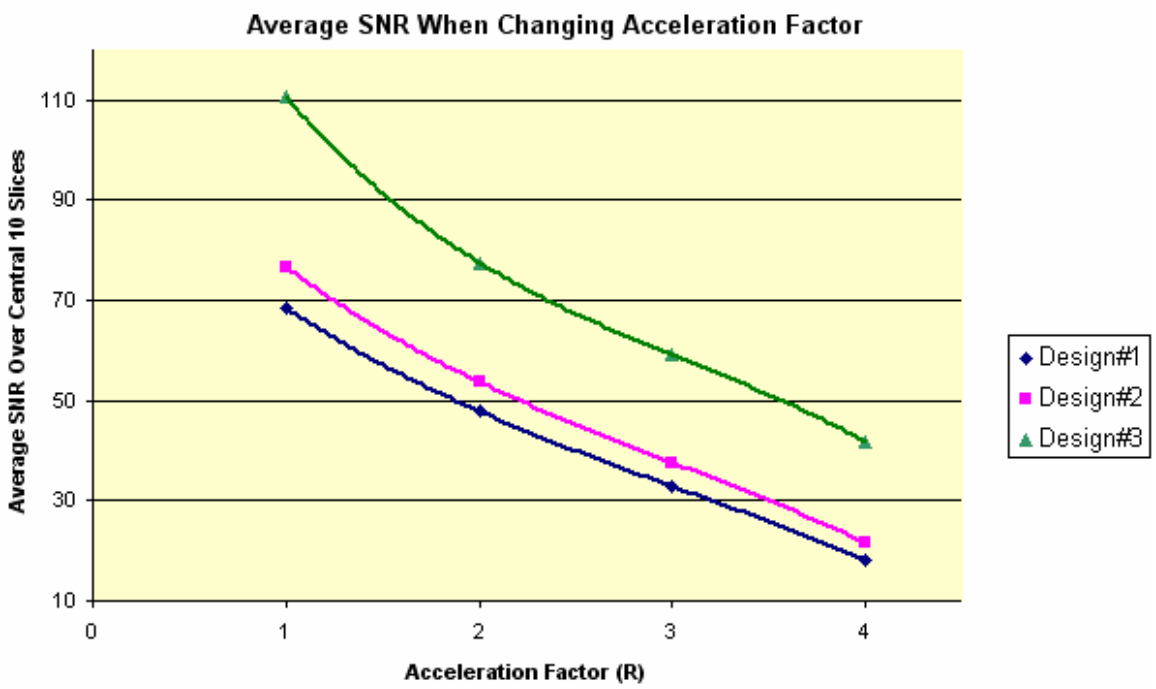

Figure 3.23 – Effects of increasing acceleration factor on average SNR over central 5 cm (*z*-directed axial slices), or 10 slices within the cardiac region, comparing the three different designs.

Design#3 provides superior average SNR for full FOV images, as well as reduced FOV data within the cardiac region. The average SNR gain over Design#1 is 61.6%, 62%, 79.8%, and 128.8% for $R = 1$ through $R = 4$, respectively. An increased SNR gain as R increases indicates that Design#3 has better g-factor maps than Design#1, which is also evident from Table 3.2.

3.5.2 Parallel Imaging Performance within Cardiac Region

The secondary performance requirement stipulates the maximum and average allowable values for axial slice g-factor maps applying L-R PE, with $R = 3$ and $R = 4$. Although the entire FOV images are required to produce g-factor maps within the cardiac region, only values within that ROI are of concern, meaning all supplementary noise levels outside the cardiac region are acceptable. Results of this quantitative analysis relating to these design specifications are shown in Figure 3.24.

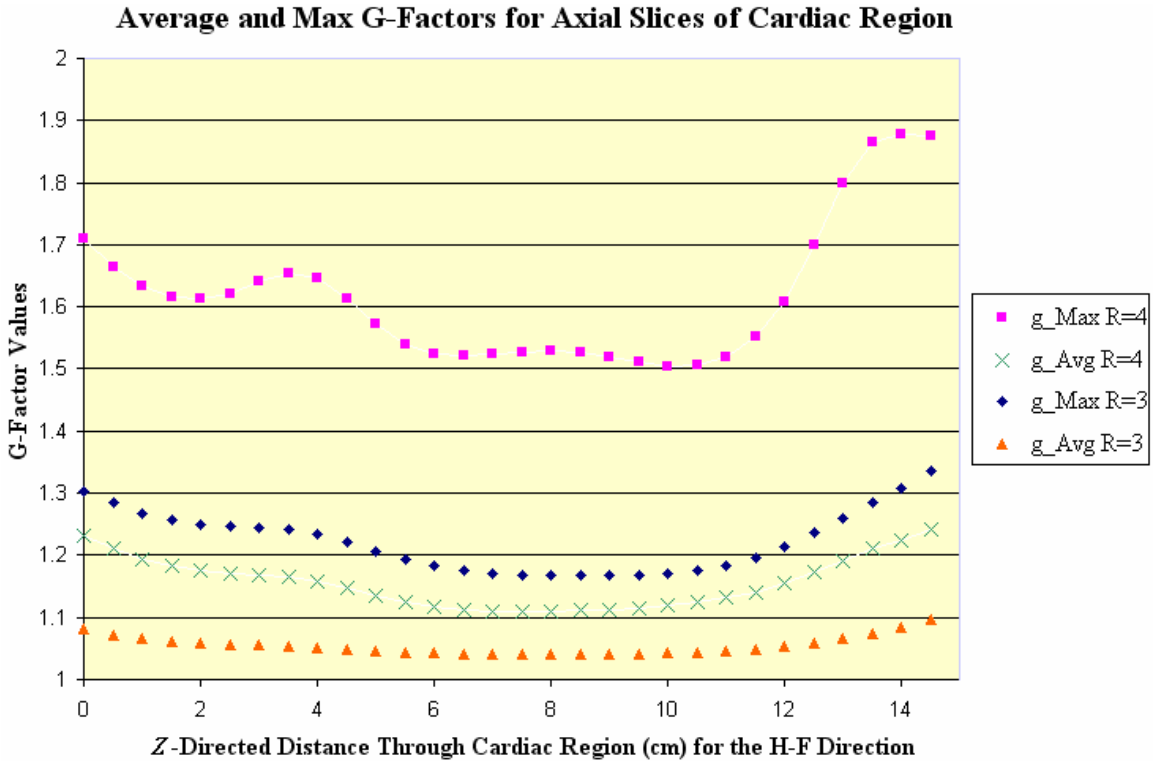

Figure 3.24 – Average and maximum *g*-factors calculated for different axial slices through the ROI thresholded by the cardiac region for reduction factors $R = 3$ and $R = 4$.

The maximum allowed *g*-factor values are satisfied, being limited by 1.5 and 2 for accelerations $R = 3$ and $R = 4$ respectively. When considering average values across the cardiac region for axial slices, both requirements of 1.15 and 1.25 for $R = 3$ and $R = 4$ are also met. As expected, the most favourable performance occurs near the centerline of the design, located at 7.5 cm based on the scale of Figure 3.24. This means that if only a small section of the cardiac region is required, the receive coil should be centered over that area.

3.5.3 Anterior Coronal SNR Near Right Coronary Artery

The primary performance specification requires the ability to achieve ⅓ mm resolution with the same SNR as the six-channel OEM cardiac array achieves using 1 mm resolution across the anterior portion of the right coronary artery, which is located 3 - 4.5 cm below the chest wall. Analysis for this requires comparisons to the existing OEM coil to establish useful SNR values from XFDTD simulations as relative to experimental

results. Full FOV SNR analysis was performed for coronal slices between 3 cm and 4.5 cm depth below the chest wall by taking average SNR values within the design ROI. For a sample SNR gain profile, an axial composite image ratio is given in Figure 3.25, using $R = 1$ and $R = 4$ for images a) and b) respectively.

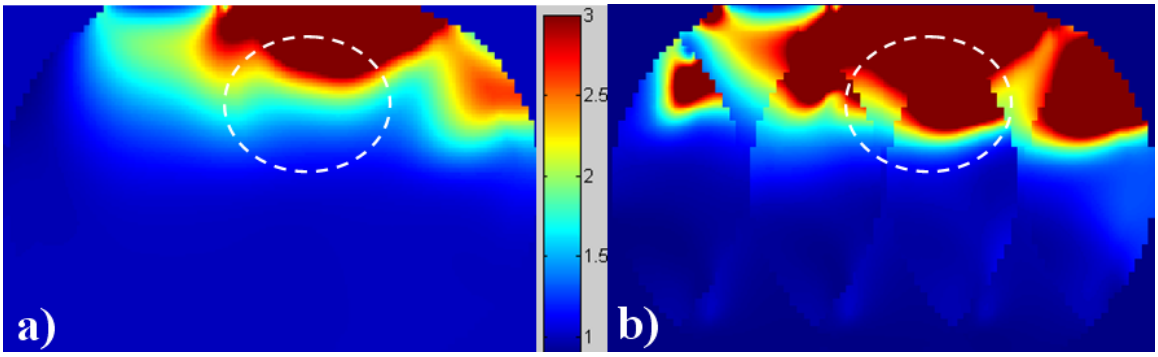

Figure 3.25 – Axial composite SNR ratio for 16-channel cardiac design divided by the six-channel OEM array, both using nine OEM spine loops for a) $R = 1$, and b) $R = 4$ using L-R PE.

An SNR gain of 200% using $R = 1$ for slice depths between 3 cm and 4.5 cm is required for ⅓ mm resolution, and this is satisfied as shown in Figure 3.26. Because the improved resolution is only required for one dimension, choosing that dimension as the FE direction ensures that total imaging time remains constant, which is very important for cardiac imaging. Specifically, to minimize image blurring resulting from motion artifact, patients must hold their breath over the entire duration of the sequence, making the total pulse sequence length important.

Parallel imaging enables a reduction in the total imaging time. Based on a L-R PE direction, SNR gains were also explored in the same region for reductions $R = 2$, $R = 3$ and $R = 4$, shown in Figure 3.26. Note that reductions of $R = 3$ and $R = 4$ would not be performed using the six-channel OEM cardiac array because the resultant image becomes too noisy for clinical use. For purposes of this thesis, the *g*-factor must not exceed two in the ROI for the reduction factor to be considered acceptable.

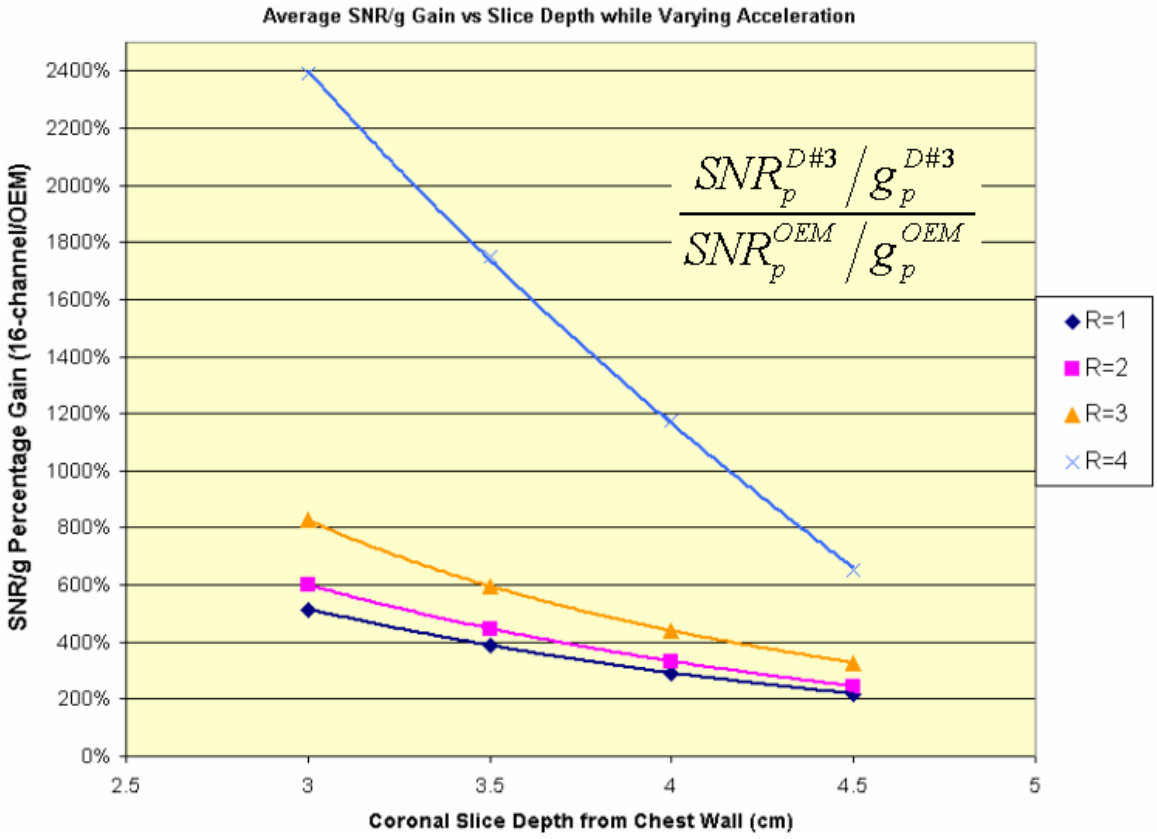

Figure 3.26 – Average SNR gains from 16-channel anterior cardiac array relative to the six-channel OEM cardiac coil using L-R PE, both including nine spine elements. The equation governing this plot is shown in the top right where D#3 refers to Design#3.

The dispersion observed when increasing the acceleration factor in Figure 3.26 demonstrates how *g*-factor maps increase non-linearly with increasing *R*. Recall that the SNR terms are constant as *R* changes, meaning this plot shows how the *g*-factor values play a significant role in output SNR as *R* increases. Because the relative performance of the cardiac array designed here improves with increasing *R*, the 16-channel anterior array will always have at least 200% SNR gains over the OEM array. This indicates that three fold resolution improvement relative to the OEM array, still having better SNR, is achievable for any *R*. The 16-channel anterior array designed here would be capable of producing useful images up to $R = 5$, as verified in Figure 3.27, whereas the OEM array fails for $R = 3$, where the failing criteria is based on maximum *g*-factors exceeding two in the ROI.

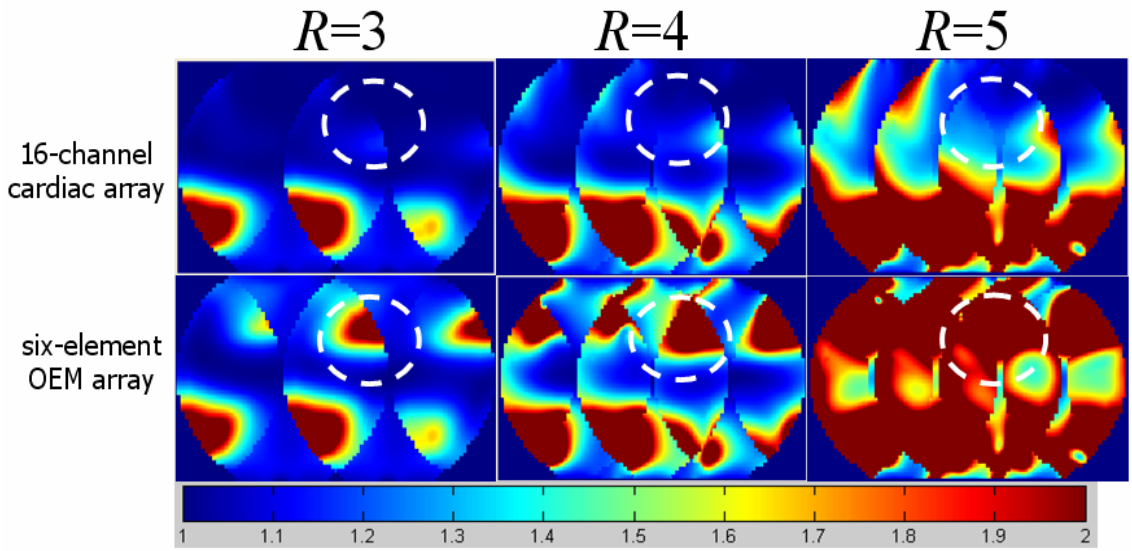

Figure 3.27 - *g*-factor maps for varying *R* values, using nine spine elements with either the 16-channel anterior cardiac array, or the six-channel OEM array.

Note that so far, analysis has been limited to applying the same reductions to both situations. Now, benefits when the 16-channel array applies parallel imaging and the OEM array maintains its full FOV SNR are explored. In other words, SNR improvement in addition to time saving benefits are considered. If the OEM array SNR using $R = 1$ is compared to the 16-channel array when changing *R*, Figure 3.28 results.

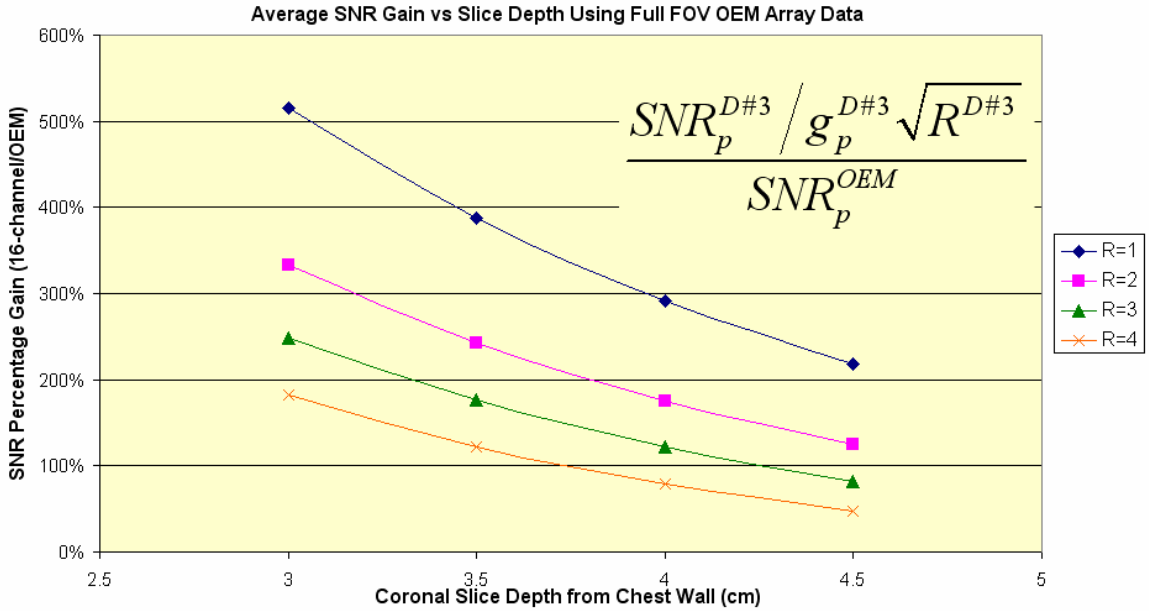

Figure 3.28 - Average SNR gains for accelerated 16-channel anterior cardiac array relative to the full FOV six-channel OEM cardiac coil using L-R PE, including nine spine elements. The equation governing this plot is shown in the top right where D#3 refers to Design#3.

Although positive SNR gains are evident for all slice depths and accelerations considered here, 200% average gain is only achievable with shallow slices. For instance, a 3 cm deep coronal slice could be acquired with three times the resolution, taken using ⅓ the imaging time and still exhibit improved SNR relative to the six-channel OEM coil using the full imaging time. This is an amazing performance benefit. This concludes computational design and analysis, as related to the placement of electrical traces for the 16-channel anterior cardiac array.

3.6 Circuit Design and Electrical Considerations

The first electrical design task was to determine the thickness of electrical trace to use. To ensure a desirable *Q*, meaning a large ratio for unloaded to loaded *Q* measurements, loop resistance must be minimized, which requires changing the electrical trace thickness and analyzing the losses, which is related to the skin effect [48]. However, if adjacent traces are placed in close proximity, as is the case with the inner core section, the designer must also be aware of potential cross-talk, or signal coupling between the adjacent conductors. This effect will reduce the coil's overall SNR, in addition to introducing undesired capacitance.

Table 3.3 - Evaluation of conductive trace options at 123.2 MHz.

Side length (cm)	*Q* Measurement	1/4" Trace	1/8" Trace
4	$Q_{unloaded}$	246	252
4	Q_{loaded}	80	90
7	$Q_{unloaded}$	341	329
7	Q_{loaded}	31	35
13	$Q_{unloaded}$	362	358
13	Q_{loaded}	11	11

For a bench test of conductor losses for a 3T MRI system, corresponding to 123.2 MHz, different sized simple square loops were tuned with four equally spaced capacitors using two candidate copper tape traces, being ⅛" and ¼". The results of these bench measurements are given in Table 3.3. Based on the similar loaded and unloaded *Q* values

between the two candidate conductive traces, it was determined that both options offer similar losses for all loops tested. Also, it was found that the sample loading heavily dominates resistive losses at this frequency, resulting in large ratios for unloaded to loaded *Q* values (>2.5), which is desired for MRI. All electrical traces were chosen to use ⅛" copper tape because the small dimensions of the inner core require intricate tape placement. Overlap adjustments would be far more complicated with ¼" tape.

To ensure standing waves do not form between the tuning capacitors of a loop, a sufficient number of capacitors must be used, placed at various positions around the coil, to electrically break the effective transmission line. An accepted guideline within the MRI industry is to ensure no conductor length exceeds $\lambda / 20$. Assuming wave frequency of 123 MHz and a propagation speed of $2c/3$, for the speed of light *c*, the unbroken copper tape length must be restricted to 8.2 cm. The above mentioned propagation speed is commonly used in microwave circuit analysis to account for material imperfections slowing down the signal transmission. This calculation was based on equation (2.86) using $\mu_r = \varepsilon_r = 1$. Considering the dimensions of the design developed here, restricting sections to below 8.2 cm requires three evenly spaced capacitors for the inner core loops and five evenly spaced capacitors for the outer ring elements.

The array must be electrically 'turned off', or disengaged, while the system is in transmit mode because the coil is intended for receive use only. This requires an immediate switching mechanism to prevent current from flowing, affecting the transmit field when power is being input to the sample. To accomplish this, a small series resonant circuit precisely tuned to the system Larmor frequency ω_0 is placed around one of the tuning capacitors for each loop, with an activation diode to provide control over disengaging the coil. The MRI system applies a DC bias to the diode during transmission, allowing current to flow in the small resonant circuit, which in turn imposes a high-impedance in the larger loop. This small resonant circuit is called an *active trap*, because it requires an active DC bias to trap the current flow. The active trap results in minimal effects during signal reception because loop voltages are too small to bias the diode, but

coil *Q* will drop slightly because of non-ideal diode behaviour in the 'off' state. The active trap can be seen in the sample coil tuning and matching network of Figure 3.29.

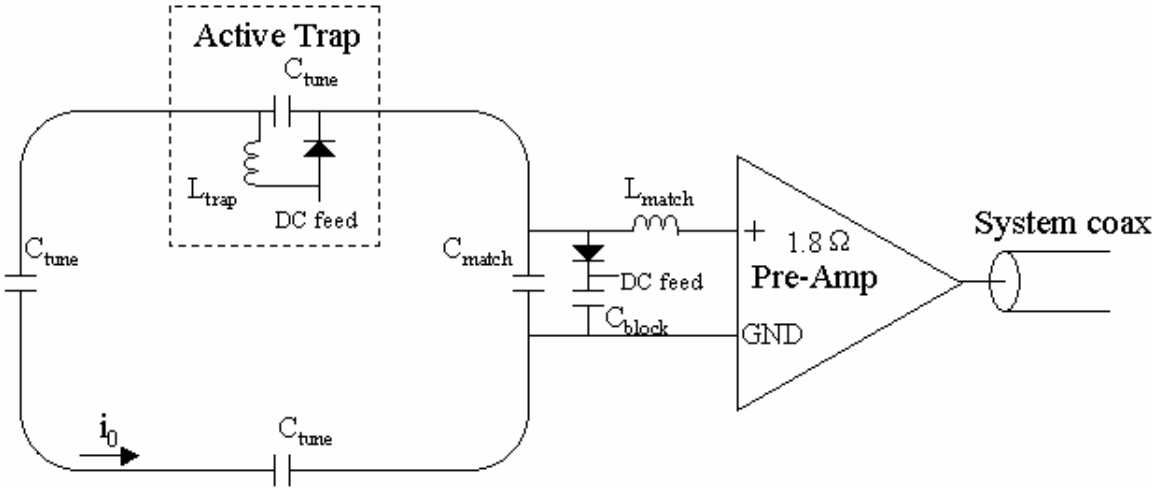

Figure 3.29 - Sample single loop tuning and matching network.

Matching the coil to 50Ω allows for convenient bench analysis using a VNA. For this reason, pre-amps are designed to expect a 50Ω impedance across the input terminals, which is transformed to a high impedance as seen across the matching capacitor C_{match}, as described in Section 2.4.2, to minimize loop currents. The matching network shown in Figure 3.29 provides high-impedance to the loop, while also impedance matching to the output coaxial cable. The high-impedance makes current flow i_0 very small during signal reception, reducing signal crosstalk due to coupling between array channels.

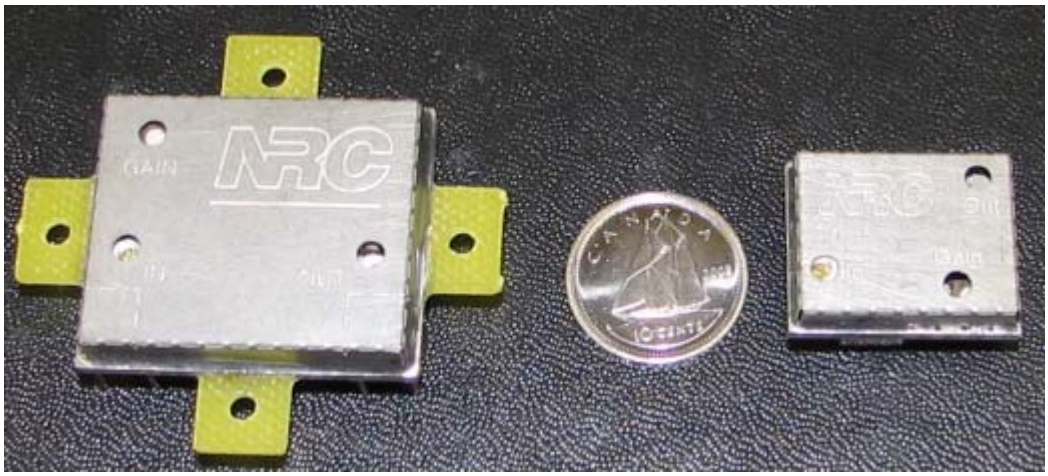

Figure 3.30 – NRC-IBD designed 1.8 Ω input impedance pre-amplifier as seen from (left-right) original sized design, miniaturized pre-amp design required here, and internal circuit view.

The 16 pre-amplifiers used for this project were designed and constructed at the NRC-IBD by miniaturizing an existing design, as shown in Figure 3.30. The pre-amps have a tuned input impedance of 1.8Ω and a noise figure of approximately 0.5dB. They require a 10V DC source from the MRI system for power. The miniaturization was required to place the eight pre-amps within the inner core section.

CHAPTER 4 Experimental Verification

4.1 16-Channel Anterior Cardiac Array Construction

4.1.1 Construction Overview

Construction of the proposed design required an iterative process of tuning, matching and decoupling. Ideally, the entire design should be fabricated using a flexible base piece to allow the array to conform to different shaped subjects. However, sample loading plays a large role in determining the electrical components used for each element, which is difficult to maintain as constant when using a flexible structure. For the prototype developed here, the anterior coil was constructed using a rigid, curved former to ensure stable electrical behaviour during bench tests. Changing the load or the coil position relative to the load, commonly called loading characteristics, will result in a resonance frequency shift and also changes the impedance match of the loop. Applying a flexible former will be more feasible for a second prototype, when general component values and required element overlap amounts are better known.

4.1.2 Iterative Design Process

Unfortunately for MRI coil designers, coupling, loading and matching characteristics are all frequency dependant. Thus, you must tune each coil individually with the load present and all other loops opened before attempting to inductively decouple any elements. Inductively decoupling two neighbouring elements by adjusting their respective overlap will affect the coil's resonant frequency and impedance matching requirement because the conductive traces were moved. Also, the mutual inductance between the coils will change, in turn changing the loading characteristics. This governs an iterative process for array coil design, where each level of complexity requires iterating through all previous levels to make minor adjustments.

For an image depicting the inner core section when adjusting channel overlap to reduce inductive coupling between nearest neighbours, refer to Figure 4.1. Notice that the outer ring section was not present at this stage. All loops that were not being measured were opened, and the S21 measurement probes from a VNA were connected across designated matching capacitors.

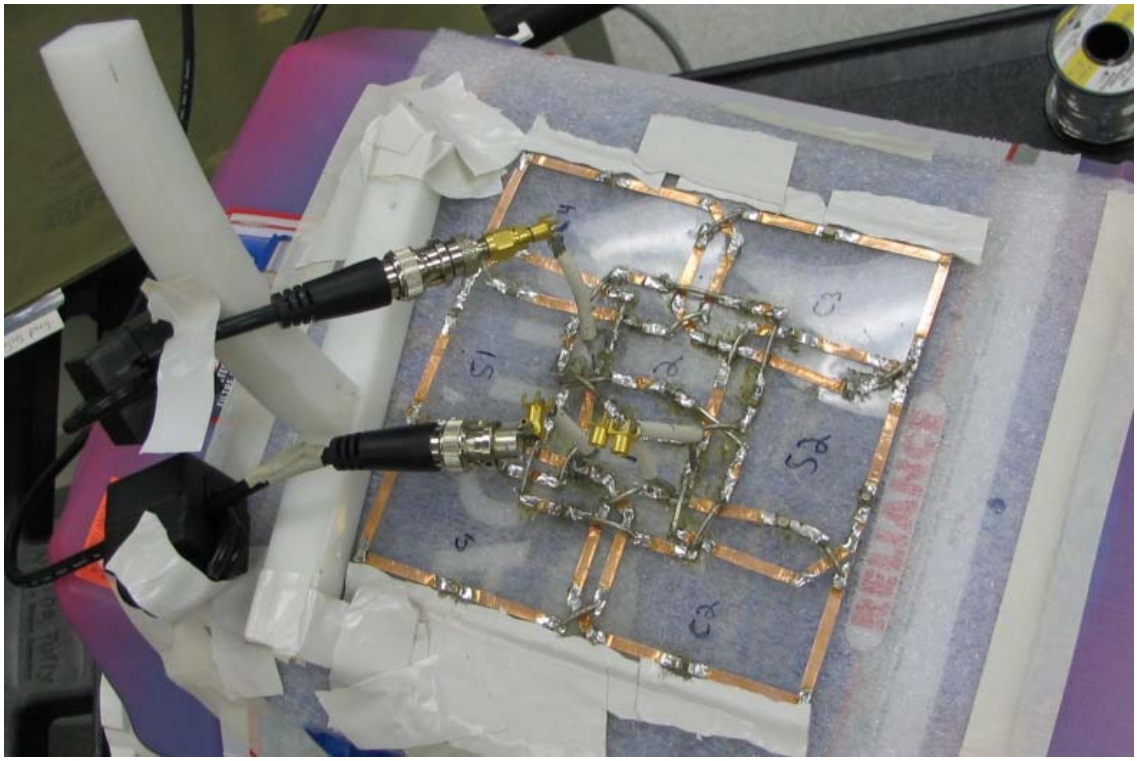

Figure 4.1 - Bench setup for S21 measurement with a VNA to adjust conductor overlap between nearest neighbours for reducing inductive coupling.

The loaded loop isolation values before applying pre-amp decoupling for the inner core and outer ring individually are shown in Figure 4.2 and Figure 4.3 respectively. Based on the defined loop names for the inner core section (shown on the right of the respective figures), it is clear that the highest coupling occurs between loops in close proximity, where no overlap exists. This is observable by considering the coupling between loops #1 and #6 in the inner core. These measurements were taken with all loops that were not being measured opened in two places, before pre-amp the matching circuitry was placed and tuned.

Inner Core								
	#1	#2	#3	#4	#5	#6	#7	#8
#1								
#2	-13.6							
#3	-16.1	-12.1						
#4	-12.3	-16.3	-15.2					
#5	-13.8	-13.5	-7.6	-7.0				
#6	-6.6	-6.8	-13.1	-12.8	-10.7			
#7	-12.0	-9.2	-9.3	-12.3	-11.8	-14.3		
#8	-9.1	-11.4	-12.9	-9.2	-13.4	-12.7	-9.8	

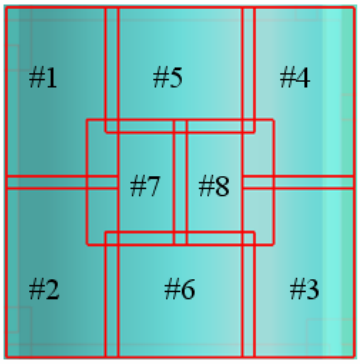

Figure 4.2 – Loaded S21 magnitude isolation values (dB) at 123.2 MHz between inner core loops after adjusting element overlap on the bench with showing their associated positions.

A similar assessment of designs where underlap is intentionally applied, such as Design#1 from Section 3.5.1, will show less desirable loaded isolation matrices compared to that of Figure 4.2, which effectively places more emphasis on pre-amp decoupling to ensure isolated receive signals for the array coil. The individual channels for this research have much better isolation values after the pre-amp matching circuitry is connected and tuned.

Outer Ring								
	#1	#2	#3	#4	#5	#6	#7	#8
#1								
#2	-17.8							
#3	-15.8	-16.3						
#4	-31.0	-25.0	-17.0					
#5	-23.0	-35.0	-18.3	-15.0				
#6	-31.0	-29.0	-28.5	-13.5	-18.0			
#7	-14.5	-34.0	-24.2	-24.0	-16.0	-18.0		
#8	-16.0	-20.0	-28.3	-38.0	-30.0	-25.0	-28.0	

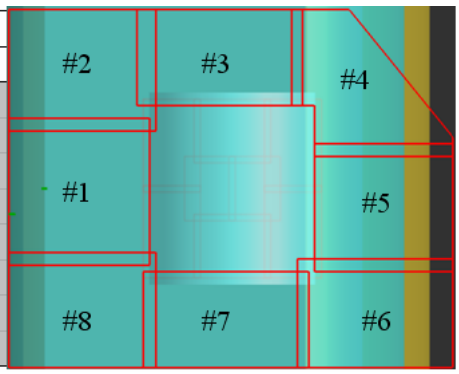

Figure 4.3 – Loaded S21 magnitude isolation values (dB) at 123.2 MHz between outer ring loops after adjusting element overlap on the bench with showing their associated positions.

The next construction step required selecting one tuning capacitor per element, to be used as part of the active trap. Each active trap was tuned to 123.2 MHz, and then set in place with hot glue, fixing the associated capacitors' value. Finally, the pre-amp matching circuitry and interfacing cables were connected, permitting bench measurements of the same arrangement as that during experimental trials. The measured unloaded *Q* values for all active traps and matching circuitry resonators are given in

Table 4.1. These measurements must be carried out on the sub-circuits as stand-alone structures. The active trap diodes were DC biased for measurements, as were the pre-amps for matching circuitry measurements.

Table 4.1 – Unloaded Q values for active traps and matching circuits for all channels.

	Inner Core								Outer Ring							
	#1	#2	#3	#4	#5	#6	#7	#8	#1	#2	#3	#4	#5	#6	#7	#8
Unloaded Q (active trap)	93	89	94	102	104	91	90	82	99	113	112	107	95	108	105	113
Unloaded Q (matching cct)	100	92	92	94	96	91	88	110	86	92	88	95	92	94	99	95

All channels required a final tuning pass to correct for any effects of having all other elements electrically closed and terminated with pre-amps. At the system interfacing coaxial cable connection point, a tuned cable trap must be mounted to each element. This trap serves the purpose of reducing current flow along the shield of the coaxial cable during system transmission. Without these traps, very large current will flow along the coaxial ground, creating undesired $\vec{B}_1$ artifacts.

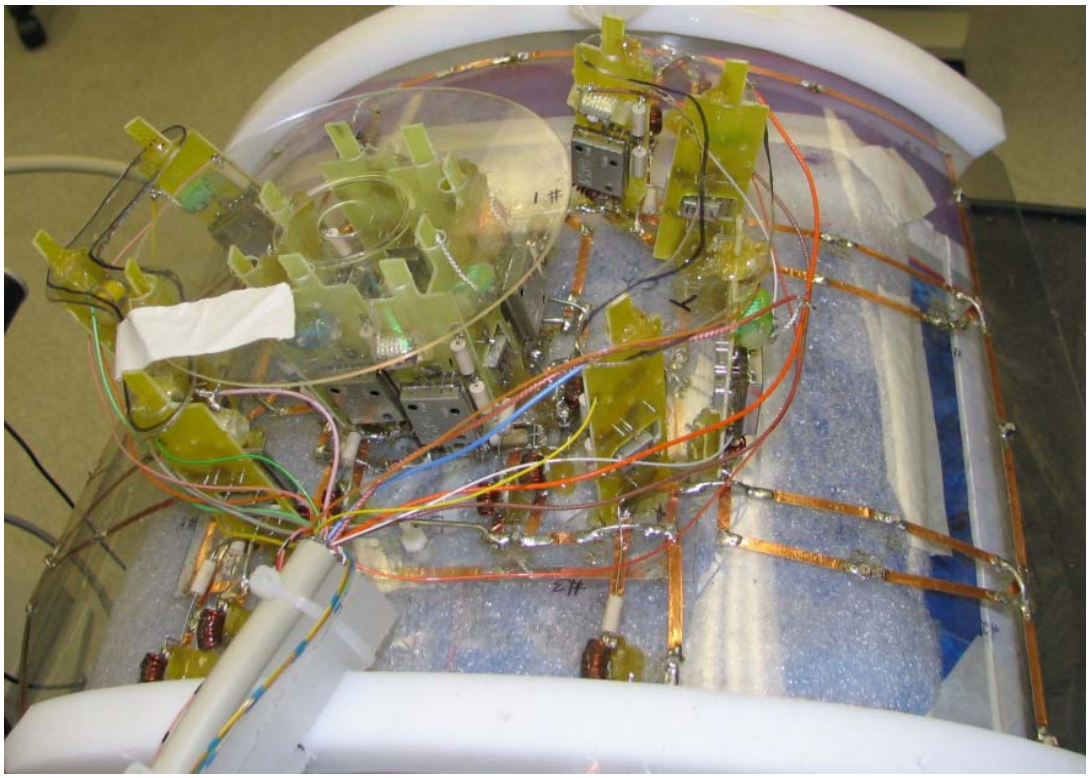

Figure 4.4 - 16-channel anterior cardiac array after inductive decoupling through overlap adjustments, active trap installation, pre-amp matching circuitry and system interfacing cable placement for the outer ring section.

To view the 16-channel anterior cardiac array with all pre-amps installed, as well as having the outer ring system-interfacing cable connected, refer to Figure 4.4.

4.2 Experimental Results

4.2.1 Setup

Experimental data was acquired with a clinical 32-channel 3T Siemens Trio Tim system located at the NRC-IBD. The phantom was a gel based solution of sucrose, KCl, TX151 and Dowicil75, filling a five gallon jug of dimensions 28 cm×25 cm×37 cm for width, height and length respectively. This phantom, which was also used on the bench during the coil tuning process, was thought to exhibit similar loading and wave behaviour characteristics compared to a human torso. Recall the torso dimensions for computations were larger, being 40 cm×26 cm×64 cm, which changes parallel imaging behaviour for L-R phase encoded axial images because the width is different. For this purpose, computational analysis was also performed using a phantom equivalent to that from experiment so accurate comparisons between simulation and experiment could be made.

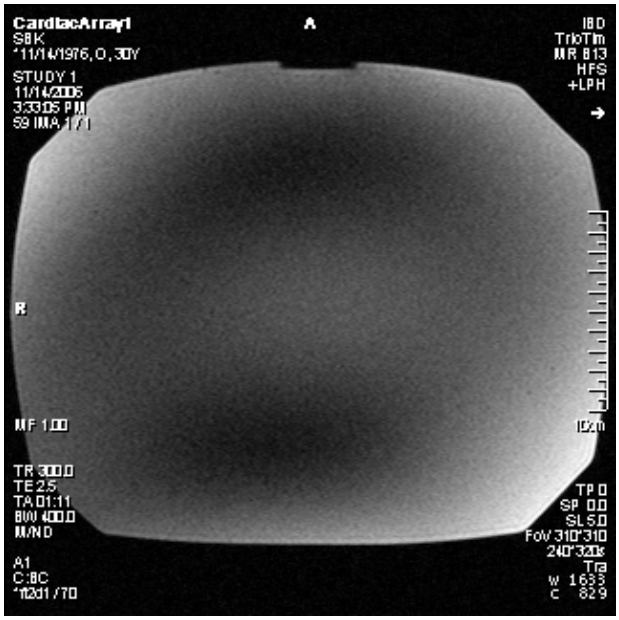

Figure 4.5 – Resultant image using the system body coil for transmit and receive. Having a non-uniform SNR distribution demonstrates that the transmit field is non-uniform.

Experimental results were obtained using the built-in body coil for the transmit mode, where the 16-channel anterior cardiac array designed here and the six-channel OEM array, both in conjunction with nine OEM spine elements, were used for signal reception. A resultant image when using the body coil for both transmit and receive is shown in Figure 4.5, demonstrating that the applied transmit field is somewhat non-uniform. Although wave behaviour of this nature is expected for large objects at 3T, it nonetheless establishes an error source relative to the computations, where a uniform transmit field was assumed. Predicted effects associated with this excitation image include improved A-P PE *g*-factor maps, but reduced SNR in the darker areas of the phantom, some of which correspond to our cardiac ROI and the coronary artery region.

Noise images were essential for determining the noise correlation matrices for the arrays, which were found by applying equation (2.69) after acquiring images without using any transmit power, meaning a zero flip angle everywhere. Both the anterior cardiac array designed here and the OEM array coils were centered on the phantom. As such, the cardiac region was treated as L-R centered for experimental analysis, but having the same geometrical size characteristics.

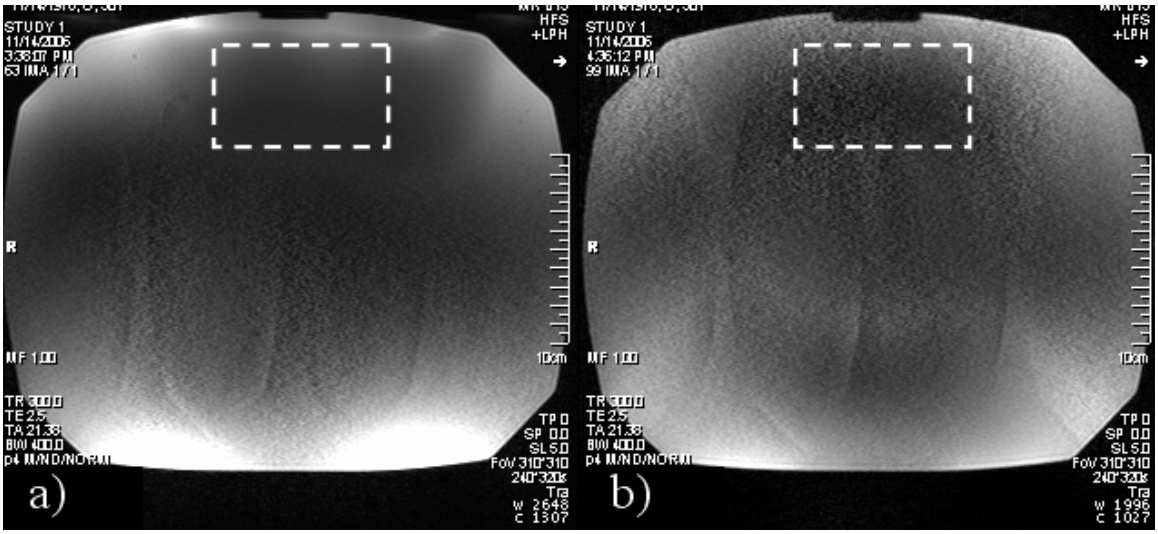

Figure 4.6 – Partially signal normalized composite images from a GRAPPA $R = 4$ pulse sequence using the nine element OEM spine array with a) the 16-channel anterior cardiac array, and b) the six-channel OEM cardiac array.

A Flash imaging sequence was used, with $T_R = 300$ msec and $T_E = 3.46$ msec, applying flip angle $\alpha = 70^\circ$ with a 5 cm slice width. For all axial slices analyzed here, an A-P FOV of 256 mm was used, with L-R FOV of 310 mm. For the output images sized 240×320, this gives approximately 1 mm resolution in both dimensions. A variety of slice locations and orientations were acquired, both using full FOV imaging and applying parallel imaging with built-in pulse sequences for reductions up to $R = 4$.

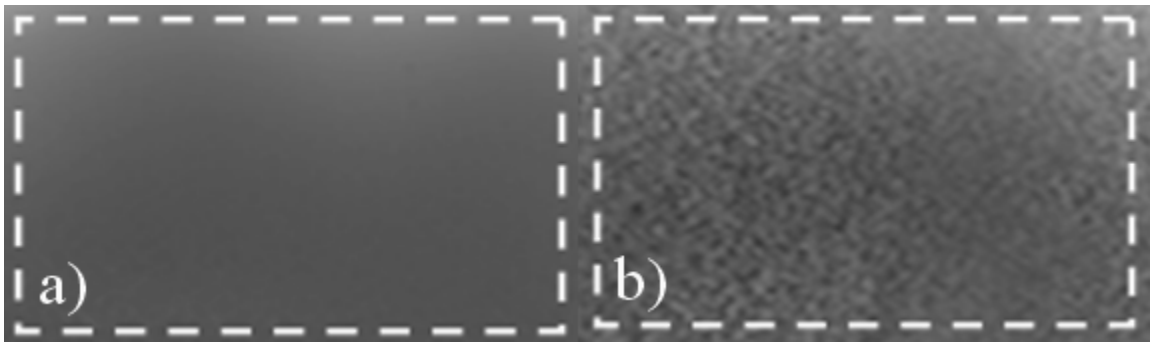

Figure 4.7 – Zoomed in view of dashed regions from Figure 4.6 for a) the 16-channel anterior array and b) the six-channel OEM array.

Sample images from both coil arrangements using GRAPPA at $R = 4$ are shown in Figure 4.6. Note that the Siemens system performed grayscale normalization corrections for the anterior array elements, but not the spine elements, meaning the white sections at the bottom of the images do not correspond to the highest SNR values. The composite image of Figure 4.6a shows low noise levels near the top for our uniform sample. The same region in Figure 4.6b appears speckled, or noisy, which indicates poor image SNR. Figure 4.7 shows a zoomed in view of the dashed regions of Figure 4.6.

4.2.2 SNR for the Anterior Right Coronary Artery

To experimentally evaluate SNR performance as a function of depth, an axial slice was taken, positioned at the center of both anterior cardiac arrays, as well as being centered above the three rows of spine elements. Recall that according to project specifications, three-fold SNR gains must be observed in the depth range of 3 cm - 4.5 cm to allow for ⅓ mm resolution across the anterior portion of the right coronary artery.

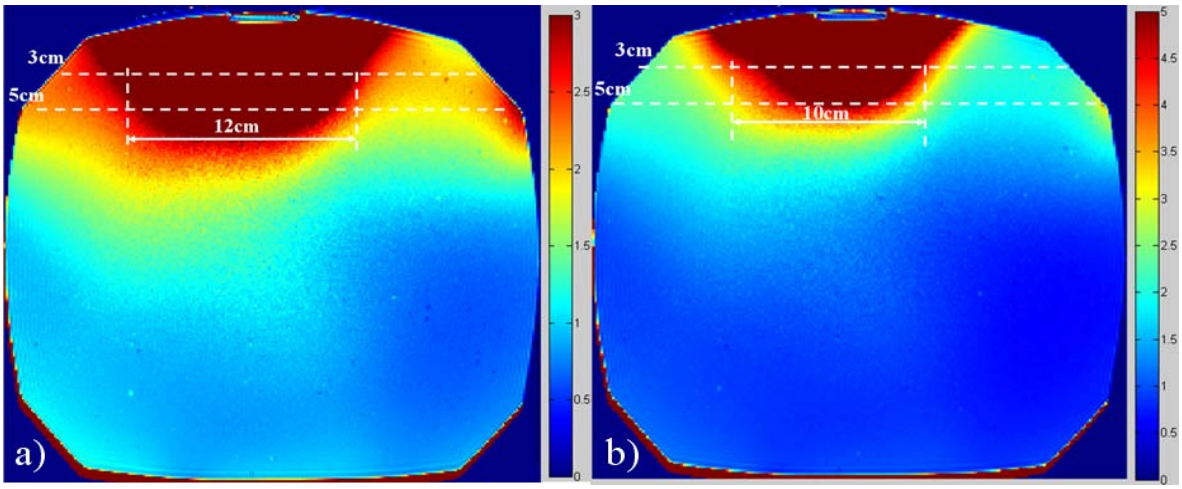

Figure 4.8 – Experimental SNR ratio images from the 16-channel anterior array divided by the six-channel OEM cardiac array, scaled to a maximum gain of a) 200% and b) 400%.

SNR ratio images from experimental data, when using different scaling maxima are shown in Figure 4.8. For the depth range of 3 cm - 5 cm, the new design displays average SNR improvements well in excess of the required 200% over the 12 cm L-R distance shown in Figure 4.8a. Average experimental SNR gains within the 12 cm by 2 cm dashed region of a) are 421%, where average gains of 460% are found in the 10 cm by 2 cm region of Figure 4.8b. Thus, it is inferred that ⅓ mm pixel resolution having useful SNR across the anterior portion of the right coronary artery is realizable.

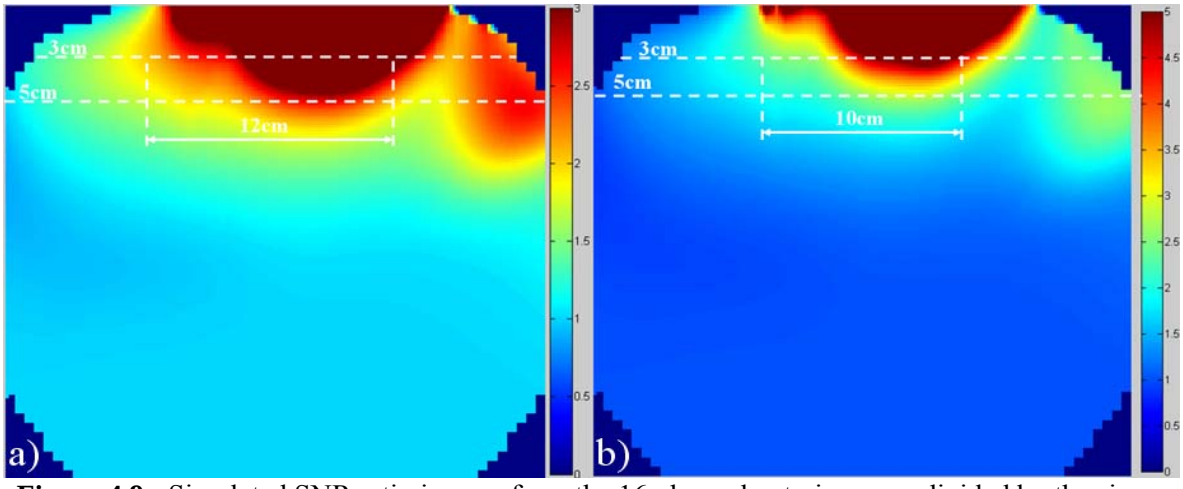

Figure 4.9 - Simulated SNR ratio images from the 16-channel anterior array divided by the six-channel cardiac array, scaled to a maximum gain of a) 200% and b) 400%.

Computed data from an equivalent setup to the experimental one from Figure 4.8 is displayed in Figure 4.9. Although similar patterns are evident, the experimental data

shows better SNR gains than those predicted from simulations. The predicted SNR gains for the regions were calculated to be 207% and 221%, for Figure 4.9a and b) respectively. The most likely cause for the difference between calculated and experimental gains is construction related.

As the 16-channel array was designed using the phantom being applied for imaging, it likely has better load matching characteristics than those of the six-channel OEM coil, which was designed with a different sample load. Also, the separation distances between the coil and the sample likely did not match perfectly between simulation and experiment, particularly as simulation results were based on a 5 mm discretized mesh. The simulated separation distances were 1 cm and 2 cm for the new design and the OEM array respectively. Considering those sources of error, it is determined that consistency between simulation and experimental data was achieved.

4.2.3 Parallel Imaging Performance within the Cardiac Region

Analysis of experimental *g*-factor maps was performed using the axial slice data from Figure 4.8 and Figure 4.9 over acceleration factors between $R = 2$ and $R = 5$. Because the sample size from experiment has different dimensions than the simulated human torso in the desired, L-R PE direction (28 cm versus 40 cm), matching *g*-factor values from experiment according to project specifications is not a valid goal. However, by showing that simulation and experimental *g*-factor maps are in agreement for the reduced phantom, which is done in Figure 4.10, the simulated parallel imaging analysis from Section 3.5.1 for a human torso is also validated.

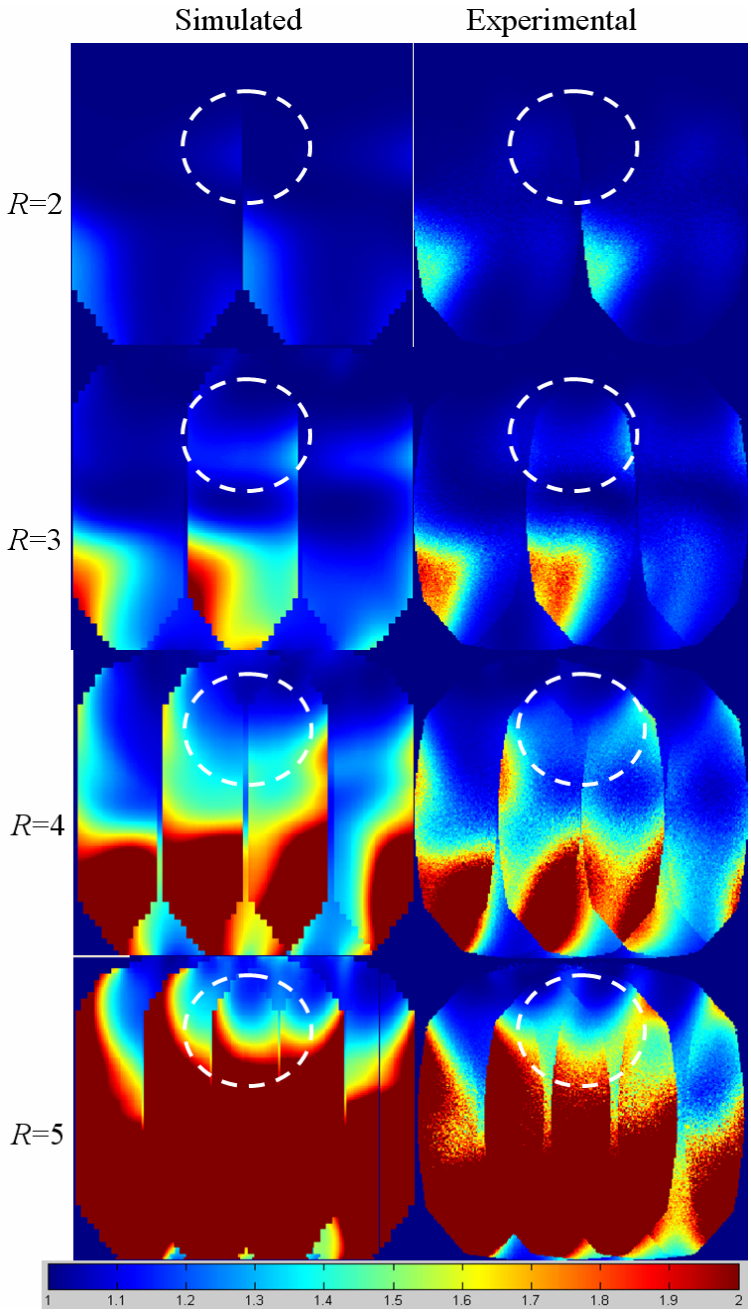

Figure 4.10 – Simulated and experimental *g*-factor maps at accelerations $R = 2$ through $R = 5$ for 16-channel anterior array for a L-R PE central axial slice.

Based on the *g*-factor maps of Figure 4.10, good agreement between calculated and experimental behaviour is shown, which verifies the results of Section 3.5.1. The dashed white line is intended to provide a general outline of where the cardiac region lies from a depth and width perspective. It was placed in the sample L-R center only to reflect where the coil centerline was located for experimental tests. Although this simulation has

very similar *g*-factor profiles to those found experimentally, the average simulated *g*-factor is lower for $R = 2$, where the average experimental *g*-factor is lower for $R = 3$, $R = 4$ and $R = 5$. The absolute difference is not important because the two samples are not perfectly matched, nor do they have equivalent image resolution. The important measurement here involves qualitatively comparing the contours.

An extension to the above analysis involves applying the experimentally obtained SNR gains to Figure 3.28, instead of the simulated ones. In this scenario, the line plots for increased *R* would be more favorable towards the new cardiac array design. It would be possible to apply $R = 3$ and acquire with ⅓ mm resolution while still having improved SNR. To verify this extension, different samples should be imaged with to explore the effects of experimentally imaging with the same sample as used during array development.

To visually explore the effects of reducing PE direction sample size, consider Figure 4.11. Within the dashed cardiac region, *g*-factor values do not exceed 1.5 at $R = 5$ when applying parallel imaging based on a 40 cm wide human torso, as shown in Figure 4.11b. This indicates that images with low noise and wrapping artifact should be clinically attainable at this *R*, when considering the cardiac region of this central slice. However, the 28 cm wide simulated phantom, shown in Figure 4.11a, depicts a far less desirable *g*-factor map for the same acceleration ($R = 5$). This clarifies why the same phantom dimensions must be used for any comparisons between different MRI designs.

From a data perspective, we will assume a fixed amount of signal and time required per PE step, considered for a unit distance. From this perspective, a sample of dimension 28 cm requires 30% less imaging time than one having a FOV of 40 cm. By this analogy, the effective acceleration associated with Figure 4.11a relative to that of Figure 4.11b, taken as a full FOV sequence, can be thought of as $R = 6.5$, which is calculated from $R = 5 * (40/28)$.

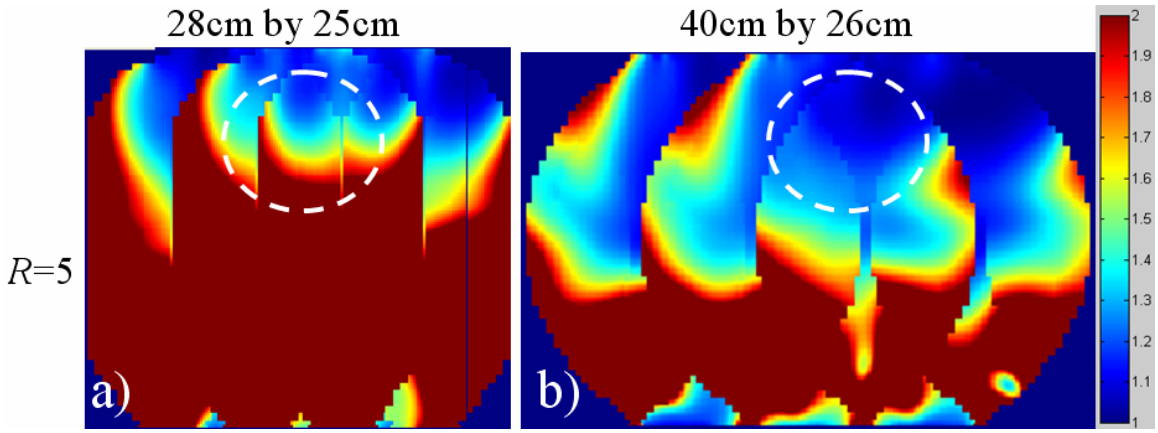

Figure 4.11 - Comparison of effects of PE direction sample size changes on *g*-factor maps for acceleration factor $R = 5$ between a) 28 cm L-R sample width, and b) 40 cm L-R sample width.

The experimental work presented in this chapter verifies that the SNR gains predicted from computational analysis are accurate. Also, the parallel imaging capabilities from experiment show good agreement with those from simulation. The 16-channel anterior cardiac design presented here yields significant improvements in both full FOV SNR and parallel imaging abilities relative to the previous 16-channel anterior designs from industry.

CHAPTER 5 Conclusions and Future Work

5.1 Conclusions

The Matlab based program written for MRI design evaluation using post-processing XFDTD field outputs served as an essential tool for design analysis. The program is capable of displaying SNR for single channels and array coils based on both XFDTD simulation data and Siemens raw output data. The composite images can be analyzed from a parallel imaging perspective and compared to other designs to establish relative performance improvements. Using this software with simulated data, the six-channel OEM chest array was analyzed to establish the required SNR improvements for ⅓ mm resolution in the anterior region of the right coronary artery.

The 16-channel cardiac array was divided into two different eight-channel sections, named the inner core and the outer ring. The methodology of this design approach was to concentrate smaller elements in the inner core, for SNR gains specifically in the ROI relative to previous 16-channel designs having a uniform grid of elements. Larger elements were designed in the outer ring region, for coverage as required for parallel imaging performance, while maintaining a small number of channels. While analyzing potential inner core section design options, it was found that twisted loops should be used to optimize SNR behaviour at depths between 9 cm and 14 cm for a structure of dimensions 14 cm by 14 cm. It was found that *g*-factor maps when using twisted arrays independently are much better as compared to an overlapped grid of simple loop coils for the inner core. However, for this design, the g-factor benefits were dampened when simulating the full 25-channel array. Because of the improved SNR characteristics at the concerned depth region here, being 3.5 cm to 5 cm, the eight-element inner core section was finalized based on simple loop coils.

The eight-channel outer ring section was then designed, focusing on *g*-factor maps within the defined cardiac region. The outer ring section was designed to have overlap between all neighbouring elements. For interfacing the outer ring with the inner

core, overlap was applied with exception to the elements lying above the central axial slice position. Based on simulations, underlap was applied here to enhance L-R *g*-factor maps. Upon finalizing the 16-channel anterior cardiac array, computational analysis relative to the six-channel OEM cardiac array demonstrated that the required SNR is achieved for ⅓ mm resolution. Based on simulations, it was concluded that acceptable images at acceleration factors up to $R = 5$ are achievable.

Next, simulation comparisons were made to other 16-channel anterior cardiac arrays that were designed using a more symmetrical geometry. Average SNR/*g*-factor gains of 61.6%, 62%, 79.8%, and 129% were calculated, when applying $R = 1$ through $R = 4$. The design benchmark for this case was a 16-channel anterior array designed by an industry research group. These results show that the design developed here offers significant improvements, verifying the proposed hypothesis of concentrating smaller elements directly above the ROI. Increased average SNR/*g*-factor gains as *R* increases indicates that this design has more desirable *g*-factor maps than previous designs.

Prototype construction was required to verify the calculated SNR and *g*-factor gains. Inductively decoupling and connecting appropriate matching circuitry required an iterative design process. Experimental images were obtained using the 16-channel anterior cardiac array with a nine-channel OEM spine coil, interfaced to a 3T Siemens Trio Tim system found at the NRC-IBD. A GRAPPA reconstruction at $R = 4$ demonstrated a crisp image as available using the design developed here, where the six-channel OEM array provides a very noisy output image. Averaged SNR analysis showed experimental gains over the six-channel OEM array of 460% for a 10 cm wide section of a central axial slice for the depth between 3 cm and 5 cm. This verifies that ⅓ mm pixel resolution is available, where only 200% SNR gain was required to satisfy this requirement. As an average measure, 460% SNR gain implies that ⅓ mm pixel resolution in addition to using $R = 3$ can be used to attain useful resulting images at this depth. The experimental data implies that better resolution than what was predicted is available with this cardiac array. Based on experimental data, sequences with isotropic resolution of ½ mm by ½ mm, while applying $R = 2$, should produce images with good SNR.

The experimental sample width differed from the intended human torso size (28 cm vs 40 cm), resulting in significantly different *g*-factor maps between the experimental data and the simulated data that used the human torso model. For this purpose, experimental data was used to verify the contours and values of *g*-factor maps calculated in the XFDTD environment when using the same sample size as that from experiment. Based on this comparison, simulated results when using the human torso model were accepted for satisfying parallel imaging abilities. Using $R = 4$, the maximum and average *g*-factor throughout the cardiac region does not exceed 2 and 1.25 respectively. Using $R = 3$, maximum and average *g*-factors are below 1.5 and 1.15.

5.2 Limitations and Assumptions

Parallel imaging performance analysis is strongly dependant on object shape and orientation, demonstrated by the fold lines shown in Figure 3.2 and Figure 4.11. Depending on the reduction factor and chosen FOV, these lines may or may not fall within the desired ROI. For this reason, it is important for design comparisons to be based on an equal sized object, FOV and reduction factor.

For the simulations of this research, perfect inductive decoupling was assumed between all coil pairs. Also, required electrical components and sub-circuits were simplified, resulting in less coil resistance and signal losses. Finally, the RF receiver chain was ignored because resultant signal losses from this circuitry are equivalent for all potential designs, thus all designs are affected equally.

The design presented here was limited to analysis at 123.2 MHz, associated with a 3T MRI system. For comparisons to previous 16-channel anterior cardiac designs, the coil geometry was adapted to a 3T environment, where it was originally designed for a 1.5T system. This extension was required as currently no literature could be found for an equivalent cardiac array developed for a 3T system.

5.3 Future Work

5.3.1 Product Development

This cardiac array design has potential to be marketed as a product for clinical use. Developed here was a first stage prototype, not ready for human testing as it has not been properly safety tested. Prior to performing clinical tests on human patients, high power testing requirements must be satisfied, in addition to successfully completing other safety regulations. A clean and visually appealing casing would be required to ensure no component damage occurred during use or storage.

A product based extension, or second stage prototype, should include a flexible casing to ensure minimal coil separation over a variety of different body types and patient geometries. A flexible housing also presents an extension to different imaging regions, such as pelvic, spine or knee for example. For use in a clinical setting, this design should be evaluated based on other parallel imaging techniques, such as GRAPPA and SMASH, to establish clear usage guidelines for researchers and technicians. This will involve outlining the best PE directions for different slice orientations, and which reduction factors will produce useful output images for different FOV settings.

5.3.2 Design Improvements

Current clinical MRI systems have up to 32 channels available. This presents an opportunity to extend the 16-channel design presented here to something of a larger scale. This requires closer evaluation of exactly how many spine elements should be used for adequate cardiac imaging, which would outline a maximum number of available anterior elements. It is noted that when using the 3T Siemens Trio Tim system, various channel combining options are available for the spine array. An example involves combining signals from six spine elements into just two independent channels.

Also, SNR benefits should be explored resulting from increasing the number of elements in the inner core section. Related to SNR behaviour at a given depth as a function of coil size, expanding the dimensions of the inner core should be considered

when increasing the number of elements. Another possibility involves using more elements in the outer ring to improve the parallel imaging performance of the design. System interfacing must be considered when exploring this option. These potential design improvements should be evaluated in software to establish their viability and whether they introduce cost effective benefits.

Finally, further investigation comparing g-factor maps between simulated and experimentally obtained data is required. It should be determined whether quasi-static based calculation methods provide sufficient accuracy for g-factor calculation at low field systems, such as 1.5T. Maps of g-factors should be compared between quasi-static simulations, XFDTD obtained data and experimental data at different frequencies.

Appendix A – B_1-Field Mapping

In an experimental environment, only the output SNR profile is provided through different MRI scans. To separate the transmit field $\vec{B}_1^+$ from the receive field $\vec{B}_1^-$ requires clever analysis using multiple image sequences. This section describes the process where the circularly polarized magnetic field maps can be individually extracted experimentally.

The $\vec{B}_1$ fields from surface coils, and to a lesser extent volume coils, in MRI are nonuniform, creating problems that can be corrected for when the $\vec{B}_1$ field map is known. The RF coil $\vec{B}_1$ field map reveals non-uniform signal intensities associated with an inhomogeneous transmit field $\vec{B}_1^+$ and non-uniform reception sensitivity $\vec{B}_1^-$. Other non-uniform signal intensities, which can become more pronounced at higher field strengths, can be attributed to [68]:

1) Imperfections in the RF pulse.

2) RF penetration effects associated with EM parameters of the object.

3) Wave behaviour when the object size to RF wavelength ratio exceeds 0.5.

4) Gradient eddy currents from object to gradient coil coupling.

To acquire a full $\vec{B}_1$ field map experimentally, the transmit RF $\vec{B}_1^+$ field is measured using a homogeneous phantom. Note that the $\vec{B}_1^+$ field distribution differs slightly between an in-vivo experiment (using a human subject) and a uniform phantom, making the map sample dependant [3]. When using a volume coil, an SE imaging sequence has been shown as more appropriate than a GE pulse sequence. However, the GE sequence is better for acquiring a $\vec{B}_1$ map of a surface coil as stated in Section 2.2.1. The general signal voltage equation for an SE pulse sequence with relaxation effects is given as [68]

$$V_{S,SE} = \frac{M_z^0 \sin\alpha_1(r)[1-\cos\alpha_2(r)\cdot e^{-T_R/T_1} - (1-\cos\alpha_2(r))\cdot e^{-T_R/T_1}\cdot e^{-T_E/2T_1}]\times e^{T_E/T_2}\cdot \vec{B}_1^{-*}(r)}{1-\cos\alpha_1(r)\cdot\cos\alpha_2(r)\cdot e^{-T_R/T_1}} \tag{A.1}$$

where position dependant flip angles $\alpha_1(r)$ and $\alpha_2(r)$ are determined by

$$\alpha(r) = \gamma\tau\vec{B}_1^{+}(r) \tag{A.2}$$

Other required variables include time constants echo time T_E, longitudinal relaxation T_1, transverse relaxation T_2, repetition time T_R, steady state bulk magnetization M_z^0, and receive sensitivity $\vec{B}_1^{-}$.

There are too many unknowns in equations (A.1) and (A.2) to solve for $\vec{B}_1^{+}(r)$ or $\vec{B}_1^{-}(r)$ from an output image depicting only signal intensity. By choosing T_R and T_E such that $T_2 \geq 5T_E$ and $T_1 \leq 5T_R$ for the tissues being imaged, equation (A.1) becomes

$$V_{S,SE}(r) = C_{SE}(r)\cdot\vec{B}_1^{-*}\cdot\sin\alpha_1(r)\cdot\sin^2\frac{\alpha_2(r)}{2} \tag{A.3}$$

with tissue constant $C_{SE}(r)$. Analysis becomes convenient upon taking a ratio with a second image whose flip angles are twice those of the first ($\alpha_2(r) = 2\alpha_1(r)$), simplifying the mathematics to yield a ratio of

$$\lambda_{SE} = \frac{V_{S2,SE}(r)}{V_{S1,SE}(r)} = \frac{\sin^3 2\alpha_1(r)}{\sin^3\alpha_1(r)} = \frac{1}{[2\cos\alpha_1(r)]^3} \tag{A.4}$$

which can be used to solve for the transmit field by

$$|\vec{B}_1^{+}(r)| = \frac{1}{\gamma\tau}\cdot\cos^{-1}(\lambda_{SE}/8)^{1/3} \tag{A.5}$$

Note that to guarantee a unique solution; all flip angles $2\alpha_1(r)$ must be less than 90° to ensure $\sin 2\alpha_1(r)$ remains a 1-to-1 mapping function. More strictly, the small tip angle approximation for applying Fourier theory to the original Bloch Equation must be valid, indicating all flip angles should be less than 10°.

By a similar approach, the signal intensity using a GE pulse sequence can be simplified using tissue constant $C_{GE}(r)$ to be

$$V_{S,GE}(r) = C_{GE}(r) \cdot \vec{B}_1^{-*} \cdot \sin\alpha_1(r) \tag{A.6}$$

which gives the ratio of two images from GE sequences with flip angles governed as before

$$\lambda_{GE} = \frac{V_{S2,GE}(r)}{V_{S1,GE}(r)} = \frac{\sin 2\alpha_1(r)}{\sin\alpha_1(r)} = \frac{1}{2\cos\alpha_1(r)} \tag{A.7}$$

and solving for transmit field $\vec{B}_1^{+}$ gives

$$|\vec{B}_1^{+}| = \frac{1}{\gamma\tau} \cdot \cos^{-1}(\lambda_{GE}/2) \tag{A.8}$$

After using either type of input pulse sequence and solving for the transmit field, using equation (A.5) or (A.8), it is possible to determine the receive sensitivity field $\vec{B}_1^{-*}$ by applying equation (A.3) or (A.6). If imaging a phantom object that possesses constant properties, the values for $C_{SE}(r), C_{GE}(r)$ are of no concern as they are not functions of position, and thus can be ignored. Now, a complete magnitude B_1 map of the RF coil can be calculated and used for optimization or image correction purposes such as RF pulse design. Note that no phase information is determined with this approach.

References

[1] Abbott D., Davis B.R., Phillips N.J., Eshraghian K., Simple Derivation of the Thermal Noise Formula Using Window Limited Fourier Transforms and Other Conundrums, *IEEE Trans. Edu*. **39**, 1-13, 1996.

[2] Afande M.M., Wu K., Giroux M., Bosisio R.G., A Finite-Difference Frequency-Domain Method that Introduces Condensed Nodes and Image Principle, *IEEE Trans. Theory Techn.* **43**, 838-846, 1995.

[3] Barker G.J., Simmons A., A Simple Method for Investigating the Effects of Non-Uniformity of Radio Frequency Transmission and Radio Frequency Reception in MRI, *Br J Radiology*. **71**, 59-67, 1998.

[4] Bhobe A.U., Halloway C.L., Piket-May M., Meander Delay Line Challenge Problem: A Comparison Using FDTD, FEM and MoM, *IEEE Inc.*805-810, 2001.

[5] Bloch F., Nuclear Induction, *Phys. Rev*. **70**, 460-474, 1946.

[6] Bloembergen N., Purcell E.M., Pound R.V., Relaxation Effects in Nuclear Magnetic Resonance Absorption, *Phys. Rev.* **73**, 679-712, 1948.

[7] Bottomley P.A., Olivieri C.H., Giaquinto R., What is the Optimal Phased Array Coil Design for Cardiac and Torso Magnetic Resonance?, *Magn. Reson. Med*. **37**, 591-599, 1997.

[8] Brown M.A., Semelka R.C., MRI Basic Principles and Applications, Wiley-Liss Inc. 1995.

[9] Carr H.Y., Purcell E.M., Effects of Diffusion on Free Precession in Nuclear Magnetic Resonance Experiments, *Phys. Rev*. **94**, 630-638, 1954.

[10] Collins C.M., Smith M.B., Calculations of B1 Distribution, SNR and SAR for a Surface Coil Adjacent to an Anatomically Accurate Human Body Model, *Magn. Reson. Med*. **45**, 692-699, 2001.

[11] Collins C.M., Yang Q.X., Wang J.H., Zhang X., Liu H., Michaeli S., Zhu X.H., Adriany G., Vaughan J.T., Anderson P., Merkle H., Ugurbil K., Smith M.B., Chen W., Different Excitation and Reception Distributions with a Single Loop Transmit Receive Surface Coil Near a Head Sized Spherical Phantom at 300 MHz, *Magn. Reson. Med*. **47**, 1026-1028, 2002.

[12] de Zwart J.A., Ledden P.J., Kellman P., van Gelderen P., Duyn J.H., Design of a SENSE Optimized High Sensitivity MRI Receive Coil for Brain Imaging, *Magn. Reson. Med*. **47**, 1218-1227, 2002.

[13] Dumoulin C.L., Giaquito R.O., Rohling K.W., Rossi C.J., Watkins R.D., Hardy C.J., Darrow R.D., A 32-Channel Coil for Phased Array Imaging at 1.5 Tesla, *In Proc 11th Annual Meeting ISMRM*, Toronto. p431 2003.

[14] Dunn A., Yee's Algorithm, http://www.nmr.mgh.harvard.edu/~adunn/papers/dissertation/node32.html, 1998.

[15] Edelstein W., Glover G.H., Hardy C.J., Redington R.W., The Intrinsic Signal to Noise Ratio in NMR Imaging, *Magn. Reson. Med*. **3**, 604-618, 1986.

[16] Foo T.K., Ho V.B., Saranathan M., Cheng L., Sakuma H., Kraitchman D.L., Wu K.C., Bluemke D.A., Feasibility of Integrating High Spatial Resolution 3D Breath Hold Coronary MR Angiography with Myocardial Perfusion and Viability Examinations, *Radiology*. **235**, 1025-1030, 2005.

[17] Gabriel C., Gabriel S., Cothout E., The Dielectric Properties of Biological Tissues I. Literature Survey, *Phys. Med. Bio*. **41**, 2231-2249, 1996.

[18] Griswold M.A., Jacob P.M., Heidemann R.M., Nittka M., Jellus V., Wang J., Kiefer B., Haase A., Generalized Autocalibrating Partially Parallel Acquisitions (GRAPPA), *Magn. Reson. Med.* **47**, 1202-1210, 2002.

[19] Hahn E.L., Spin Echos, *Phys. Rev*. **80**, 580-594, 1950.

[20] Hardy C.J., Cline H.E., Giaquinto R.O., Niendorf T., Grant A.K., Sodickson D.K., 32-Element Receiver Coil Array for Cardiac Imaging, *Magn. Reson. Med*. **55**, 1142-1149, 2006.

[21] Hardy C.J., Darrow R.D., Saranathan M., Giaquinto R.O., Zhu Y., Dumoulin C.L., Bottomley P.A., Large Field of View Real Time MRI With a 32-Channel System, *Magn. Reson. Med*. **52**, 878-884, 2004.

[22] Hayes C., Hattes N., Roemer P.B., Volume Imaging with MR Phased Arrays, *Magn. Reson. Med*. **18**, 309-319, 1991.

[23] Hayes C., Roemer P.B., Noise Correlations in Data Simultaneously Acquired from Multiple Surface Coil Arrays, *Magn. Reson. Med.* **16**, 181-191, 1990.

[24] Hornak J.P., The Basics of MRI, http://www.cis.rit.edu/htbooks/mri/. 2006.

[25] Hoult D.I., The Principle of Reciprocity in Signal Strength Calculations – A Mathematical Guide, *Concepts Magn. Reson*. **12**, 173-187, 2000.

[26] Hoult D.I., Phil D., Sensitivity and Power Deposition in a High Field Imaging Experiment, *Journal Magn. Reson. Imag*. **12**, 46-67, 2000.

[27] Huber M.E., Kozerke S., Pruessmann K.P., Smink J., Boesiger P., Sensitivity Encoded Coronary MRA at 3T, *Magn. Reson. Med*. **52**, 221-227, 2004.

[28] Ibrahim T.S., Modeling the EM Wave Interaction with the Body and SAR, *ISMRM 14th Annual Meeting.* Seattle, 2006.

[29] Ibrahim T.S., Adbuljalil A.M., Lee R., Robitaille P.M., Analysis of B_1 Field Profiles and SAR Values for Multi-Strut Transverse Electromagnetic RF Coils in High Field MRI Applications, *Phys. Med. Bio*. **46**, 2545-2555, 2001.

[30] Insko E.K., Bolinger L., Mapping of the Radiofrequency Field, *Journal Magn. Reson*. **103**,82-85, 1993.

[31] Jin J., "Electromagnetic Analysis and Design in Magnetic Resonance Imaging", CRC Press, Boca Raton, 1998.

[32] Kaplan W., "Advanced Calculus 4th Ed.", Addison-Wesley, 1992.

[33] Keller J.S., "Design and Performance of a Quadrature Elliptic Birdcage Resonator for Magnetic Resonance Imaging", M.Sc. Thesis, Department of Electrical Engineering, University of Western Ontario, 1999.

[34] King S.B., Duensing R.G., Zero Shared Resistance Between Coil Elements of a Phased Array, *Proc ISMRM 8th Annual Meeting*, Denver, P1406, 2000.

[35] King S.B., Vijayakumar S., Huang F., Saylor C., Duensing R.G., Improved A-P Parallel MRI of the Spine Using a Twisted Array, *Proc ISMRM 14th Annual Meeting*, Seattle, P2576, 2006.

[36] King S.B., Varosi S.M., Duensing R.G., Eigenmode Analysis for Understanding Phased Array Coils and Their Limits, *Concepts in Magn. Reson*. B. **29**, 42-49, 2006.

[37] Kunz K.S., Luebbers R.J., "The Finite Difference Time Domain Method for Electromagnetics", CRC Press Inc, 1993.

[38] Lauterbur P.C., Image Formation by Induced Local Interactions: Examples Employing Nuclear Magnetic Resonance, *Nature*, 242, 190-225, 1973.

[39] Lee H., Kim J., Modified Yee's Cell for Finite-Difference-Time-Domain Modeling of Periodic Boundary Guiding Structure, *IEEE MTT-S Digest*. 889-892, 2001.

[40] Liang Z.P., Lauterbur P.C., "Principles of Magnetic Resonance Imaging: A Signal Processing Perspective", IEEE Inc., New York, 2000.

[41] Lide D.R., "CRC Handbook of Chemistry and Physics 86th Edition 2005-2006", CRC Press, Taylor & Francis Group, 2005.

[42] McKenzie C.A., Yeh E.N., Ohlinger M.A., Price M.D., Sodickson D.K., Self Calibrating Parallel Imaging With Automatic Coil Sensitivity Extraction, *Magn. Reson. Med*. **47**, 529-538, 2002.

[43] National Institutes of Health. "Visible Human Project", US National Library of

Medicine, 2004.

[44] Niendorf T., Hardy C.J., Giaquinto R.O., Gross P., Cline H.E., Zhu Y., Kenwood G., Cohen S., Grand A.K., Joshi S., Rofsky N.M., Sodickson D.K., Toward Single Breath Hold Whole Heart Coverage Coronary MRA Using Highly Accelerated Parallel Imaging With a 32 Channel MR System, *Magn. Reson. Med*. **56**, 167-176, 2006.

[45] Ohliger M.A., Grant A.K., Sodickson D.K., Ultimate Intrinsic Signal-to-Noise Ratio for Parallel MRI: Electromagnetic Field Considerations, *Magn, Reson. Med*. **50**, 1018-1030, 2003.

[46] Ohliger M.A., Ledden P., McKenzie C.A., Sodickson D.K., Effects of Inductive Coupling on Parallel MR Image Reconstructions, *Magn. Reson. Med*. **52**, 628-639, 2004.

[47] Poljak D., Brebbia C.A., "Boundary Element Methods for Electrical Engineers", WIT Press, 2005.

[48] Pozar D.M., "Microwave Engineering 3rd Ed", John Wiley & Sons. 2005.

[49] Pruessmann K.P., Weiger M., Scheidegger B., Boesiger P., SENSE: Sensitivity Encoding for Fast MRI, *Magn. Reson. Med*. **42**, 952-962, 1999.

[50] Purcell E.M., Torrey H.C., Pound R.V., Resonance Absorption By Nuclear Magnetic Moments in a Solid, *Phys. Rev*. **69**, 37-38, 1946.

[51] Pykett I.L., Rosen B.R., Buonanno F.S., Brady T.J., Measurement of Spin Lattice Relaxation Times in Nuclear Magnetic Resonance Imaging, *Phys. Med. Bio*. **28**, 723-729, 1983**.**

[52] Ramo S., Whinnery J.R., Van Duzer T., "Fields and Waves in Communication Electronics 3rd Ed.", John Wiley & Sons Inc. 1994.

[53] Reeder S.B., Wintersperger B.J., Dietrich O., Lanz T., Greiser A., Reiser M.F.m Glazer G.M., Schoenberg S.O., Practical Approaches to the Evaluation of Signal-to-Noise Ratio Performance with Parallel Imaging: Application with Cardiac Imaging and a 32-Channel Cardiac Coil, *Magn. Reson. Med*. **54**, 748-754, 2005.

[54] Roemer P.B., Edelstein W.A., Hayes C.E., Souza S.P., Mueller O.M., The NMR Phased Array, *Magn. Reson. Med*. **16**, 192-225, 1990.

[55] Schnell W., Renz W., Vester M., Ermert H., Ultimate Signal to Noise Ratio of Surface and Body Antennas for Magnetic Resonance Imaging, *IEEE Trans on Ant. and Prop.*, **48**, 418-428, 2000.

[56] Smith M.J., McNabb C., Phased Array Volume Coil for MR Imaging of the Brain, University of Manitoba, Department of Electrical and Computer Engineering, Final Design Project, 2004.

[57] Sodickson D.K., McKenzie C.A., A Generalized Approach to Parallel Magnetic Resonance Imaging, *Med. Phys*. 28, 1629-1643, 2001.

[58] Sodickson D.K., Hardy C.J., Zhu Y., Giaquinto R.O., Kenwood G., Niendorf T., Lejay H., McKenzie C.A., Ohlinger M.A., Grant A.K., Rofsky N.M., Rapid Volumetric MRI Using Parallel Imaging With Order of Magnitude Accelerations and a 32 Element RF Coil Array, *Acad. Rad*. **12**, 626-635, 2005.

[59] Sodickson D.K., Manning W.J., Simultaneous Acquisitions of Spatial Harmonics (SMASH): Fast Imaging with Radiofrequency Coil Arrays, *Magn. Reson. Med*. **38**, 591-603, 1997.

[60] Stuber M., Botnar R.M., Fischer S.E., Lamerichs R., Smink J., Harvey P., Manning W.J., Preliminary Report on In Vivo Coronary MRA at 3 Tesla in Humans, *Magn. Reson. Med*. **48**, 425-429, 2002.

[61] Terman F.E., Helliwell R.A., Pettit J.M., Watkins D.A., Rambo W.R., "Electronic and Radio Engineering", McGraw-Hill Book Company Inc., 1955.

[62] Taves T., "In Vivo Conductivity Measurement Using MRI-Guided Noise Tomography", M.Sc. Thesis, Department of Physics and Astronomy, University of Manitoba, 2007.

[63] Tilley A.R., The Measure of Man & Woman, *John Wiley & Sons*. 2002.

[64] Umashankar K.R., Taflove A., A Novel Method to Analyze Electromagnetic Scattering of Complex Objects, *IEEE Trans. EM Compatibility*. **24**, 397-405, 1982.

[65] Umashankar K.R., Taflove A., Beker B., Calculation and Experimental Validation of Induced Currents on Coupled Wires in an Arbitrary Shaped Cavity, *IEEE Trans. Antennas Prop.* **35**, 1248-1257, 1987.

[66] Vaughan J.T., Garwood M., Collins C.M., Liu W., DelaBarre L., Adriany G., Andersen P., Merkle H., Goebel R., Smith M.B., Ugurbil K., 7T vs 4T: RF-Power, Homogeneity and Signal-to-Noise Comparison in Head Images, *Magn. Reson. Med*. **46**, 24-30, 2001.

[67] Walsh D.O., Gmitro A.F., Marcellin M.W., Adaptive Reconstruction of Phased Array MR Imagery, *Magn. Reson. Med*. **43**, 682-690, 2000.

[68] Wang J., Qiu M., Yang Q.X., Smith M.B., Constable R.T., Measurement and Correction of Transmitter and Receiver Induced Nonuniformities In Vivo, *Magn. Reson. Med*.**53**, 408-417, 2005.

[69] Wang J., Reykowski A., Dickas J., Calculation of the Signal to Noise Ratio for Simple Surface Coils and Arrays of Coils, *IEEE Trans on Biomed. Eng*. **42**, 908-917, 1995.

[70] Wang J., Yang Q.X., Zhang X., Collins C.M., Smith M.B., Zhu X.H., Adriany G., Ugurbil K., Chen W., Polarization of the RF Field in a Human Head at High Field: A Study with a Quadrature Surface Coil at 7.0T, *Magn. Reson. Med*. **48**, 362-369, 2002.

[71] Weber O.M., Martin A.J., Higgins C.B., Whole heart Steady State Free Precession Coronary Artery Magnetic Resonance Angiography, *Magn. Reson. Med.* **50**, 1223-1228, 2003.

[72] Wei J., Yuan J., Shen G.X., Effect of Tuning Capacitor Placement on Mutual Coupling for MRI Array Coils, *Concepts Magn. Reson. B.* **29**, 50-54, 2006.

[73] Weiger M., Pruessmann K.P., Leussler C., Roschmann P., Boesiger P., Specific Coil Design for SENSE: A Six Element Cardiac Array, *Magn. Reson. Med*. **45**, 495-504, 2001.

[74] Weiger M., Pruessmann K.P., Boesiger P., 2D SENSE for Faster 3D MRI, *Magn. Reson. Mater. Phys. Biol. Med*. **14**, 10-19, 2002.

[75] Wiesinger F., Boesiger P., Pruessmann K.P., Electrodynamics and Ultimage SNR in Parallel MR Imaging, *Magn. Reson. Med.* **52**, 376-390, 2004.

[76] Wright S.M., Wald L.L., Theory and Application of Array Coils in MR Spectroscopy, *NMR in Biomed*. **10**, 394-410, 1997.

[77] Yee K.S., Numerical Solution of Initial Boundary Value Problem Involving Maxwell's Equations in Isotropic Media, *IEEE Trans. Antennas Prop*. **14**, 302-307, 1966.

[78] Zhao H., Crozier S., Liu F., A High Definition Finite Difference Time Domain Method, *App. Mathematical Modelling.* **27**, 409-419, 2003.

[79] Zhu Y., Hardy C.J., Giaquinto R., Rohling K., Dumoulin C., Sodickson D.K., Ohlinger M., Darrow R., Kenwood G., Highly Parallel Volumetric Imaging with Accelerated Spatial Encoding along Two Dimensions, *In Proc. 11th Annual Meeting ISMRM*, Toronto, p22, 2003.

[80] Zhu Y., Hardy C.J., Sodickson D.K., Giaquinto R.O., Dumoulin C.L., Kenwood G., Niendorf T., Lejay H., McKenzie C.A., Ohlinger M.A., Rofsky N.M., Highly Parallel Volumetric Imaging With a 32 Element RF Coil Array, *Magn. Reson. Med*. 52, 869-877, 2004.